

STUDY OF THE EXCITED STATES OF  $^{60,61}\text{Zn}$

By

RONALD B. SCHUBANK, B.SC.

A Thesis

Submitted to the School of Graduate Studies

in Partial Fulfilment of the Requirements

for the Degree

Doctor of Philosophy

McMaster University

© December, 1985

W

STUDY OF  $^{60,61}\text{Zn}$  -- SCHUBANK -- Ph.D.

DOCTOR OF PHILOSOPHY (1985)  
(Physics)

McMASTER UNIVERSITY  
Hamilton, Ontario

TITLE: Study of the excited states of  $^{60,61}\text{Zn}$

AUTHOR: Ronald B. Schubank, B.Sc. (McMaster University)


SUPERVISOR: Professor John A. Cameron

NUMBER OF PAGES: xvii

## Abstract

The level structures of the nuclei  $^{60}\text{Zn}$  and  $^{61}\text{Zn}$  have been studied by means of  $(\tau, n\gamma)$  and  $(\alpha, n\gamma)$  reactions, respectively. Additional heavy ion induced reactions were also investigated with respect to  $^{60,61}\text{Zn}$  and other competing channels, notably  $^{59}\text{Zn}$ ,  $^{60}\text{Cu}$  and  $^{61}\text{Ga}$ . Gamma singles, n- $\gamma$  coincidence,  $\gamma$ - $\gamma$ , multi- $\gamma$  coincidence,  $\gamma$  and n- $\gamma$  angular distribution measurements were made. Limitations on excited state lifetimes were obtained from beam pulsing, electronic timing, and Doppler shift measurements. A high resolution neutron spectrum of the  $^{58}\text{Ni}(\alpha, n)^{61}\text{Zn}$  reaction was obtained. Attempts at other multi-particle transfer experiments have been unsuccessful.

The experimental results are compared with those found elsewhere and with theoretical calculations.



Acknowledgements

First and foremost, I would like to thank my supervisor, Dr. J.A. Cameron, for his inspiration, guidance and assistance throughout the course of my studies. I wish also to express my gratitude to the other members of my supervisory committee, Drs. R.G. Summers-Gill and R. Childs.

I would like to acknowledge the help, cooperation and camaraderie of all the faculty, students and staff of the Tandem Lab, especially the members of my research group. In particular, to my fellow student Victor Janzen, I extend a special thank you.

I would also like to express my thanks to Mrs. Suzanna Wannamaker for typing this thesis.

And finally, to my parents, whose love and support have never failed.

## Table of Contents

Chapter		Page
1	Introduction	1
2	Theory	
	2.1 Introduction	4
	2.2 Shell model (I): the SPM and IPM	5
	2.3 Pairing interaction and Quasi-particles	7
	2.4 Unified vibrational and rotational models	9
	2.5 Hartree-Fock-Bogolyubov	14
	2.6 Shell model (II): the SDI	16
	2.7 Electromagnetic decay properties	22
	2.8 Heavy ion induced reactions	29
3	Experimental Techniques	
	3.1 Introduction	34
	3.2 Production of projectiles	36
	3.3 Target preparation and chambers	38
	3.4 Detectors	41
	3.4.1 $\gamma$ detectors	41
	3.4.2 Neutron detectors	43

3.4.3	Charged-particle detectors	50
3.5	Prompt $\gamma$ studies	53
3.5.1	Singles	53
3.5.2	Yield curves	54
3.5.3	n- $\gamma$ coincidence	56
3.5.4	$\gamma$ - $\gamma$ coincidence	58
3.5.5	Multiple- $\gamma$ events; MPF	59
3.6	Angular distributions	62
3.7	Delayed decay studies	72
3.7.1	Electronic timing	72
3.7.2	Beam off activity	74
3.7.3	DSAM	75
4	Experimental Results for $^{61}\text{Zn}$	
4.1	Results and general discussion	78
4.2	Discussion of levels	139
4.2.1	The 88 and 124 keV levels	139
4.2.2	The 418 keV level	141
4.2.3	The 755 keV level	142
4.2.4	The 938 keV level	143
4.2.5	The 996 keV level	145
4.2.6	The 1265 keV level	146
4.2.7	The 1361, 1402 and 1659 keV levels	147
4.2.8	The 1802, 2034 and 2098 keV levels	149

	4.2.9	The 2003, 2270 and 2796 keV levels	149
	4.2.10	The 2400, 3337 and 4413 keV levels	153
5	<sup>60</sup> Zn:	Results and Discussion	155
	5.1	Results and general discussion	155
	5.2	Discussion of levels	177
	5.2.1	The 1003 and 2192 keV levels	177
	5.2.2	The 3509 keV level	178
	5.2.3	The 3971 keV level	180
	5.2.4	The 4199 keV level	180
	5.2.5	The 3811, 4349, 4774 and 5336 keV levels	181
	5.2.6	The 4912, 6638, 7371 and 8701 keV levels	182
	5.2.7	The 3034 and 3626 keV levels	184
6		Summary and Concluding Remarks	185
		Appendix	193
	A.1	<sup>58</sup> Ni( $\tau, n\gamma$ ) <sup>59</sup> Cu reaction	193
	A.2	New levels in <sup>60</sup> Cu produced by heavy ion reactions	193
	A.3	Other channels	200
		References	207



## List of Tables

		Page
Table 4.1	$^{61}\text{Zn}$ $\gamma$ energies in the $(\alpha, n\gamma)$ reaction	87
Table 4.2	Contents of $^{61}\text{Zn}$ coincidence gates at $E_\alpha = 20$ MeV	91
Table 4.3	Contents of $^{61}\text{Zn}$ coincidence gates at $E_\alpha = 15$ MeV	98
Table 4.4	Summary of $(\alpha, n\gamma)$ $^{61}\text{Zn}$ work	116
Table 4.5	Energies and intensities of $^{61}\text{Zn}$ levels in the $(\alpha, n)$ reaction	124
Table 4.6	$^{61}\text{Zn}$ $\gamma$ energies in other HI reactions	130
Table 4.7	Contents of $^{61}\text{Zn}$ coincidence gates at 66 MeV $^{24}\text{Mg}$ on Ca	131
Table 4.8	Summary of levels from $\gamma$ work	132
Table 5.1	$^{60}\text{Zn}$ $\gamma$ energies in the $(\tau, n\gamma)$ reaction	156
Table 5.2	Contents of $^{60}\text{Zn}$ coincidence gates at $E_\tau = 12$ MeV	167
Table 5.3	Summary of $(\tau, n\gamma)$ $^{60}\text{Zn}$ work	175
Table A.1	New $\gamma$ lines and levels in $(\tau, pn\gamma)$ $^{59}\text{Cu}$	196
Table A.2.1	Summary of $^{60}\text{Cu}$ $\gamma$ rays observed in the $\gamma$ experiments	201
Table A.2.2	Contents of $^{60}\text{Cu}$ coincidence gates at $E_\tau = 12$ MeV	203

Table A.2.3 Contents of  $^{60}\text{Cu}$  coincidence gates at 204

$E_{\text{Na}} = 70 \text{ MeV}$

Table A.2.4 Summary of  $^{60}\text{Cu}$  levels based on the 205  
 $\gamma$  experiments

## List of Figures

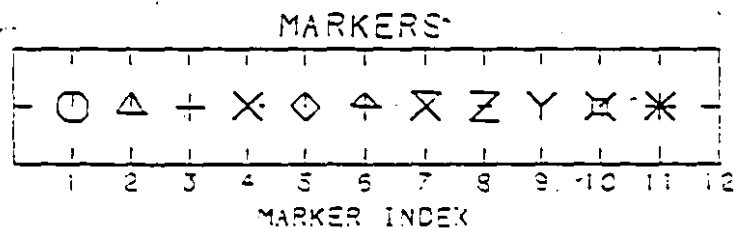
		Page
Figure 2.1	Single particle energy levels	6
Figure 2.2	Portion of chart of nuclides	30
Figure 3.1	Layout of facilities	39
Figure 3.2	Block diagram of $\gamma$ detector electronics	44
Figure 3.3	Block diagram for neutron detector electronics	44
Figure 3.4	Neutron detector pulse shape spectrum	46
Figure 3.5	Neutron detector pulse height spectrum	47
Figure 3.6	Seforad $^3\text{He}$ ion chamber efficiency curve	51
Figure 3.7	i) Typical $\gamma$ - $\gamma$ coincidence circuit	60
	ii) Typical (5) $n\gamma$ coincidence circuit for $n\gamma$ angular distributions	61
Figure 4.1	$^{58}\text{Ni}(\alpha, n\gamma)^{61}\text{Zn}$ $\gamma$ - $\gamma$ projections at $E_\alpha = 20$ MeV	79
Figure 4.2	$n\gamma$ spectrum at $E_\alpha = 20$ MeV	80
Figure 4.3	$\gamma$ -singles spectrum at $E_\alpha = 20$ MeV	81

Figure 4.4	Typical beam off $\gamma$ spectrum used in normalizations ( $^{61}\text{Cu} + ^{61}\text{Ni}$ )	83
Figure 4.5	Typical inverse normalization correction curve between two Ge(Li) detectors	84
Figure 4.6	Typical normalization correction curve of a single Ge(Li) detector	85
Figure 4.7	123 keV coincidence gate spectrum at 20 MeV	88
Figure 4.8	756 keV coincidence gate spectrum at 20 MeV	89
Figure 4.9	873 keV coincidence gate spectrum at 20 MeV	90
Figure 4.10	$^{58}\text{Ni}(\alpha, n\gamma)^{61}\text{Zn}$ at $E_\alpha = 15$ MeV $\gamma$ - $\gamma$ projections	94
Figure 4.11	123 keV coincidence gate spectrum at 15 MeV	95
Figure 4.12	756 keV coincidence gate spectrum at 15 MeV	96
Figure 4.13	873 keV coincidence gate spectrum at 15 MeV	97
Figure 4.14	Illustration of method for crude compensation of $\bar{n}\gamma$ events into $n\gamma$ spectra	99
Figure 4.15	Clean $n\gamma$ coincidence spectrum for $^{61}\text{Zn}$	101

Figure 4.16	1141 keV gate TAC spectrum for n $\gamma$ events of Figure 4.15	102
Figure 4.17	Singles $\gamma$ yields for 88 and 123 keV lines	104
Figure 4.18	Singles $\gamma$ yields relative to 88 keV line	106
Figure 4.19	High resolution singles spectra at $E_{\alpha} = 15$ MeV	108
Figure 4.20	756 keV n $\gamma$ angular distribution at $E_{\alpha} = 20$ MeV	109
Figure 4.21	756 keV $\gamma$ singles angular distri- bution at $E_{\alpha} = 15$ MeV	110
Figure 4.22	756 n $\gamma$ angular distributions at 15 MeV	112
Figure 4.23	Proposed level scheme of $^{61}\text{Zn}$ based on the ( $\alpha$ ,n $\gamma$ ) experiments performed in this project	121
Figure 4.24	$^{58}\text{Ni}(\alpha, n)^{61}\text{Zn}$ neutron energy spectrum	122
Figure 4.25	$^{16}\text{O}$ on $^{50}\text{Cr}$ singles $\gamma$ spectrum at 60 MeV	125
Figure 4.26	$^{10}\text{B}$ on $^{54}\text{Fe}$ singles $\gamma$ spectrum at 45 MeV	126
Figure 4.27	$^6\text{Li}$ on $^{58}\text{Ni}$ singles $\gamma$ spectrum at 30 MeV	127
Figure 4.28	$^{24}\text{Mg}$ on Ca singles $\gamma$ spectrum at 66 MeV	128

Figure 4.29	$^{23}\text{Na}$ on Ca singles $\gamma$ spectrum at 70 MeV	129
Figure 4.30	Summary of experimental $^{61}\text{Zn}$ level schemes	134
Figure 4.31	Comparison of experimental $^{61}\text{Zn}$ level schemes with SDI shell model predictions of van Hienen et al.	135
Figure 4.32	Odd-A systematics for N=31 isotones and Z=30 isotopes near $^{61}\text{Zn}$	136
Figure 4.33	WCM and experimental level scheme for $^{65}\text{Zn}$	137
Figure 5.1	$^{58}\text{Ni}(\tau, n\gamma)^{60}\text{Zn}$ $\gamma$ - $\gamma$ projections at $E_{\tau} = 12$ MeV	160
Figure 5.2	$\gamma$ singles spectrum at $E_{\tau} = 12$ MeV	161
Figure 5.3	$90^{\circ}$ n- $\gamma$ coincidence spectrum at $E_{\tau} = 12$ MeV illustrating $\bar{n}$ events	162
Figure 5.4	Typical beam off $\gamma$ spectrum following 12 MeV $\tau$ irradiation	164
Figure 5.5	1004 keV gate at $E_{\tau} = 12$ MeV	165
Figure 5.6	1189 keV gate at $E_{\tau} = 12$ MeV	166
Figure 5.7	Clean n $\gamma$ coincidence spectrum for $^{60}\text{Zn}$	168
Figure 5.8	Clean n $\gamma$ coincidence spectrum for $^{60}\text{Zn}$ at $E_{\tau} = 8$ MeV	169
Figure 5.9	Proposed $^{60}\text{Zn}$ level scheme	171

Figure 5.10	Comparison of experimental levels of $^{60}\text{Zn}$ with theories	173
Figure 5.11	Even-A systematics for $N=30$ isotones and $Z=30$ isotopes near $^{60}\text{Zn}$	176
Figure A.1	Lines and levels in $^{59}\text{Cu}$ via $(\tau, pny)$	194
Figure A.2	$^{60}\text{Cu}$ level schemes	197



## Glossary of Abbreviations

$a_k$	normalized $\gamma$ angular distribution coefficient
$A_k$	unnormalized $\gamma$ angular distribution coefficient
ADC	analogue to digital converter
$B_k$	statistical tensor for perfect alignment
B(E2), B(M1)	reduced transition rate
BCS	Bardeen-Cooper-Schrieffer theory
CFD	constant fraction discriminator
CN	compound nucleus
C.O.	cross-over timing
c, cont	contaminated
d	doublet
DEL / DA	delay/amplifier
DDLA	double delay line (clipping) amplifier
DSAM	doppler shift attenuation method
$E_x$	excitation energy
E2	electric quadrupole transition or $\gamma$ -ray
FWHM	full width half maximum
GDG	gate and delay generator
Ge, Ge(int), HPGe	intrinsic (hyperpure) germanium $\gamma$ -ray detector



Ge(Li)	lithium drifted germanium detector
H	Hamiltonian
H, HB, HF, HFB	Hartree-Fock-Bogolyubov
HV	high voltage power supply
IPM	independent particle model
LA	linear (RC shaping) amplifier
LSD	logic shaper and delay
M.E.	matrix element
M1	magnetic dipole transition of $\gamma$ -ray
MCA	multi channel analyzer
MPF	multiplicity filter
MSDI	modified surface delta interaction
n	neutron
nPHA	neutron detector pulse height analysis
nPSA	neutron detector pulse shape analysis
nTOF	neutron time of flight
n $\gamma$	neutron- $\gamma$ coincidence
$\bar{n}$	$\gamma$ ray seen in neutron detector
NaI, NaI(Tl)	sodium iodide (thallium doped) detector
o	not seen
p	proton
$P_m(J)$	population of the $J_z = m$ substate
PAPS	preamp power supply
$Q_k$	solid angle correction coefficient (for $\gamma$ ray angular distributions)
QCVM	quasi cluster vibrational model

SCA	single channel analyser
SEMF	semi-empirical mass formula
SM	shell model
SPM	single particle model
TAC	time to amplitude converter
TFA	timing filter amplifier
TPC	timing pickoff control
TR	transition rate
t	triplet
$U_k$	population dealignment coefficient of order k. (Due to $\gamma$ top feeding)
x	modified gaussian population parameter; particle or $\gamma$ seen
xcoin	(example: 2-) fold coincidence
$W(\theta)$	$\gamma$ angular distribution
$\alpha$	alpha particle: ${}^4\text{He}^{++}$ (as projectile or particle)
$-\beta$	beta particle: nuclear emitted electron or positron (also electron capture)
$\gamma$	gamma ray
$\gamma\gamma$	$\gamma\gamma$ coincidence
$\delta$	mixing ratio (usually E2 to M1)
$\rho_k$	statistical tensor of order k
$\sigma$	cross section; gaussian population width parameter
$\tau$	${}^3\text{He}^{++}$ (as projectile or particle)

## CHAPTER 1

### Introduction

In an introductory course on nuclear physics, a professor of mine, (R.G. Summers-Gill), once made the analogy of nuclear physics with stamp collecting. The two main problems in nuclear physics are that the interactions are very complex and only partially understood -- even today. Hampering matters is the fact that most nuclei contain either too many particles (i.e. more than two) or too few (cf. the effectively infinite number of atoms in even the tiniest of solid state devices). One is therefore faced with solving a general n-body problem with complicated forces and special attention paid to quantum mechanics and occasionally, relativity. Hence the idea of stamp collecting: data are collected and analysed for patterns; phenomenological, macroscopic and microscopic theories are developed to try to account for these patterns and in turn predict additional properties. With time, the techniques of both theoretical and experimental realms become more refined.

Two of the earliest and most important "patterns" recognized were the Shell Model of Mayer (1949) and Haxel,

Jensen and Suess (1949) and the Collective Models of Bohr (1952) and Bohr and Mottelson (1953).

The theoretical inspiration for this thesis has in fact been the series of shell model calculations carried out on the Zn isotopes by van Hienen et al. (1976). The nuclei  $^{60}\text{Zn}$  and  $^{61}\text{Zn}$  were chosen to be studied in this thesis partly because little was known about their structure and electromagnetic decay modes when this project began and partly to test the validity of the theoretical predictions. To accomplish this, a number of experimental techniques incorporating heavy ion induced reactions and subsequent decays were employed to determine energy levels, spins, parities and  $\gamma$  transition branches, multipolarities and lifetimes.

In the course of these investigations, hitherto unknown properties of other nuclei near  $A=60$  were uncovered, most notably  $^{60}\text{Cu}$ . Since the shell model calculations of Glaudemans et al (1972) and Koops and Glaudemans (1977) of the Ni and Cu isotopes provide the foundation for the Zn calculations, any new information on  $^{60}\text{Cu}$ ,  $^{59}\text{Zn}$ ,  $^{61}\text{Ga}$ , etc. is not without relevance.

The following chapters describe both the theoretical and experimental aspects of the methodology. The experimental results are presented and discussed in the light of theory and results obtained by others; in particular, the  $\gamma$  spectroscopy work of Kamermans et al. (1970) regarding  $^{60}\text{Zn}$ ,

Sarantites et al. (1973) and Smith et al. (1982) for  $^{61}\text{Zn}$ , the particle work of Woods et al. (1978) and Weber et al. (1979) for both  $^{60,61}\text{Zn}$ , and neutron time of flight work by Evans et al. (1972), Greenfield et al. (1971) and Alford et al. (1975) for  $^{60}\text{Zn}$ .

## CHAPTER 2

### Theory

#### 2.1. Introduction

To solve the problem of the structure of the nucleus and all its properties from first principles is by its very nature an impossible task. One must resort to the use of models to give a systematic understanding. Even then, the problems of solving these "simplified" models can often be rather formidable. Complicating matters are the natural limitations of such models. A given model may do well in describing certain features of a given nucleus yet fail miserably with other properties or other nuclei.

The details of the more "fashionable" models to date have been the subject of numerous papers, theses and texts. To avoid duplication, most of the details will not be presented in this discussion of the theory. Rather, greater emphasis will be placed on the main ideas of the theories relevant to this project. Excellent general and specific treatments may be found in numerous sources, such as: Preston and Bhaduri (1975), Rowe (1970), Glaudemans (1967, 1970), DeShalit and Talmi (1963).

## 2.2 Shell Model (I): The single and independent particle models

The Single Particle Model (SPM) represents the most extreme aspect of the shell model. In its simplified form, each nucleon is considered to move independently in a stationary orbit within the nucleus. The strong nuclear force felt by the nucleons effectively forms a static average common potential. Properties such as excitation energies, spins and moments are then solely determined by the "outermost" or "valence" particle, with the assumption that the remaining particles form spin  $J=0$  pairs.

Such a model works well for nuclei with numbers of protons and/or neutrons near one of the "magic" numbers:  $Z$  or  $N = 2, 8, 20, 28, 50, 82, 126$ . These magic numbers arise from the large energy gaps between major shells as shown in Fig. 2.1. If an extra particle is added to a closed shell (A), it is automatically confined to a higher shell. The low lying excitations in (A+1) are due to promotion of the particle to even higher shells. Similarly, if a particle is removed from an otherwise closed shell (A) a "hole" is formed. Excitations in (A-1) are due to the hole migrating to lower shells. Due to the large energy gap, only high lying excitations are formed by promoting the unpaired particles/holes.

If an available level can accommodate many particles, then the addition of a  $J=0$  coupled pair of particles to (A')

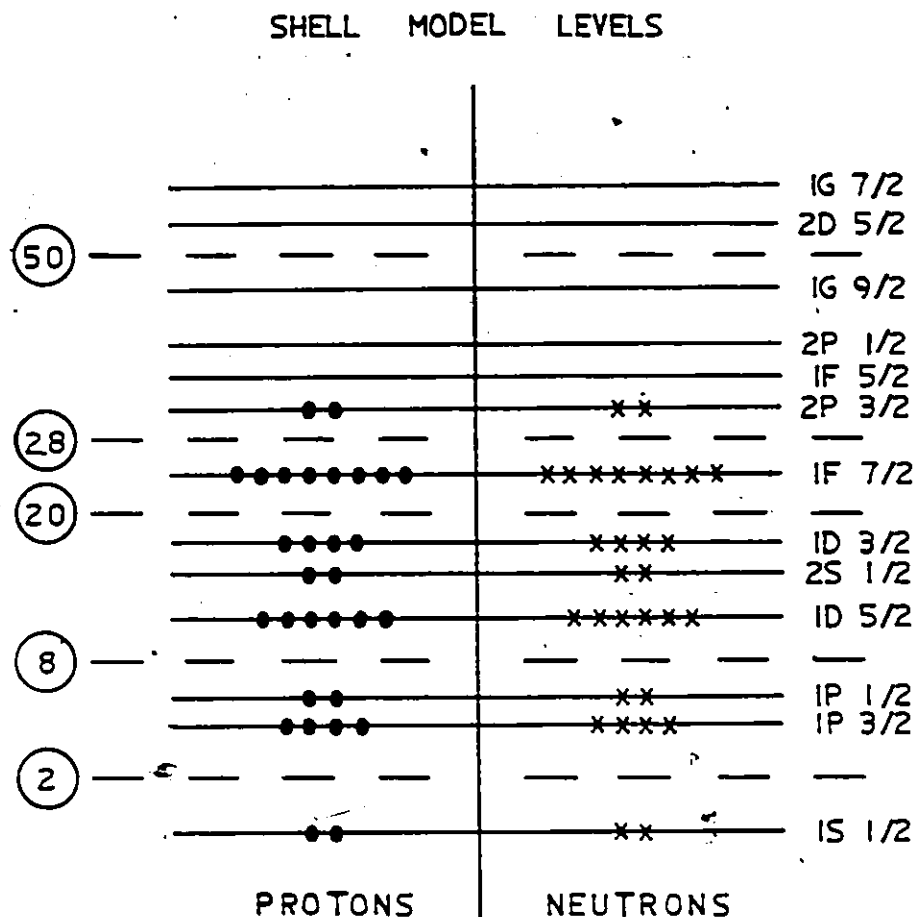


Figure 2.1. Single particle energy levels for typical nuclear potential. Magic numbers are due to the relatively large energy gaps between certain levels. These numbers can be reproduced in a nuclear shell model by adding a spin-orbit term to a potential such as a square-well with rounded edges. The actual spacings are not drawn to scale and may vary depending upon parameters used. Because of Coulomb effects, the sequence for protons may differ somewhat from neutrons.



should produce qualitatively only small differences in the low lying structure of  $(A'+2)$ . Alternatively, if the particles added to  $(A)$  are all uncorrelated, one is left with the slightly more generalized Independent Particle Model (IPM).

Not surprisingly, both these models deteriorate rapidly as the number of valence particles or holes increases. For example,  $^{61}\text{Zn}$  might naively be considered in the SPM or IPM as a  $^{60}\text{Zn}$  core plus one neutron. But  $^{60}\text{Zn}$  in itself does not provide a suitably inert core. A more favourable candidate for an inert core might be doubly magic  $(Z=N=28)$   $^{56}\text{Ni}$ . However, caution might have to be exercised as the coulomb repulsion of the 28 protons is sufficiently large to render  $^{56}\text{Ni}$  unstable; also, as of this writing, the one proton particle nucleus,  $^{57}\text{Cu}$  and one neutron hole nucleus  $^{55}\text{Ni}$  have yet to be reliably identified. The next best candidate for closed shells would be  $^{40}\text{Ca}$  or  $^{48}\text{Ca}$  but obviously the number of valence particles needed to make nickel or zinc is presently far too large for the IPM to have any hope of succeeding. One must introduce some kind of effective interaction(s) between these valence particles.

### 2.3 Pairing interaction and quasiparticles

The success, and at the same time, failure of the IPM is due in part to the fact that fermions tend to form pairs coupled to  $J=0$ . This may also be seen in the pairing term

of the Semi Empirical Mass Formula (SEMF) of von Weizsäcker (1935) and in the relatively large energy gap between the ground state and first excited state of any near-spherical even-even nucleus. An explanation for this behaviour can be found if one includes a short range interaction in the overall potentials. The theory was originally developed by Bardeen, Cooper and Schrieffer (1957) to describe electron superconductivity. It was subsequently adapted to nuclei by Bohr, Mottelson and Pines (1958).

The pairing force destroys the sharpness of the Fermi surface of the IPM. Instead of a given state in the vicinity of the Fermi surface being either completely full or empty, it now has to be characterized by some probability of being filled by a pair of particles and a corresponding probability of being empty.

However, if one invokes the concept of quasiparticles, much of the simplicity of the original IPM can be regained: instead of considering particle excitations, one now deals with particle-hole excitations. The energy  $\epsilon_\nu$  of a quasiparticle state  $\nu$  can be determined by the following expression:

$$\epsilon_\nu = \{(E_\nu - \lambda)^2 + \Delta^2\}^{1/2} \quad 2.3.1$$

where  $E_\nu$  is the single particle energy,  $\lambda$  the diffuseness of the Fermi surface, and  $2\Delta$  the pairing energy gap, which can

be measured from differences in the even-odd proton (neutron) separation energies.

#### 2.4 Unified vibrational and rotational model.

Even in the vicinity of magic nuclei, the simple shell model fails to describe properly all the known properties of nuclei. One example is the transition rates of the first excited  $J^\pi=2^+$  states to the  $0^+$  ground states of even-even nuclei: the experimental rates are considerably higher than the single particle values, indicating some degree of collectivity. The total strength may be realized if small deformations in the shape of the nuclear potential are allowed, as considered by Nilsson (1955). Naturally the single particle model falters in the region far from shell closure. The discrepancies in rates can be more than two orders of magnitude!

Historically, many of the properties of the nucleus can be described by the so-called liquid drop model. Indeed, this is the justification of the SEMF. Again, the motions of nucleons are considered to form some kind of average effective potential acting on themselves. Phenomenologically, this is described by volume, surface tension, Coulomb, symmetry, and pairing terms. The first three terms essentially describe a charged liquid drop; the last two take into account that nuclei would prefer to have equal numbers of neutrons and protons, were it not for the Coulomb

force, and that short range correlations result in particles tending to form  $J=0$  pairs.

Such a drop is spherical in shape with excitations described as surface vibrations (vibrational model). It is characterized in part by roughly equal spacings of excited states:

$$E_x \approx n\hbar\omega . \quad 2.4.1$$

However, deformations in the shape can result because of the longer-ranged "aligned coupling". This is due to the tendency of a nucleon to align its orbit with the average field produced by the other nucleons. For sufficiently large deformations, rotations are a natural consequence. Ignoring centrifugal and Coriolis effects, the energy level spacings are proportional to  $J(J+1)$ .

$$E_x \approx \frac{\hbar^2}{2\mathcal{J}} J(J+1) , \quad 2.4.2$$

where  $\mathcal{J}$  is the moment of inertia of the system. Generally,  $\mathcal{J}$  is not equal to the rigid body moment of inertia; rather, only the surface deformed part is involved in the collective motion.

Somewhere between the extremes of the IPM and the collective models must lie a more accurate description of

the nucleus. Their reconciliation can be had by shifting the emphasis from the collective motion of the particle density to that of the independent particle field, as proposed by Bohr (1952) and Bohr and Mottelson (1953). Conversely, one may think of the independent particles moving in a vibrating or rotating field instead of a static one.

A simple extension of the above ideas to describe spectra of odd-even and odd-odd nuclei and excited states of even-even nuclei can be realized in the weak or intermediate coupling models, or more generally, the core excitation models of Lawson and Utretsky (1957) and DeShalit (1961). These coupling models are based on the premise that an even-even spherical nucleus has a simple vibrational spectrum, at least for low lying excitations. If a particle (or hole) is added to such an even-even "core" the resultant possible spin states,  $\vec{J}$ , are due to the angular momentum of the core,  $\vec{\lambda}$ , coupled with that of the added particle,  $\vec{j}$ :

$$\vec{J} = \vec{\lambda} + \vec{j}$$

2.4.3

A weak coupling model has been used to describe  $^{60}\text{Zn}$  by Vo Van and Wong (1977). Some of the odd-zinc isotopes -- though regrettably neither  $^{59}\text{Zn}$  nor  $^{61}\text{Zn}$  -- have been described under the similar heading of quasiparticle-phonon-coupling model by Thankappen (1965), Weidinger (1970)

and Throop (1975). Briefly, a simplified account of the method of Weidinger is as follows: an effective Hamiltonian is broken into three parts:

$$H = H_c + H_p + H_{int} \quad 2.4.4$$

where the three terms represent the core, the particle(s), and the interaction between the two, respectively. The last may be simplified into terms involving spin operators and quadrupole operators between the core (upper case) and the particle (lower case):

$$H_{int} = - \xi (\vec{J} \cdot \vec{j}) - n (\vec{Q} \cdot \vec{q}) \quad 2.4.5$$

where  $\xi$  and  $n$  are coupling parameters to be determined. The matrix elements are then given by:

$$\begin{aligned} \langle J' j'; IM | H | J j; IM \rangle = & \quad 2.4.6 \\ \delta_{JJ'} \delta_{jj'} (E_j + E_J - \frac{1}{2} \xi [I(I+1) - J(J+1) - j(j+1)]) & \\ - n W(2j' J I; j J') \langle J' | Q | J \rangle \langle j' | q | j \rangle & \end{aligned}$$

where  $E_j$ 's and  $E_J$ 's are determined by the quasiparticle and core vibrational energies, respectively, and  $W(2j' J I; j J')$  is a Racah coefficient. The core wavefunctions may not in general be known, but if one restricts the core to only the  $0^+$  and  $2_1^+$  states, then two new quantities may be introduced,

$$x_1 = n \langle 21Q10 \rangle$$

2.4.7

$$x_2 = n \langle 21Q12 \rangle,$$

leaving three free parameters  $\xi$ ,  $x_1$ ,  $x_2$  to adjust empirically.

Obviously the above description can be made more elaborate if additional basis states and/or particles are included. Models for the core itself may become more complicated. For instance, increasing deformation may change the core from spherical to ellipsoidal or even lower symmetry. In fact, the level structures of the even zinc isotopes have been described in terms of an anharmonic vibrator (i.e. the Hamiltonian contains anharmonic terms) by Kisslinger (1967) and Lightbody (1972). Alternatively a "cluster" of particles or quasiparticles may be considered with an extra term in the Hamiltonian describing the interactions within the cluster. Such a model has already been applied to the odd zinc isotopes -- again  $^{59,61}\text{Zn}$  excepted -- with "reasonable" success by Egmond et al (1981). Quartet (cluster of four particles) states in  $^{60}\text{Zn}$  have been calculated by Jaffrin (1972).

One major drawback with most of the above methods is that the number of free parameters may grow rapidly. Also, the parameters are not easily transferrable to other nearby nuclei.

## 2.5 Hartree-Fock-Bogolyubov

The models discussed thus far have generally been developed semi-empirically with few microscopic foundations. These foundations can be established, however, through the formalism of the self-consistent Hartree-Fock-Bogolyubov theories (H, HF, HB, HFB).

Beginning with the Hartree theory, one first considers a Hamiltonian describing the interactions of the nucleus:

$$H = \sum_{i=1}^A T + \frac{1}{2} \sum_{i \neq j}^A v(r_i, r_j) \quad 2.5.1$$

where  $T$  is the kinetic energy operator and  $v(r_i, r_j)$  is the two-body potential between nucleons  $i$  and  $j$ . As an approximation, three (or more) body interactions can be ignored since the energies considered are "relatively" small. Furthermore, the Pauli Principle helps to keep several fermions from coming close together.

The second term is broken into two parts:

$$\frac{1}{2} \sum_{i \neq j}^A v(r_i, r_j) = \sum_{i=1}^A V_0(r_i) + \frac{1}{2} \sum V_R(r_i, r_j) \quad 2.5.2$$

where  $V_0(r_i)$  is a simple effective potential and  $V_R(r_i, r_j)$  is the residual potential. The effective potential is



chosen large enough so that the residual is small and acts as a perturbation.

Ignoring the residual interaction for the time being, the new, simpler Hamiltonian is solved:

$$(-\hbar^2 \nabla^2 / 2m + V_0(r)) \psi_i(r) = \epsilon_i \psi_i(r) \quad 2.5.3$$

with eigenvalues  $\epsilon_i$  and eigenfunctions  $\psi_i$ . The total wavefunction becomes:

$$\psi(1, 2, 3, \dots, A, r) = \prod_{i=1}^A \psi_i(r_i), \quad 2.5.4$$

which is antisymmetrized by adding all the possible even permutations, subtracting the odd permutations and normalizing by  $1/\sqrt{A}$ .

Treating the residual interaction as a perturbation, the average interaction felt by a particle due to all the remaining particles is:

$$U(r_i) = \sum_{j \neq i}^A \iiint \psi_j^*(r_j) V_R(r_i, r_j) \psi_j(r_j) d^3 r_j \quad 2.5.5$$

The new one-body equations

$$(-\hbar^2 \nabla^2 / 2m + V_0(r) + U(r)) \psi_i(r) = \epsilon_i \psi_i(r) \quad 2.5.6$$

are solved and used to generate better wavefunctions and, in turn, better fields. After several iterations, a self consistency between the particle densities and fields is attained.

The Hartree-Fock-Bogolyubov theory is essentially based upon the above approach, but in addition includes exchange terms in the potential. In its more generalized form, it also takes into account both the long and short range parts of the interaction (i.e. BCS theory) to describe, for instance, pairing and time dependence for excited states.

It should be made clear that approximations and truncations generally have to be made to make the calculations amenable to finite computer time and budgets!

HFB calculations have been performed, with limited success, on the zinc isotopes by Chandra (1971, 1972), Parikh (1972), and Sandhu (1975).

## 2.6 Shell model II: the SDI

A different approach to breaking down the multi-body nuclear problem into a series of one-body problems is found in the generalized shell model. In the Ni-Zn region, it is still possible to make use of the isospin formalism, i.e. Coulomb effects aside, the nuclear forces between protons and neutrons are the same.

The starting point is relatively straightforward. Closed shells of both neutrons and protons are assumed to form an inert core. If the closure is of a major shell, then the single particle excitations for a nucleus with an additional particle are large and confined to the next shells. So far this is just the IPM again.

The Hamiltonian can be written into two parts, one involving the core and the other the interaction of the particle with the core,

$$H = H_c + H_{pc} \quad 2.6.1$$

with solutions limited to the next major shell and its subshells. This is justified due to the large energy gaps between major shells (Fig. 1).

If a second particle is added, then some kind of interaction between the two valence particles must come into play:

$$H = H_c + H_{p_1-c} + H_{p_2-c} + H_{p_1 p_2} \quad 2.6.2$$

Semi-microscopically, the two particles can only interact directly with each other when they are close due to the short-ranged nature of the nucleon-nucleon force. Indirectly, they can affect each other at longer ranges via core polarization, but if the core is truly inert, then this long

range interaction can be neglected, at least as a good approximation. A further simplification may be made if the short range interaction is replaced by a  $\delta$  interaction -- hence the expression Surface Delta Interaction model, or SDI.

The last term in 2.6.2 becomes (after Glaudemans)

$$H_{p_1 p_2}(r_i, r_j) = V_{SDI}(ij) = -4\pi A_T \delta(\Omega_{12}) \delta(r_1 - R) \delta(r_2 - R) \quad 2.6.3.$$

where the factor  $-4\pi A_T$  determines the overall strength of the interaction (which may depend on the coupled isospin of the two particles:  $T=0$  or  $1$ ) and the three  $\delta$ 's indicate that the interaction takes place only when both nucleons are at the same place on the surface of the nucleus (radius  $R$ ; the closed core restricts the interaction to the nuclear surface).

For two particles of spin  $j_a, j_b$  and isospin  $t_a, t_b$  in shells  $\lambda_a, \lambda_b$ , coupled to total spin  $J$  and isospin  $T$  (subject to the antisymmetrization requirement), the energy is given by the matrix elements

$$E = \langle \psi | V | \psi \rangle \quad 2.6.4$$

The excitation energies with respect to the ground state become

$$\begin{aligned}
 E_{\text{ex}} &= \langle {}^l_a j_a {}^l_b j_b | V_{\text{SDI}} | {}^l_a j_a {}^l_b j_b \rangle + E_a + E_b - E_{\text{gs}} & 2.6.5 \\
 &= \frac{-A_T (2j_a + 1)(2j_b + 1)}{2(2J+1) (1+\delta_{ab})} \\
 &\quad \{ \langle j_a \frac{1}{2} j_b \frac{1}{2} | J0 \rangle^2 (1 - (-)^{l_a + l_b + J + T}) \\
 &\quad + \langle j_a \frac{1}{2} j_b \frac{1}{2} | J1 \rangle^2 (1 - (-)^T) \} + E_a + E_b - E_{\text{gs}}
 \end{aligned}$$

Complications ensue when there is more than one allowable coupling of  $j$ 's and  $t$ 's yielding the same  $(J^\pi, T)$ . In this case, a general solution is given by a linear combination of the individual solutions. Known as configuration mixing, the linear combination tends to repel closely lying states of the same  $(J^\pi, T)$ .

If a third particle or more is added, the situation naturally becomes more complex. The new situation can be tackled by breaking the  $n$ -body problem into a series of  $(n-1)$ -body problems, considering all possible couplings of the  $n$ 'th particle with the remaining  $(n-1)$  particles.

The general wavefunction of all the  $n$  particles is given by a linear combination of all the antisymmetrized  $(n-1)$ -coupled-to- $n$  wavefunctions multiplied by the appropriate coefficients of fractional parentage (cfp). Symbolically, one has

$$\rho_n / \Gamma = \sum_{\epsilon} \langle \rho_n / \Gamma | \rho_{n-1} / \epsilon \rangle \rho_{n-1} / \Gamma \quad 2.6.6$$

where  $\rho_n / \Gamma$  represents the antisymmetrized wavefunction for  $n$  particles coupled to  $\Gamma(J, T)$  values,

$\rho_{n-1} / \epsilon$  represents the wavefunction for the  $n$ 'th

particle coupled to the  $\epsilon$ 'th permutation of the  $(n-1)$  particles, and the expansion coefficient  $\langle \rho_n / \Gamma | \rho_{n-1} / \epsilon \rangle$  is the cfp.

Again, the dimensionality of the overall problem grows rapidly as the number of particles and/or shells is increased. But there are still certain advantages to this method. The number of free parameters to be determined, either by fitting experimental data or otherwise, can be kept reasonably small:  $A_0$  and  $A_1$  to describe the strength of the SDI,  $A'_0$  and  $A'_1$  to allow for different strengths in the off-diagonal matrix elements if required for the configuration mixing allowance for hole excitations, terms to describe the longer range aspects of the particle-particle interactions, for example, a constant term  $B_T$  (modified surface delta interaction or MSDI<sup>2</sup>, tensor terms, etc. (in the Ni-Cu-Zn region, these are small and negligible, respectively). More importantly, a systematic survey can be done using the same parameters for several nuclei. Indeed, such

a survey has been performed on the zinc isotopes by van Hienen et al. (1976), based upon the earlier nickel-copper survey of Koops and Glaudemans (1977, 1973).

The fundamental assumptions of the above nickel-copper-zinc calculations are a doubly-magic  $^{56}\text{Ni}$  inert core (even though  $^{56}\text{Ni}$  itself is unstable!) with active particles restricted to  $p_{3/2}$ ,  $f_{5/2}$ , and  $p_{1/2}$  shells. Hole-excitations are not allowed directly, rather they are assumed small and their effects incorporated into the remaining parameters. The Hartree-Fock calculations of Chandra et al. (1971, 1972), Parikh (1972) and Sandhu et al. (1975) for zinc, suggest that only  $f_{7/2}$  excitations would contribute and the lack of experimental evidence for hole components in the ground state by stripping reactions (Couch et al. (1970) and von Ehrenstein et al. (1967)) justify this assumption. Any small effects can easily be covered by the effective interactions. The exclusion of  $g_{9/2}$  and  $d_{5/2}$  states does however affect the calculations, at least for the low-lying states of the more neutron rich Ni-Cu-Zn isotopes. Because of the restrictions to the f-p shell, odd-A positive parity states are not predicted at all. For the neutron deficient Ni-Cu-Zn isotopes the  $g_{9/2}^+$  and  $d_{5/2}^+$  exclusions should produce only small effects in the low-lying structure; therefore they need only be incorporated indirectly.

The two-body parameters of the Hamiltonian for the zinc calculations were in fact those used in the nickel-

copper calculations with no additional fitting using experimental zinc properties. Thus the zinc isotopes -- especially the neutron deficient ones -- provide a fertile testing ground for the shell model theory.

### 2.7 Electromagnetic decay properties

The above formalisms may be tested in part by examining binding energies, excitation energies, spins and parities. Properties such as transition rates -- in particular, gamma ( $\gamma$ ) transitions -- and spectroscopic factors may be useful as well.

The emission probability per unit time for a photon of energy  $E_\gamma$ , multipolarity  $\ell$ , and projection  $m$  is given, after Blatt and Weisskopf (1952) by:

$$T(\ell, m) = \frac{8\pi(\ell+1)}{\ell[(2\ell+1)!!]^2} \frac{1}{\pi} \left( \frac{E}{\hbar c} \right)^{2\ell+1} B(\ell, m), \quad 2.7.1$$

where  $B(\ell, m)$  is the reduced transition rate whereby the initial and final states are connected by an electric or magnetic  $2^\ell$ -pole transition operator:

$$B(\ell, m) = \langle f | \Omega_m^\ell | i \rangle^2 \quad 2.7.2$$

subject to the selection rules



$$|J_i - J_f| \leq l \leq J_i + J_f \quad 2.7.3$$

and

$$\begin{aligned} \Pi_i \Pi_f &= (-)^l \quad \text{for electric } 2^l\text{-pole} & 2.7.4 \\ \Pi_i \Pi_f &= (-)^{l+1} \quad \text{for magnetic } 2^l\text{-pole.} \end{aligned}$$

The rates are therefore sensitive to the wavefunctions contained in the electromagnetic matrix elements.

The electric operators may be found from the charge distribution:

$$\Omega_m^l(\text{electric}) = \sum_{i=1}^A e_i r_i^l Y_m^l(\theta_i, \phi_i) \quad 2.7.5$$

(for  $E_\gamma \ll 20$  MeV).

The magnetic operators are much more complicated as they involve gradients and g-factors:

$$\begin{aligned} \Omega_m^l(\text{magnetic}) &= \sum_{i=1}^A [\text{grad } r_i^l Y_m^l(\theta_i, \phi_i)] \frac{2g_i^{(l)}}{l+1} \hat{\lambda}_i \frac{eh}{2m_p c} \\ &+ \sum_{i=1}^A [\text{grad } r_i^l Y_m^l(\theta_i, \phi_i)] \cdot g_i^{(s)} \hat{s}_i \frac{eh}{2m_p c} \end{aligned}$$

(for  $E_\gamma \ll 20$  MeV).

2.7.6

In the shell model the free space values for charges and magnetic moments for the protons and neutrons,

$$e_p = 1 e$$

$$e_n = 0$$

$$g_p^{(1)} = 1 \text{ nm}$$

$$g_n^{(1)} = 0 \text{ nm}$$

$$g_p^{(s)} = 5.585 \text{ nm}$$

$$g_n^{(s)} = -3.826 \text{ nm} ,$$

2.7.7

are replaced by effective values. In particular, the neutron charge and orbital moment become very different from zero. (This can be justified in part by a center-of-mass argument. Also, if only the free value charges are used, the theoretical  $B(E2)$  values are generally too small.)

Under the isospin formalism, the operator  $\Omega_m^l$  can be recast, after Glaudemans (1970), as an isoscalar part minus an isovector part

$$\Omega_m^l = S_m^l \cdot \mathbb{1}_0^0 - V_m^l \cdot \tau_0^1 , \quad 2.7.8$$

with  $S_m^l$  the isoscalar part,  $\mathbb{1}_0^0$  the rank zero identity tensor operator,  $V_m^l$  the isovector part, and  $\tau_0^1$  equal to the isospin tensor operator  $\tau_3$  of rank 1, projection 0. For electric  $2^l$ -poles:

2.7.9

$$S_m^{(l)}(el) = \sum_{i=1}^A \frac{e_p(i) + e_n(i)}{2} r_i^{(l)} Y_m^{(l)}(\theta_i, \phi_i)$$

and

$$V_m^{(l)}(el) = \sum_{i=1}^A \frac{e_p(i) - e_n(i)}{2} r_i^{(l)} Y_m^{(l)}(\theta_i, \phi_i).$$

For magnetic  $2^l$ -poles.

2.7.10

$$S_m^{(l)}(\text{mag}) = \sum_{i=1}^A [\text{grad } r_i^{(l)} Y_m^{(l)}(\theta_i, \phi_i)] \cdot \left[ \frac{g_p^{(l)}(i) + g_n^{(l)}(i)}{2} \frac{2^l i}{l+1} + \frac{g_p^{(s)}(i) + g_n^{(s)}(i)}{2} \vec{s}_i \right] \frac{e\hbar}{2m_p c}$$

$$V_m^{(l)}(\text{mag}) = \sum_{i=1}^A \text{grad } r_i^{(l)} Y_m^{(l)}(\theta_i, \phi_i) \cdot \left[ \frac{g_p^{(l)}(i) - g_n^{(l)}(i)}{2} \frac{2^l i}{l+1} + \frac{g_p^{(s)}(i) - g_n^{(s)}(i)}{2} \vec{s}_i \right] \frac{e\hbar}{2m_p c}$$

The expression for the transition rate becomes:

$$T(\ell, m) = \frac{8\pi(\ell+1)}{\ell[(2\ell+1)!!]^2} \frac{k^{2\ell+1}}{h} \left[ \langle J_f J_{fz} T_f T_{fz} | S_{mz}^\ell \frac{1}{\tau_0} | J_i J_{iz} T_i T_{iz} \rangle + \langle J_f J_{fz} T_f T_{fz} | v_{mz}^\ell \tau_0^{-1} | J_i J_{iz} T_i T_{iz} \rangle \right]^2$$

The total transition rate,  $T(\ell)$ , and reduced rate,  $B(\ell)$ , can be found by taking an average of all the initial magnetic substates, with weighting factors if the populations are not all the same, summed over all possible final states:

2.7.12

$$T(\ell)_{e \text{ or } m} = \frac{8\pi(\ell+1)}{\ell[(2\ell+1)!!]^2} \frac{1}{h} \left( \frac{E_\gamma}{hc} \right)^{2\ell+1} \times \sum_{\substack{J_{iz} \\ J_{fz}}} \frac{T(\ell, m)}{2J_i + 1}$$

$$= \frac{8\pi(\ell+1)}{\ell[(2\ell+1)!!]^2} \frac{1}{h} \left( \frac{E_\gamma}{hc} \right)^{2\ell+1} B(\ell)_{e \text{ or } m}$$

Via the Wigner-Eckart theorem, the  $J_z$  and  $T_z$  dependence can be removed, leaving the reduced  $B(\ell)$  rate in terms of double reduced matrix elements and Clebsch-Gordan coupling coefficients.

$$B(\ell) = \frac{1}{(2J_i+1)(2T_f+1)} [ \langle J_f T_f ||| S^2 \Pi_0^0 ||| J_i T_i \rangle \delta_{T_i T_f} + \langle T_i T_{iz} 10 | T_f T_{fz} \rangle \langle J_f T_f ||| v^{\ell} \tau_0^1 ||| J_i T_i \rangle ]^2 \quad 2.7.13$$

It is convenient to measure the transition rates in Weisskopf units, which are single proton transition estimates:

$$T_w(E, \ell) = \frac{4.4(\ell+1) \times 10^{21}}{\ell [(2\ell+1)!!]^2} \left( \frac{3}{\ell+3} \right)^2 \frac{E_\gamma^{2\ell+1}}{197} R^{2\ell} \text{ sec}^{-1} \quad 2.7.14$$

$$T_w(M, \ell) = \frac{1.9(\ell+1) \times 10^{21}}{\ell [(2\ell+1)!!]^2} \left( \frac{3}{\ell+3} \right)^2 \frac{E_\gamma^{2\ell+1}}{197} R^{2\ell-2} \text{ sec}^{-1}$$

with  $E_\gamma$  in MeV and the nuclear radius  $R$  in fm ( $R = 1.2 A^{1/3}$  fm). The ratios of the actual transition rates over the Weisskopf estimates are then related to the  $B(\ell)$  values by:

$$\frac{T(E, \ell)}{T_w(E, \ell)} = |M.E.|^2 = \frac{4\pi}{\ell^2} \left( \frac{\ell+3}{3} \right)^2 \frac{1}{R^{2\ell}} B(E\ell) \quad 2.7.15$$

$$\frac{T(M, \ell)}{T_w(M, \ell)} = |M.E.|^2 = \frac{\pi}{10} \left( \frac{\ell+3}{3} \right)^2 \frac{1}{R^{2\ell-2}} B(M\ell)$$

(The units of  $B(E\ell)$  and  $B(M\ell)$  are  $e^2 \cdot m^4$  and (nuclear magnetons) $^2 m^{2\ell-2}$ , respectively; M.E. is short for matrix element.)

For M1 transitions, the isovector part is expected to be much greater than the isoscalar part:

2.7.16

$$|M.E.(M1)|_{wu}^2 = S(\text{isoscalar part}) \delta_{T_i T_f} + V(\text{isovector part}) (T_z^2 \delta_{T_i T_f} +$$

$$\langle T_i T_{zi} T_f T_{zf} \rangle (1 - \delta_{T_i T_f}))$$

As can be seen by the Weisskopf estimates, it is possible for E2 transitions to compete with M1's, (E3 with M2, etc.), subject to the selection rules. A measure of this mixing is given by  $\delta$  where

2.7.17

$$\delta \frac{B(E2)}{B(M1)} = \frac{M(E2)}{M(M1)} \left( \frac{T_w(E2)}{T_w(M1)} \right)^{1/2} = \frac{\langle J_f \ell=2 \parallel J_i \rangle}{\langle J_f \ell=1 \parallel J_i \rangle}$$

For a total transition rate  $T$ ,  $\delta^2$  obviously represents the fraction that is E2 in character. Note however, that  $\delta$  itself may be either positive or negative, so careful attention must be paid to a consistent convention regarding

phases. The usual convention of Rose and Brink (1967) will be followed in this project.

Finally, branching ratios represent an additional source of information regarding the nature of the relevant wavefunctions. Branching ratios are a measure of the relative decay of an initial state to a given final state with respect to all possible final states.

### 2.8 Heavy ion induced reactions

In order to study the various nuclear properties, it is first necessary to produce sufficient quantities of the particular isotope under study -- preferably in excited states. This can be accomplished via nuclear reactions. For nuclei near the region of stability, a number of options may be available for use:  $\gamma$ , n, light-ion, heavy-ion induced reactions, (induced) fission, etc., with a host of experimental techniques to study static and dynamic properties.

— In the production of the neutron deficient nuclei  $^{60}\text{Zn}$  and  $^{61}\text{Zn}$ , one is limited to using helium or heavier ions, as a glance at the relevant portion of the chart of the nuclides in Figure 2.2 will quickly verify. Fortunately, these reactions are amenable to the methods of  $\gamma$ -ray spectroscopy, among others (the case for  $^{60}\text{Cu}$  is a little more fortunate in that hydrogen ions (p,d,t) may also be used).

## CHART OF THE NUCLIDES (A~60)

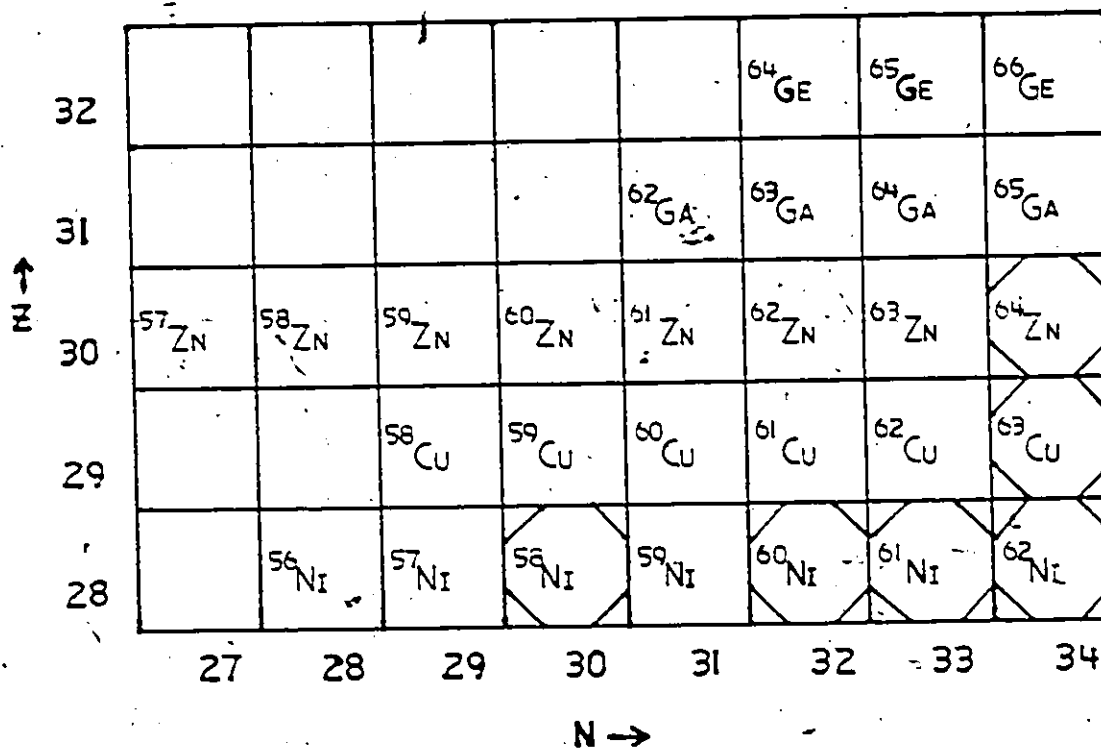


Figure 2.2 Portion of the Chart of Nuclides. Stable isotopes are shown in the octagonal boxes.



An excellent review article on nuclear spectroscopy with heavy ions has been published by Newton (1969); therefore, only the more relevant ideas of the subject will be presented in this chapter. Furthermore, since many of the techniques employed in the present study of  $^{61}\text{Zn}$  are similar to those of  $^{60}\text{Zn}$  (and competing nuclei such as  $^{60}\text{Cu}$ ), only the details for the one will be given, mention being made of any relevant differences. Results and discussion of each of the nuclei will however be presented individually in the following chapters.

Particle induced nuclear reactions may be classified into several types, describable using the following semi-classical arguments. For the case in which the distance of closest approach of a projectile is greater than the range of the nuclear forces between projectile and target, only the long range Coulomb interaction comes into play. The result is either elastic (Rutherford) scattering or Coulomb excitation of the target and/or projectile. If the distance of closest approach is such that a "grazing" collision occurs, i.e. there is only a partial overlap of the nuclear wavefunctions, then particle transfer can take place between the projectile and target nuclei. This is essentially a direct process (though in principle it may involve several steps), characterized by short reaction times of the order of  $10^{-22}$  sec. -- i.e. transit times for the projectile to cross the target nucleus. Finally, if the collision is

almost "head on", a compound nucleus may be formed, followed by a "slow" evaporation of one or more particles (n,p, $\alpha$ ...), the timescale being of the order of  $10^{-16}$  sec. The line of demarcation is not sharp. Generally all three contribute to some extent to the total process, depending on the masses and relative energies involved. At very low energies, Coulomb effects dominate; for moderate energies (several MeV/nucleon), compound nuclear effects; and at higher energies, direct effects.

There can be several advantages to using heavy ions. Because of their mass excesses, even moderately low kinetic energies for a heavy ion projectiles can result in large excitation energies and orbital angular momenta in the compound nucleus (CN). In many instances, the selectivity of the CN reaction leading to a given residual nucleus can be rather high but it is energy dependent as well. The cross-section, or probability for evaporation of (m) particles first increases with energy above threshold, but levels off and then decreases as the (m+1) channel becomes more favourable. Under suitable conditions, the residual nucleus may be far from the valley of stability.

When the barriers inhibiting particle evaporation, such as centrifugal and Coulomb, become large enough,  $\gamma$  decay of the final nucleus can begin to compete. Obviously then, heavy ion reactions lend themselves nicely to in-beam  $\gamma$  spectroscopy. Furthermore, the residual nucleus can

possess sufficiently large linear momentum that Doppler shift measurements of  $\gamma$  lifetimes become feasible, or the nucleus may be allowed to recoil out of the target completely and be transported elsewhere for study.

However, there may be certain disadvantages too. The large Coulomb and compound nuclear effects may severely complicate particle spectroscopy analysis. For instance, the fine details of particle angular distributions characteristic of so many light ion few particle transfer reactions can be totally smeared out. The only information remaining on the orbital angular momentum transferred is contained in the total cross section, which depends strongly on several other factors as well.

## CHAPTER 3

### Experimental Techniques

#### 3.1 Introduction

The experimental investigation of the excited states of  $^{60,61}\text{Zn}$  poses several problems. As alluded to above, heavy ions must be used as both  $^{60,61}\text{Zn}$  are many neutrons removed from the valley of stability. The "simplest" reactions are  $^{58}\text{Ni}(\alpha, n)^{61}\text{Zn}$ ,  $^{58}\text{Ni}(\alpha, 2n)^{60}\text{Zn}$  and  $^{58}\text{Ni}(\tau, n)^{60}\text{Zn}$ , (where  $\tau$  will be used to denote a  $^3\text{He}$  projectile) with  $Q$  values of the order  $-10$ ,  $-19$ , and  $-2$  MeV, respectively. Because of the small Coulomb barriers in this  $A=60$  region (5 MeV/proton), charged particle emission leading to nuclei less neutron deficient than  $^{60,61}\text{Zn}$  is favoured by an order of magnitude (Cumming (1959)). In addition, these competing nuclei are rich in accessible states. One is then faced with the arduous task of sifting through a "sea" of more numerous and intense  $\gamma$ -rays belonging to competing nuclei in order to study the  $\gamma$ -rays of interest.

A more useful approach is to measure the  $\gamma$ -rays appearing in "prompt" coincidence with emitted neutrons. (Since the  $\gamma$  lifetimes are generally much shorter than the timing resolution of the electronics (a few nsec), "prompt" can be extended from a few nanoseconds to a few micro-

seconds, isomers being very rare in the neutron deficient Ni-Zn region.) One drawback is the drastically reduced net counting rate, as both neutron and  $\gamma$  detectors have small efficiencies. Also, projectile energies must be chosen low enough so that pn or nn emission is either reduced or prohibited. Having identified the  $\gamma$ -rays in the above manner, their yields were measured as a function of projectile energy and angle both with and without the neutron "filter". (Additional benefits of n- $\gamma$  coincidence are described below.) The order of the  $\gamma$ -rays appearing in cascades was determined by performing n- $\gamma$  and n- $\gamma$ - $\gamma$  experiments, in conjunction with any information on intensities and energy sums.

Once the identity of several levels was established, heavier ion induced reactions were investigated with the aim of finding properties of levels with higher excitation and spin. The following reactions were examined:  ${}^6\text{Li}$  on  ${}^{58}\text{Ni}$ ,  ${}^{10}\text{B}$  on  ${}^{54}\text{Fe}$ ,  ${}^{16}\text{O}$  on  ${}^{50}\text{Cr}$ ,  ${}^{24}\text{Mg}$  on (natural) Ca, and  ${}^{23}\text{Na}$  on Ca. Again,  $\gamma$  yield curves were measured. Multi- $\gamma$  coincident experiments were performed on the Mg and Na on Ca reactions with use made of a multiplicity filter (MPF).

Production of  ${}^{60}\text{Cu}$  was unavoidable in many cases. Because of the larger cross-sections and greater level of information already known about low lying states, a particle- $\gamma$  identification experiment was not performed for  ${}^{60}\text{Cu}$ . Instead, more reliance was placed upon  $\gamma$ - $\gamma$  coinci-

dence and energy sums data. Other competing channels were examined in this fashion as well.

Finally, several attempts were made, with limited success, to obtain particle spectra via the following reactions:  $^{58}\text{Ni}(^6\text{Li}, t)^{61}\text{Zn}$ ,  $^{59}\text{Fe}(^{10}\text{B}, t)^{61}\text{Zn}$ , and  $^{58}\text{Ni}(\alpha, n)^{61}\text{Zn}$ . The first of these has already been performed by Woods et al. (1978). The aim in repeating the experiment here was to find any levels obscured in the experiment of Woods et al. by reactions on contaminants (e.g.  $^{12}\text{C}$ ) by using self-supporting targets as well as to resolve some of the more closely lying states. The second reaction was inspired by the success of the corresponding  $\gamma$  experiments. Although several attempts were made, neither of the two experiments was successful. (Small cross sections ( $\sim \mu\text{b}$ ) coupled with equipment breakdowns were the culprits responsible for this.) The  $(\alpha, n)$  experiment was, on the other hand, far more successful. Spectra of reaction neutrons at  $90^\circ$  (lab) have been obtained using a SEFORAD neutron detector.

### 3.2 Production of Projectiles

Ions of  $^3\text{He}$  or  $^4\text{He}$  were produced in a standard duoplasmatron (D/P) positive ion source in conjunction with a Li or Na vapour charge exchange canal. (A recovery unit was used to recycle precious  $^3\text{He}$  gas, otherwise lost.) The emerging  $(^3)^4\text{He}^-$  beam had an energy of 46 keV prior to

injection into the McMaster University Tandem van de Graaff accelerator.

Sodium and  ${}^6\text{Li}$  ions were also produced using the D/P source, but as secondary beams: an intense 40 keV  $\text{H}^+$  beam collides with the Na or Li vapour in the canal.

A Triconex cesium sputter source was used to create ion beams of  $\text{Mg}^-$ ,  $\text{MgO}^-$ ,  $\text{B}^-$ ,  $\text{BO}^-$ ,  $\text{O}^-$ , as well as  ${}^6\text{Li}^-$  (less intense but more stable and of longer duration than from the D/P source). Ions were sputtered from a cone of the appropriate material (usually an oxide mixed with silver for better thermal conductivity) by a cesium beam. The ions acquire a net negative charge by passing through a thin cesium film on the surface of the cone before being accelerated to 23 keV. Unwanted ion species are partially removed from the beam by a  $30^\circ$  inflection magnet prior to injection.

In the main accelerator, the negative ion beam was accelerated towards a terminal of potential  $V$ , charge exchanged by a gas and/or foil stripper inside the terminal to a given charge state ( $+n$ ) before being further accelerated. (Gas stripping was used when only a low charge state was desired, or to dissociate the molecular ions prior to stripping by the foil.) The emerging positive ion beam acquires a total energy of  $(n+M_I/M_M)$  eV + injection energy, where  $M_I$  and  $M_M$  are the final ion and molecular masses, respectively.

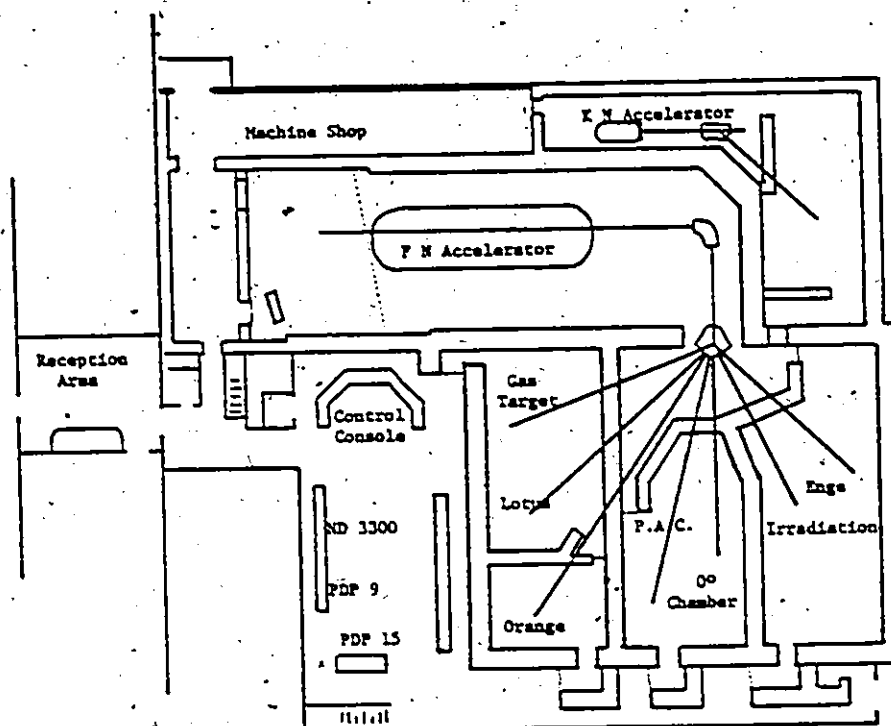
After acceleration, the beam was momentum analyzed by a  $90^\circ$  magnet/slit system. (Beam striking the slits provided feedback signal to control the terminal voltage, hence beam energy.) Fine tuning of the beam profile was accomplished by electrostatic and magnetic steerers, gridded lenses, and magnetic quadrupoles situated at strategic locations along the beam path. A switching magnet was used to send the beam to one of the selected target stations: the  $0^\circ$  line particle scattering chamber,  $45^\circ$  line Lotus  $\gamma$  spectrometer, and the  $-42^\circ$  line Enge spectrometer. A general schematic of the beam transport system is given in Figure 3.1.

### 3.3 Target preparation, target chambers

Targets for the  $\gamma$  experiments were made by rolling small lumps of either  $^{58}\text{Ni}$  (enriched to  $> 99.5\%$ ),  $^{54}\text{Fe}$  ( $> 99\%$ ),  $^{50}\text{Cr}$  ( $> 90\%$ ), or natural Ca (chem. grade;  $97\%$   $^{40}\text{Ca}$ ) into foils a few  $\text{mg}/\text{cm}^2$  thick and several  $\text{cm}^2$  in area. (For the Ca targets, much of the CaO crust flaked away during the rolling process; however, rolling and transfer to the target vacuum chamber had to be rapid to minimize fresh oxidation.) Some of the  $^3\text{He}$  induced  $\gamma$  experiments required a target thick enough to stop the beam, the order of  $100 \text{ mg}/\text{cm}^2$ , due to problems encountered with reactions in beam dump materials.

The targets were mounted onto tungsten wire rings. These rings were supported by rigid tungsten wires connected





TANDEM ACCELERATOR LABORATORY

Figure 3.1. Layout of facilities at the McMaster Tandem Accelerator Laboratory.

to a remote (1 - 10 cm) beam dump of either gold or  $^{208}\text{Pb}$ . The more remote beam dumps were surrounded with lead wrapped in cadmium foil to shield the  $\gamma$  detectors against any activity -- both prompt and delayed -- from the beam dump. The beam dump was employed to monitor the beam intensity. Currents typically of the order of 1 nA were used, limited by the count rate capacity of the data acquisition system. Two 2 mm diameter tantalum apertures placed upstream of the target helped to ensure good collimation of the beam.

Initially a target chamber consisting of 3/8" diameter, thin walled stainless steel tubing was used; however this proved to be unsatisfactory for several reasons, the main one being that portions of the beam would strike the walls despite the good collimation. Partial absorption of the low energy  $\gamma$ -rays was a much less significant problem. The remaining  $\gamma$  experiments involved the use of either a 1" diameter thin walled tantalum tube or 1" diameter plastic tube. The latter was often lined with thin tantalum or gold foil (~ .001") except in the immediate vicinity of the target as viewed by the detectors. Careful attention was placed on alignment of the beam line, apertures, target and chamber, and minimization of any beam current on the apertures. For some of the  $\gamma$  angular distribution measurements a (vertical) cylindrical plastic chamber was employed.

The targets for the particle experiments had to be much thinner in order to minimize degradation of the energy

due to straggling. They also had to be free of any backings or other contaminants that would produce particles in the range of interest. Self-supporting targets of  $^{58}\text{Ni}$  and  $^{54}\text{Fe}$  in thicknesses ranging from 40 to  $120 \text{ } \mu\text{g}/\text{cm}^2$  were prepared by Dr. Y. Peng. The material was vacuum deposited onto a substrate which was then removed by dissolving in a solvent or, in the case of thin zapon backings, evaporated away during the subsequent high energy ion beam bombardment. The targets were mounted either onto a standard aluminum frame (1" square with 1/2" dia. hole) or, for the ( $\alpha$ ,n) experiments, a 1/2" dia. aluminum ring with 3/8" hole.

For the ( $\alpha$ ,n) experiments, the beam dump was located 1.5 m downstream from the target and surrounded by lead, borax, and cadmium to shield the neutron detector against  $\gamma$ -rays and neutrons from the beam dump. Slits and apertures upstream of the target ensured good collimation of the beam. Currents of the order of hundreds of nanoamps were used, limited either by the count rate capacity or beam availability.

### 3.4 Detectors

#### 3.4.1 $\gamma$ detectors

Over the course of this project, many different  $\gamma$  detectors were used. These ran the gamut of the intrinsic Ge and Ge(Li) semiconductor detectors then available at the McMaster facility: 10 cc, 15 cc (int., planar), 37 cc, 42

cc, 50 cc old, 50 cc new, 65 cc, 11% (int.), 17%, 25%, 26%. (the % refers to the efficiency with respect to a 3"  $\times$  3" (3" diameter by 3" length) NaI (Tl) detector; the underlined detectors were those with superior characteristics). The smaller detectors tend to have better energy resolution than the larger ones, but at the expense of efficiency. (Recent developments in crystal growing technology account for the manufacture of larger, more efficient and better resolution detectors.) Unfortunately the resolution can (and does) degrade with age, count rate, level of neutron damage from prior runs, and any extraneous electrical "noise" not filtered out by the electronics. Values for resolution ranged from 0.8 keV FWHM @ 122 keV  $\gamma$  for the 15 cc planar to ~ 2 keV FWHM @ 1.3 MeV for the "better" detectors (11%, 25%, 26% (when new)), to 3 - 6 keV FWHM @ 1.3 MeV  $\gamma$  for the others.

For the experiments involving the MPF (q.v.), several large volume NaI (Tl) detectors (six @ 5"  $\times$  5", one @ 3"  $\times$  3") were used in conjunction with five large Ge/Ge(Li)'s. However, only the event information of the NaI's was employed, since their resolution was drastically inferior: ~ 100 keV FWHM @ 1.3 MeV  $\gamma$ . Useful energy information from the Ge/Ge(Li) detectors was made available by linear shaping amplifiers (normally a differentiation time constant of 2  $\mu$ sec was used). "Slow"-timing signals were obtained from the linear amplifiers via single channel analysers (SCA)

operating in the cross-over mode. "Fast"-timing (few nsec FWHM) was performed using standard constant fraction discrimination (CFD) of signals previously shaped (20 nsec differentiation/20 nsec integration or 200 nsec diff/0 nsec int) and amplified by timing filter amplifiers (TFA).

Signals were then processed by analog to digital converters (ADC's) (gated when necessary if various requirements were fulfilled), which were interfaced with a computer (more details below). The basic block diagrams of the  $\gamma$  electronics are shown in Figure 3.2.

Energy and efficiency calibrations were obtained using both commercial and "in-target"  $\gamma$  sources. The latter, though less accurately known, tended to be more reliable for several reasons: the energy signals are slightly dependent on geometry and count rates and may even be subject to long term drifting; overall efficiencies are very sensitive to geometries of the detectors and any shielding materials between the  $\gamma$  source and detectors; furthermore, the depletion volume of the detectors can vary with age, so efficiency curves must be recorded regularly.

#### 3.4.2 Neutron detectors

In some of the  $\gamma$  experiments, detection of  $\gamma$ -rays from competing reactions was suppressed by using a neutron detector in coincidence with the  $\gamma$  detector(s). For this purpose a 2.5"  $\times$  3" NE218 liquid scintillator was employed.

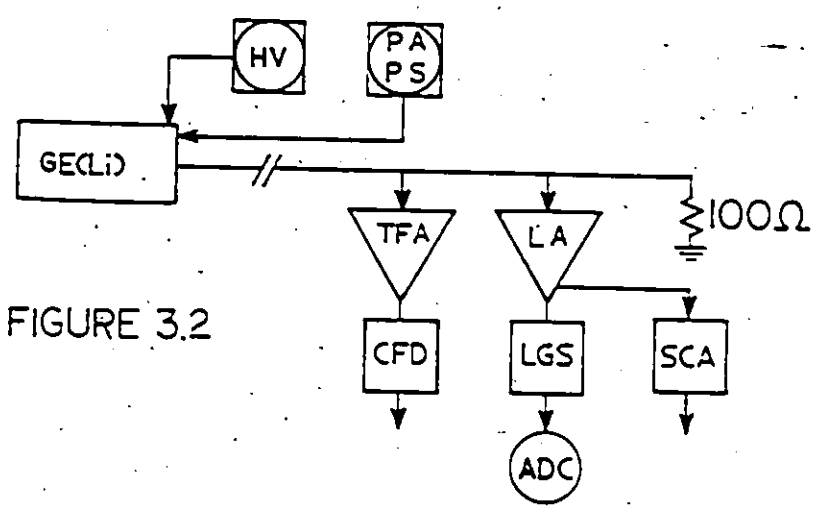


FIGURE 3.2

Block diagram for  $\gamma$  detector electronics

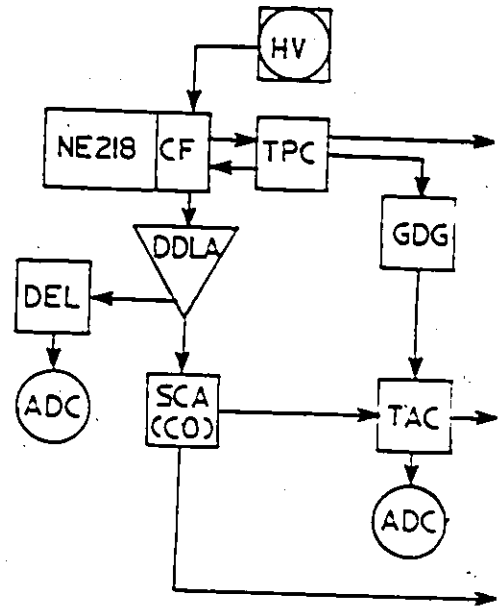


FIGURE 3.3

Block diagram for neutron detector electronics

The scintillation output was detected by a RCA 8575 fast photomultiplier (PM) tube coupled to an Ortec model 270 constant fraction timing base/power supply. Because the neutron detector is also sensitive to  $\gamma$  rays by the Compton effect, it was necessary to shield the detector with 1 - 2" of lead wrapped in cadmium foil to attenuate the  $\gamma$ /x-ray flux and to employ the standard technique of pulse shape discrimination analysis (PSA) of Geddie and McDonald (1967, 1968). By comparing constant fraction timing with cross-over timing differences in the pulse shape for neutron-converted-to-proton recoil or  $\gamma$ -converted-to-electron induced events in the scintillator can be distinguished (the former has a decay time, of the order of tens of nsec longer than the latter). The diagram outlining the electronics used for this is shown in Figure 3.3. [Note that the PSA here depends to some extent upon the pulse height (PH).] Figures 3.4 and 3.5 give examples of the typical pulse shape and pulse height analysis spectra obtained for the reactions studied here. If a very large dynamic range is to be realized, faster photomultiplier tubes, more stable electronics, and a two dimensional neutron pulse height-pulse shape analysis should be used. Recently better electronic devices have become available (Ortec) that provide superior pulse shape analysis over a very wide dynamic range. Unfortunately, all the ancillary electronics were not available for use at the McMaster facility.

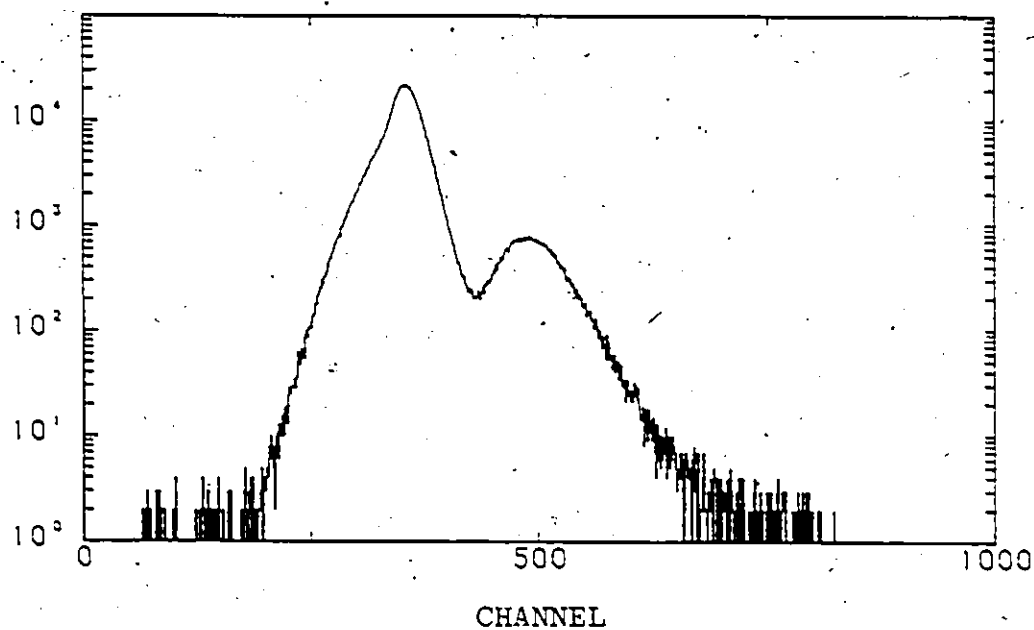


Figure 3.4. Typical neutron detector pulse shape spectrum obtained in these experiments. (Note the overwhelming number of  $\gamma$  events in the left hand peak; the right hand peak corresponds to neutron events.)



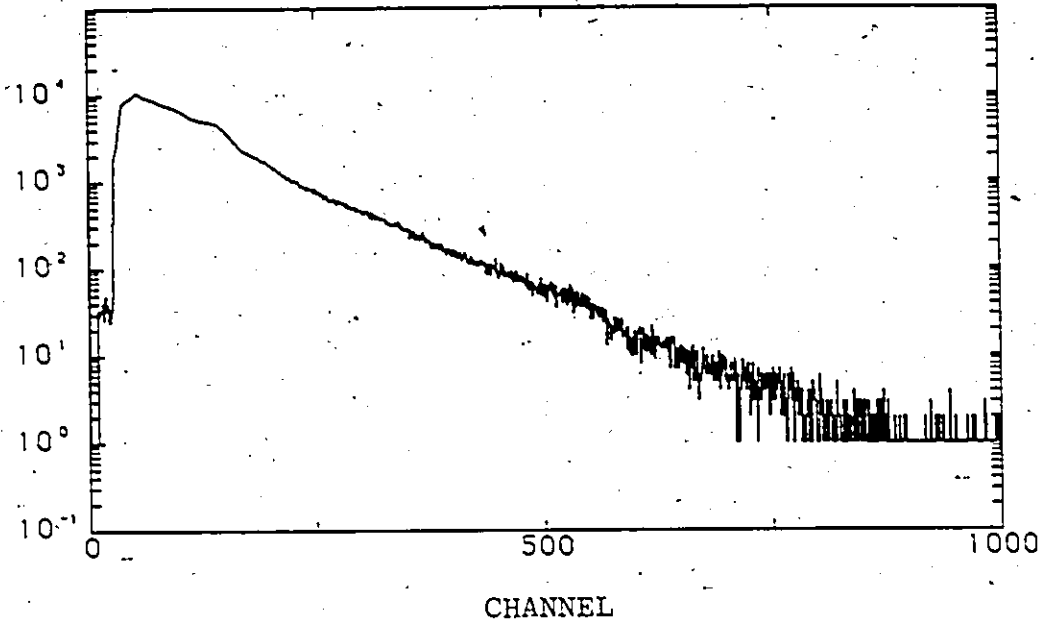


Figure 3.5. Typical neutron detector pulse height spectrum obtained in these experiments.

The proton recoil signal from the scintillator is not sufficient to determine the neutron's energy uniquely. The usual method to obtain energy information is by time-of-flight (TOF), whereby the neutron velocity is measured by the time required to cross a fixed distance. This obviously requires rapidly pulsed beams, long flight paths, and high efficiency neutron detectors with good timing and  $\gamma$  suppression characteristics if adequate resolution is to be achieved. Instead, an alternate method employing secondary reactions was used.  $^3\text{He}$  has a "reasonably" large and flat neutron capture cross section (few barns) for neutrons below 3 MeV, with a 0.781 MeV Q-value. It also has a large elastic-scattering cross section and, above 3 MeV, an increasing  $^3\text{He}(n,d)d$  cross section. By any of these processes, the neutron can be essentially "transformed" into a detectable ionizing charged particle whose energy can be easily measured in a proportional counter or ionization chamber (the  $^3\text{He}$  gas acts both as neutron converter and ionizing medium).

One such proportional counter, manufactured by Harshaw, was tried. However, its efficiency and resolution ( $> 70$  keV @  $E_n = 0$ , worse at higher energies) were too poor to be useful. A counter manufactured by Seforad (on loan from the McMaster University Nuclear Reactor) yielded much more satisfactory results. Its superior efficiency stems from its greater effective volume (larger size (7 x 30 cm),

greater pressure (3 atmos.) of  $^3\text{He}$ ) than the Harshaw detector (1  $\times$  10 cm, 1 atmos.). Operation in the ion chamber mode, use of a very sensitive FET, and shielding of the central wire by a grid, provide the Seforad detector with superior resolution (15 keV for epithermals, 30 keV @ 2 MeV n). However, it does present certain drawbacks. It is intended to be used broadside instead of the more common end-on geometry, since it was designed primarily for  $\gamma$ -induced neutron experiments. This means, that if maximum resolution is to be achieved in a particle induced reaction, the counter must be situated at  $90^\circ$  to the beam direction in order to minimize the kinematic spread of neutron energies due to geometry. (The end-on geometry is not suitable due to various materials in the way.) Even so, an angular spread of  $5^\circ$  represents an energy spread of 50 keV for the  $^{58}\text{Ni}(\alpha, n)$  reaction at 13 MeV. Needless to say, many (multi) particle transfer cross sections are much smaller near  $90^\circ$  than near more forward angles! Also, the large ion drift times make any n- $\gamma$  coincidence experiment infeasible.

The resulting neutron spectrum is very reminiscent of a  $\gamma$ -ray spectrum: there are full energy peaks due to direct capture (cf. photoelectric effect of  $\gamma$ 's) broadened on the low energy side by forward scattering if there is any appreciable material between the source and detector (true for  $\gamma$ 's as well), a low energy edge due to n -  $^3\text{He}$  elastic recoil (cf. Compton scattering) forming an almost exponen-

tial background under the full energy peaks, and multiple peaks for  $E_n > 3$  MeV due to competing processes (cf. pair production). Complicating matters is the sensitivity of the detector to  $\gamma$ -rays via the Compton process. In principle pulse shape analysis can be used to help distinguish  $n - {}^3, {}^4\text{He}^+$  from  $\gamma - e^-$  events, but this is complicated by the large variations in pulse heights and shapes, even for the same kind of events. However, the positive 0.781 MeV Q-value for neutron capture ensures that most  $\gamma$  signals are well below this threshold. The detector is also very sensitive to thermal and epithermal neutrons produced by multiple scattering in walls, floors, etc. These can be reduced by surrounding the detector with a thin cadmium sheet. The epithermal peak will still provide a useful calibration point. A lead sheet will also aid in attenuating the  $\gamma$  flux, but it cannot be too thick lest forward scattering of neutrons in the lead degrade the energy resolution.

An excellent treatment of the characteristics and operation of this Seifrad detector may be found in the thesis of McFee (1977). An efficiency curve for this detector (from McFee) is shown in Figure 3.6.

### 3.4.3 Charged-particle detectors

Several techniques were employed in the study of the  $({}^6\text{Li}, t)$  and  $({}^{10}\text{B}, t)$  charged particle reactions. An Enge

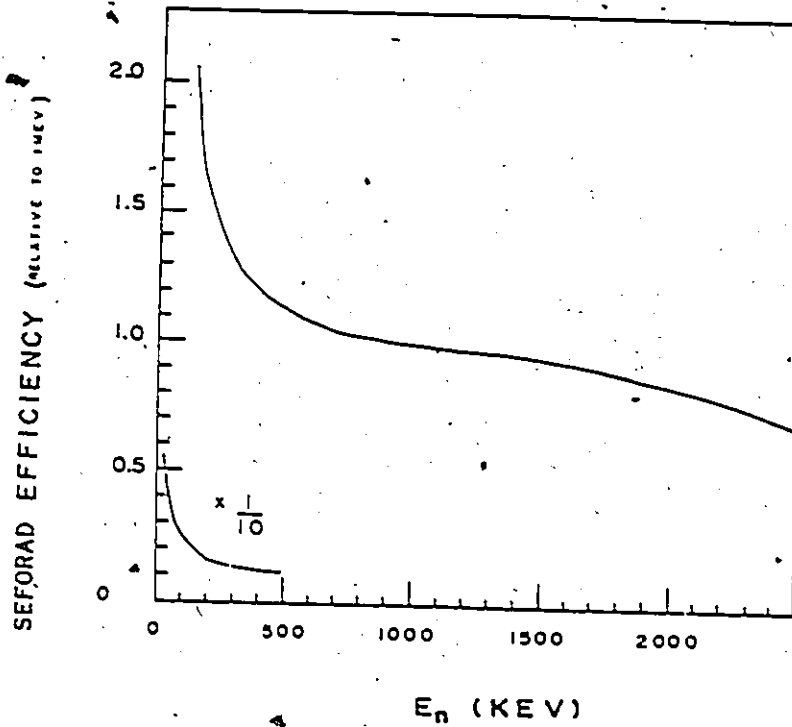


Figure 3.6. Seforad  $^3\text{He}$  ion chamber efficiency curve (from McFee, 1977).

magnetic spectrometer was used to analyze the momentum of reaction particles. These were detected either by a nuclear emulsion photographic plate or a position sensitive delay line counter/E (total energy) scintillator. Unfortunately, several problems were encountered, namely "bad" plates (incorrectly labelled, they were of the wrong type), or too many "spurions" caused by breakdowns and cosmic ray events in the DL counter coupled with very poor resolution. Once these were corrected, new problems arose: machine instability, insufficient beam intensity, and finally inability of the spectrometer's power supply to further provide the necessary high magnet currents to bend 20 - 30 MeV tritons. (At this time of writing, the power supply is still being repaired/upgraded.)

Another attempt was made to study these reactions using a surface barrier  $\Delta E/E$  particle telescope. Two detectors, a 200  $\mu\text{g}/\text{cm}^2$  Si transmission ( $\Delta E$ ) counter followed by a 2000  $\mu\text{g}/\text{cm}^2$  energy (E) counter were employed for this purpose. Unfortunately, the resolution in either counter was insufficient to separate the triton groups from the overwhelming proton, deuteron, and alpha groups. The alphas could be removed by placing a sufficiently thick piece of aluminum foil in front of the telescope, at the expense of degrading the p/d/t resolution through straggling. Eventually the resolution deteriorated with time to

the point where any details of the energy spectra were obliterated.

Thus no new information from the particle experiments  $^{58}\text{Ni}(^6\text{Li}, t)^{61}\text{Zn}$ ,  $^{54}\text{Fe}(^{10}\text{B}, t)$  or even competing reactions  $^{58}\text{Ni}(^6\text{Li}, \alpha)^{60}\text{Cu}$ ,  $^{54}\text{Fe}(^{10}\text{B}, \alpha)^{60}\text{Cu}$  was obtained. No further attempts have been made in this project to study these or other (HI, charged particle) reactions.

### 3.5 Prompt $\gamma$ studies

#### 3.5.1 $\gamma$ Singles

In the singles experiments pulses from the Ge/Ge(Li)'s were suitably amplified and shaped before being fed to ADC's interfaced to either a PDP-9, or more recently, a PDP-11/VAX750 computer. (Occasionally a Tracor Northern TN 1710 multichannel analyzer was pressed into service as well.) Programs used for data acquisition were ADCS and XSYS/TDLC for the PDP-9 and VAX, respectively. The collected data were transferred onto dectapes (PDP-9) or floppy disks (VAX) for further off-line analysis.

Peak areas, centroids, energy calibrations and appropriate errors for well resolved peaks were calculated using the program SOFT on the PDP-15 or an equivalent program found in the VAX operating system. Some gross and net areas were also found by setting windows in the on-line programs. The PDP-15 program GSFIT5 was used to analyze multiplets, with careful attention paid to variations in

parameters. (More sophisticated analysis programs such as SPECTRE and JAGSPLOT on the CDC Cyber or T4VJ, T4RS, and SAMPO on the VAX tended to give unreliable results. A new version of SAMPO and a new program T4RBS designed to find and fit empirically shaped peaks and backgrounds is still in the process of development at this time of writing.) Documentation for these and other programs (listed below) may be found in the Program Library of the McMaster Tandem Accelerator Laboratory.

### 3.5.2 Yield curves

Yield curves provide a measure of specific and/or general activities under varying initial conditions, most notably beam energy. They are useful for several reasons. On a broad scale they aid in the selection of the optimum conditions for production of a given nuclear species. If the beam energy resolution and/or energy loss is much less than the average level spacings of the compound nuclear and/or residual nuclear systems, sharp resonances may be seen, corresponding to the matching of beam energies with energy levels. At higher energies or with poorer resolution, the CN system has essentially a continuum of available states so that rapid fluctuations in the yield average out and the small scale structure becomes featureless, as is the case of the reactions investigated in this project. On a



smaller scale, useful information may be obtained by measuring yields of individual  $\gamma$ -rays.

Above energy threshold the population of a specific bound level (followed by subsequent  $\gamma$  emission) is a statistical process governed by energy available to overcome any potential barriers. The population is expected to increase smoothly with energy but taper off again as other exit channels begin to compete more favourably. Because of the centrifugal barrier, the initial shape of a  $\gamma$  yield curve may depend on the angular momentum of the level in addition to any particle incoming/outgoing Coulomb barriers or other nuclear properties. Many of these "extraneous" Coulomb features can be cancelled out in part if the yield of a  $\gamma$  ray is measured relative to another one, preferably corresponding to a low lying initial state of known spin. Empirically, the low energy portions of these relative yield curves, after an initially steep rise, are often nearly exponential with energy. On a log-linear scale the slope reflects the relative spin of the initial level, a steeper slope corresponding to a larger value of spin.

Well above threshold, the exponential shapes break down. As the particle "side feeding" of a level tapers off,  $\gamma$  production may still be on the increase due to "top feeding" by  $\gamma$ -rays from levels higher up. For nuclei with low spin ground states, most bound levels  $\gamma$  decay to intermediate ones. Thus the yield of just a few  $\gamma$ -rays corre-

sponding to low lying transitions can provide a measure of the total cross section relative to competing reactions.

### 3.5.3 n- $\gamma$ Coincidence measurements

As has been previously stated, it was necessary to identify  $\gamma$ -rays belonging to  $^{60}\text{Zn}$  or  $^{61}\text{Zn}$  using the neutron coincidence signature. Several problems with the circuit of Figure 3.3 were encountered. The pulse shape analyzer of this circuit is somewhat dependent upon the pulse height; coupled with the low relative yield of neutrons (even with lead  $\gamma$  shielding) and drifting in the electronics, this made total rejection of  $\gamma$  events in the neutron detector (henceforth called  $\bar{n}$  events) very difficult. Stronger  $\gamma$ - $\gamma$  events from competing reactions can intrude into the n- $\gamma$  coincidence spectrum.

After some experimentation, the following provided the optimum remedy (short of purchasing new detectors and electronics):

- 1" - 2" of lead shielding placed in front and around the sides of the neutron detector, wrapped in cadmium and copper sheets to absorb X-rays from fluorescence in the shielding
- maintaining the count rate in the detector to  $\leq 2,000$  counts/sec
- air cooling of the detector and electronics to reduce drifting

- most importantly, address recording of the event information onto magtapes (PDP-9 program EVR), including the fast n- $\gamma$  timing, neutron detector pulse height and pulse shape signals and  $\gamma$  energy.

Several advantages were gained by address recording "everything":

- multi dimensional windows could be set to optimize the neutron detector pulse shape analysis
- the separated  $\bar{n}$ - $\gamma$  spectra could still provide good internal energy calibration
- any sudden (or gradual) changes in the electronics such as gain drifts could be more readily accommodated
- corrections for chance coincidences and  $\bar{n}\gamma$  events "sneaking" into the n- $\gamma$  spectra could be made, the latter by subtracting spectra collected from windows near the  $\bar{n}/n$  boundary after suitable normalization to known  $\bar{n}$ - $\gamma$  lines intruding in the n- $\gamma$  spectra; because of the energy dependence of the neutron pulse shape analysis, the total  $\bar{n}\gamma$  spectra are not suitable for subtracting except in a qualitative manner, as some  $\bar{n}\gamma$  intrusions are over compensated while others remain under compensated. This is illustrated in Figures 4.14 and 5.3 for  $^{58}\text{Ni}(\alpha, n\gamma)^{61}\text{Zn}$  and  $^{58}\text{Ni}(r, n\gamma)^{60}\text{Zn}$  spectra where tantalum beam dumps were used. Therefore the efficiency of the neutron detector need not be compromised by raising the PSA threshold and restricting the dynamic range of accepted pulses.

#### 3.5.4 $\gamma$ - $\gamma$ Coincidence measurements

For the  $(\alpha, n\gamma)^{61}\text{Zn}$  and  $(\tau, n\gamma)^{60}\text{Zn}$   $\gamma$ - $\gamma$  coincidence experiments, the coincidence fast timing (TAC) and energy signals from a pair of Ge/Ge(Li) detectors were address recorded onto magtape by the PDP-9 computer using program EVR. (The two  $\gamma$  detectors were both in the  $90^\circ$  plane to minimize Doppler shifts, offset from the beam axis and partially shielded from each other by  $1/2'' - 1''$  Pb or Ta plates to reduce backscattering and positron annihilation events. A neutron detector was usually placed at  $0^\circ$  immediately behind the beam dump.) Off-line sorting of the events was performed by the PDP-15 computer using program DSEH2 or one of its variants: BATMAN, SRTMEM, etc. With these programs, windows could be set on selected peaks and backgrounds on either side of the peaks from one detector. Additional windows on the prompt and background portion of the TAC spectra were set as well. The collected spectra of the second detector were thus corrected for backgrounds due to any "chance" coincidences or Compton events under the peaks in the windows. For partially resolved peaks, windows had to be set more carefully. Background windows for a given peak were selected to include appropriate components of the neighbouring peak(s) to compensate for any contributions it might make. (This method, when carefully executed, proved to be reliable though rather tedious.)

Normally a singles monitor spectrum, usually hardware gated by coincidence requirements with a neutron detector, was recorded at the same time into the data memory and later transferred to dectape.

A typical (n)  $\gamma$ - $\gamma$  coincidence circuit used in these experiments is shown in Figure 3.7.

### 3.5.5 Multiple- $\gamma$ events; MPF

The multiplicity filter was pressed into service in the search for higher excitations and spin states. The MPF operates on the premise that a high spin/energy state decays to the ground state through a cascade of  $\gamma$  emissions. If several  $\gamma$ -rays are detected coincidentally in a large array of detectors, then these  $\gamma$ -rays must belong to such a cascade. It is not necessary that all the detectors possess good energy resolution. The poorer ones (NaI) need only provide multiplicity information via hardware to gate the superior Ge/Ge(Li) detectors. The total energy deposited in the array per event, indicative of the total excitation energy, can in principle be used as an additional parameter but was not used in these experiments as the high spins sought are modest in comparison with those seen in the rare-earth region, for instance.

For the  $^{24}\text{Mg}$  and  $^{23}\text{Na}$  on calcium experiments investigated in this project, typically six NaI(Tl)'s and five large volume Ge/Ge(Li)'s were used, the latter providing

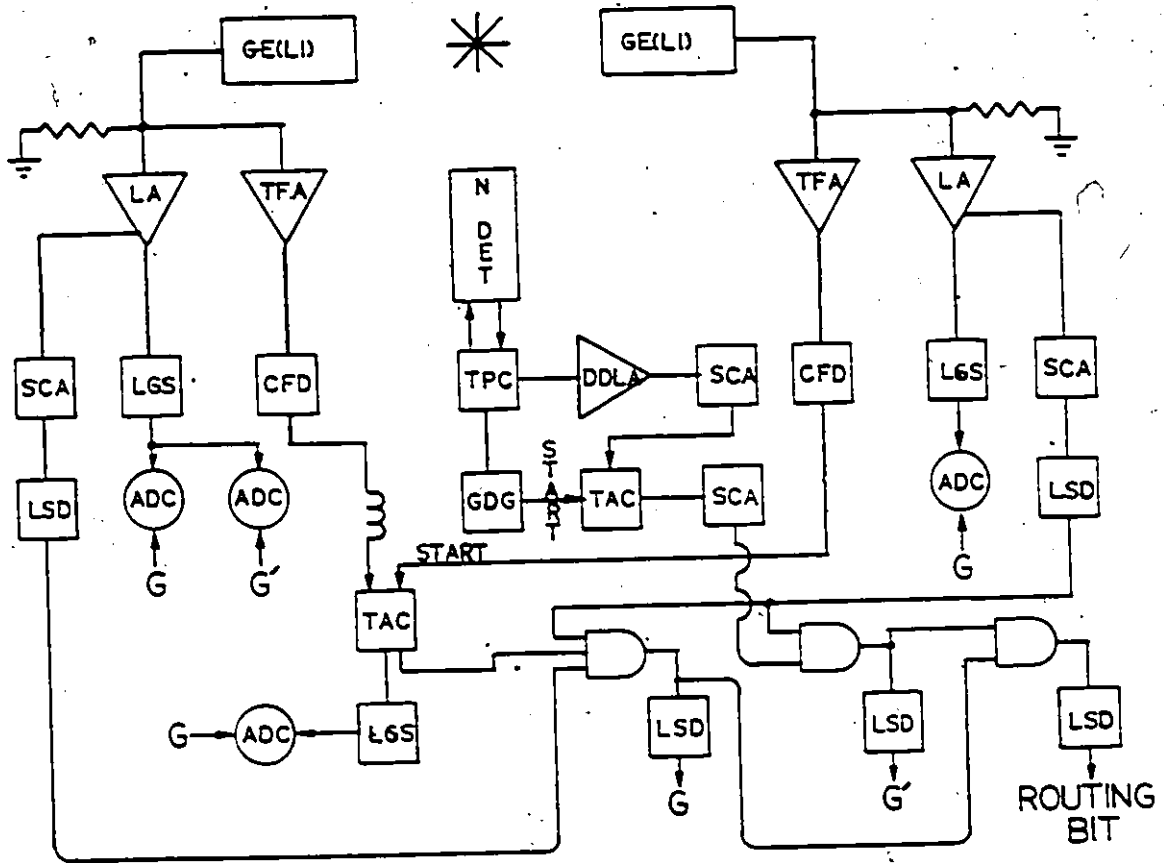


Figure 3.7 i. Typical  $\gamma$ - $\gamma$  coincidence circuit.

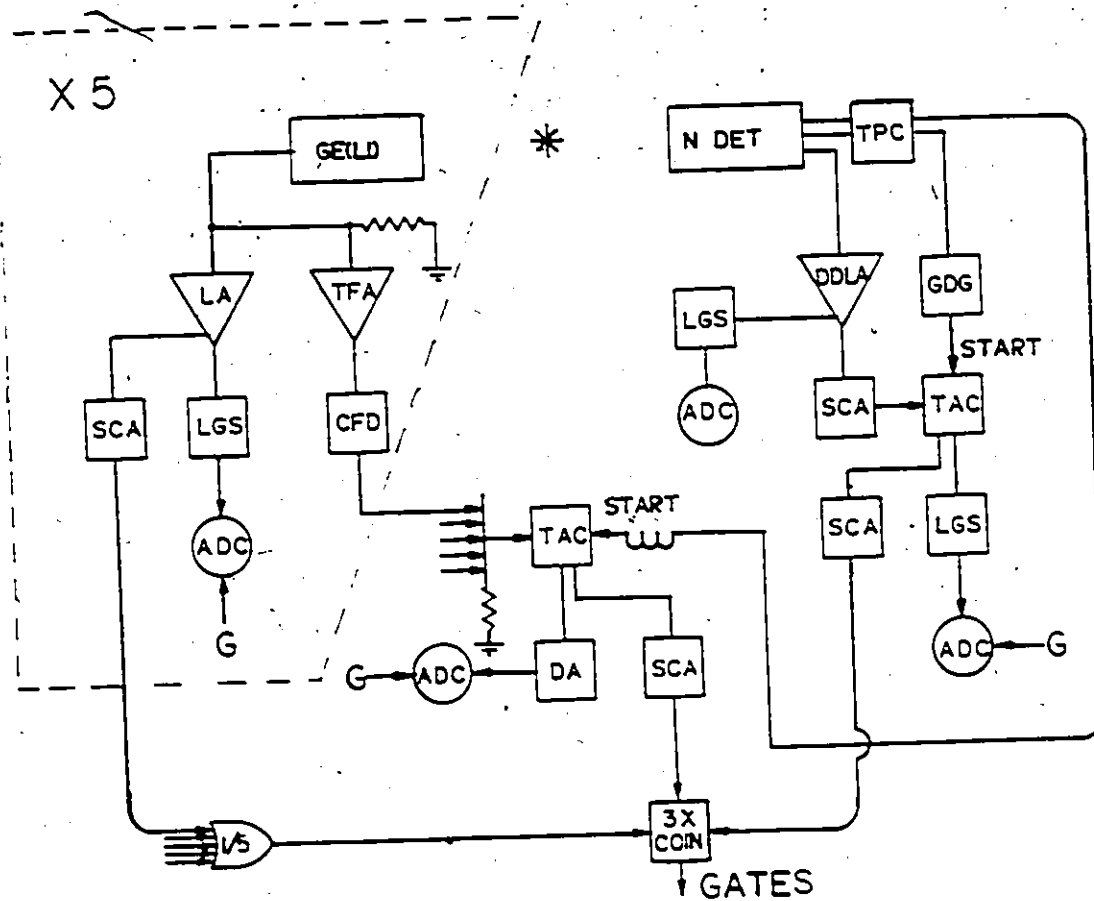


Figure 3.7 ii. Typical (5)  $n\gamma$  coincidence circuit for  $n\gamma$  angular distributions.

linear energy signals to five ADC's. Coincidences of three or more signals, at least two from Ge/Ge(Li)'s, were required before the events were address recorded by the PDP-9 (program JCWR). Data were sorted off-line by the PDP-15 (program JCWS). (In one experiment an equivalent program on the VAX was used, but preliminary on-line sorting failed to yield any new useful information, so the data were not saved for further analysis.) Windows were set on  $\gamma$  peaks in one detector and spectra collected from the  $\gamma$  coincidences in either one of or all the remaining Ge/Ge(Li)'s (all the Ge/Ge(Li) signals having been conveniently matched in gain at the onset of the experiment). Background windows had to be set separately. The collected background-window spectra were then subtracted from the collected peak-window spectra on the PDP-9 (ADCS) or PDP-15 (HANDLE). No corrections for chance events were made as the 200 nsec multiple coincidence requirement and reasonable count rates ( $< 10$  K counts/sec) ensured reasonably large true/chance ratios.

### 3.6 Angular distributions

The angular distribution  $W(\theta)$ , of  $\gamma$ -rays from the decay of a given state to another following a particle induced nuclear reaction may be described in terms of even Legendre polynomials (Yamazaki (1967), Rose and Brink (1967), Sheldon and van Patter (1966):



$$W(\theta) = \sum_{\substack{k=0 \\ \text{even}}}^{k_{\max}} A_k P_k(\cos\theta) \quad (k_{\max} = 4, \text{ usually}) \quad 3.6.1$$

The summation is over even  $k$  because of the time reversal invariance. Normally higher order terms are not necessary, though there may be occasional exceptions for  $\gamma$ -rays of multipolarity greater than two. The population of the  $m$ 'th substate of the state with spin  $J$ ,  $P_m(J)$  is equal to  $P_{-m}(J)$ .

Often  $W(\theta)$  is normalized such that  $A_0 = 1$  since only the  $A_2$  and  $A_4$  (alternately, the  $a_2 \equiv A_2/A_0$  and  $a_4 \equiv A_4/A_0$ ) coefficients are of interest. It is the  $a_k$  coefficients that contain information about multiplicities ( $L_1, L_2$ ) of the  $\gamma$ -rays, and spins and indirectly, parities ( $J_i^\pi, J_f^\pi$ ) of the levels involved (Yamazaki, etc.):

$$a_k(J_i L_1 L_2 J_f) = \rho_k(J_i) \frac{1}{1+\delta^2} \{ F_k(J_f L_1 L_1 J_i) + 2\delta F_k(J_f L_1 L_2 J_i) + \delta^2 F_k(J_f L_2 L_2 J_i) \} \quad 3.6.2$$

where  $\rho_k$  is the statistical tensor describing the population of the substates:

$$\rho_k(J) = (2J+1)^{1/2} \sum_{m=-J}^J (-)^{J-m} \langle J m J -m | k 0 \rangle P_m(J), \quad 3.6.3$$

$$F_k(J_f L_1 L_2 J_i) = (-)^{J_f - J_i - 1} [(2L_1 + 1)(2L_2 + 1)(2J_i + 1)]^{1/2} \quad 3.6.4$$

$$\times \langle L_1 \ 1 \ L_2 \ -1 | k \ 0 \rangle W(J_i J_i L_1 L_2; k J_f),$$

$\langle L_1 \ 1 \ L_2 \ -1 \ k \ 0 \rangle$  is a Clebsch Gordan coupling coefficient,  $W(J_i J_i L_1 L_2; k J_f)$  is a Racah coefficient, and  $\delta$  is the mixing ratio of the multipolarities (e.g.  $E_2/M_1$ ) as defined previously:

$$\delta \equiv \frac{\langle J_f \ 1 \ L_2 \ 1 \ J_i \rangle}{\langle J_f \ 1 \ L_1 \ 1 \ J_i \rangle} \quad 3.6.5$$

Non-zero mixing ratios are an aid in assigning relative parities. For instance, if  $\delta(1,2) \neq 0$ , then the transition must be M1/E2 as an M2 would not compete with an E1 transition, hence:  $\pi_i = \pi_f$ . Similarly, if  $\delta(2,3) \neq 0$  then the transition must be M2/E3 and  $\pi_i = -\pi_f$ . If  $\delta(1,2) = 0$  (or  $\delta(2,3) = 0$ ), then no parity assignment is possible on this basis. (The transition is most likely E1 (E2), but the possibility of a pure M1 (M2) transition cannot be ruled out entirely, even though pure M1 (M2) transitions are quite rare in the mass A=60 region (Endt (1979)). Additional information should really be supplied by independent experiments, eg. the measurement of  $\gamma$  transition lifetimes (eg. for  $E_\gamma < 1.3$  MeV and time resolution of 10 ns or better and  $l=2$  as determined by the angular distributions; the

transitions must be E2 if no lifetime is seen within error) of the  $\gamma$  polarization via a double scattering  $\gamma$  experiment, or the measurement of the electron conversion ratios using an electron spectrograph, such as an "Orange" electron magnetic spectrometer. Again, because of much stronger competing channels, the requirements of neutron coincidence would have to be imposed, resulting in very slow net counting rates indeed. An n- $\gamma$  polarization experiment has already been carried out by Smith et al. (1981) for  $^{61}\text{Zn}$ . It was felt that to repeat these measurements here would not be worthwhile. Meanwhile, n-e experiments using an Orange electron spectrometer would be prohibitively slow, because of both low overall efficiency and small conversion ratios in the A-60 mass region.

The finite size of the detector(s) must also be taken into account. The experimental angular distributions are therefore fitted to the function

$$W(\theta) = A_0 + A_2 Q_2 P_2(\cos\theta) + A_4 Q_4 P_4(\cos\theta) \quad 3.6.6$$

where  $Q_2$  and  $Q_4$  are the geometrical corrections for the detector(s), leaving  $A_2/A_0$  and  $A_4/A_0$  to be determined by a least-squares method. For this project, the solid angle corrections for Ge/Ge(Li) coaxial detector compiled by Camp and Van Lehn (1971) have been used. Where several detectors were used at fixed angles, the  $Q_2$  and  $Q_4$  values may depend

on  $\theta$ . When necessary the  $\theta$  dependence was taken into account with program LEGADJ (by adjusting the angular distribution to simulate one taken with a single detector while still maintaining the same error fluctuations) prior to analysis by programs LISA on the PDP-15, or ANGSIGX on the VAX.

After initially finding the experimental  $A_k$  values, LISA/ANGSIGX then proceeded to find the best theoretical values for varying mixing ratios and given assumptions of  $\{J_i, J_f, L_1, L_2$  and  $P(m)\}$  that reproduce the experimental coefficients. If one or more of these "assumptions" is really an unknown parameter, then it is clear that a unique assignment may not always result. Angular distribution of other decay branches may have to be considered as well. Alternatively one of the spins may have to be determined by other means. For instance, the ground state spin/parity of  $^{61}\text{Zn}$  is found by  $\beta^+$  decay studies (Hoffman et al. (1969, 1970), Dulfer et al. (1972)) to be  $3/2^-$ . As an even-even nucleus, the ground state of  $^{60}\text{Zn}$  is automatically assigned a spin/parity of  $0^+$ . It is possible, in principle, to determine spin/parity values for higher levels by working up the cascades.

The third important class of parameters to consider are the populations. In principle they could be calculated if the reaction mechanism is well known, for example by the code ALICE or other variations of the Sheldon and Strang

(1969) code MANDY. However, this "mechanism" still has to take into account the structure yet to be determined. A practical alternative is to find the populations empirically or design an experiment whereby they are restricted to known values. For (heavy ion, yp xn) reactions, it has been demonstrated (Diamond et al. (1966)) that a Gaussian distribution adequately describes the populations:

$$P_m(J) = \exp(-m^2/2\sigma^2) / \sum_{m'=-J}^J \exp(-m'^2/2\sigma^2) \quad (3.6.7)$$

Because the H.I. beam defines the quantization (z) axis, the orbital angular momentum brought into the system is only in the  $m_L = 0$  substate. If the target and projectile both have zero intrinsic spin, then the incoming projection of total angular momentum is  $m_J = 0$  only, otherwise the projections range over the possible combinations of intrinsic spin. The evaporating particles tend to carry away only small amounts of angular momentum; if several particles are boiled off, their random direction and energies (recall that a continuum of states is being sampled in the CN system for any experiments with finite beam energy resolution and target thickness) introduce cancellations finally leading to a statistical (Gaussian) distribution for the m-states.

Sawa (1973) has shown that ( $\alpha, n$ ) and ( $\alpha, p$ ) reactions in the Ni-Zn region give rise to essentially Gaussian

distributions with relatively small values for the "alignment" parameter  $\sigma$ . [Unfortunately the expression "alignment" is used to describe the distribution as well as the  $P_m/P_{-m}$  symmetry. The case for  $\sigma=0$  is said to correspond to complete alignment: i.e., only the  $m=0$  (or  $\pm 1/2$ ) state is populated.]

Recently Ekström et al. (1981) have reported that a modified Gaussian,  $\exp\{-m^x/2\sigma^x\}$  ( $1 \leq x \leq 2$ ), is better at describing the distributions because of top as well as side feeding (but at the expense of introducing another parameter; for  $\gamma$  distributions near threshold or where "Method II" geometry (q.v.) is invoked,  $\sigma$  is so small that it doesn't really matter if  $x=2$  or not).

Another way to treat top feeding is via the use of  $U_k$  coefficients. For a transition  $J'_i \rightarrow J_i$  with multipolarity  $L'_1 L'_2$ , the statistical tensor  $\rho_k(J_i)$  can be described in terms of  $\rho_k(J'_i)$  (after Yamazaki (1967)):

$$\rho_k(J_i) = U_k(J'_i L'_1 L'_2 J_i) \rho_k(J'_i) \quad 3.6.8$$

$$\text{where } U_k(J_i L_1 L_2 J_f) = \frac{1}{1+\delta} [u_k(J'_i L'_1 J_i) + \delta^2 u_k(J'_i L'_2 J_i)] \quad 3.6.9$$

$$3.6.10$$

$$\text{and } u_k(J'_i L'_1 J_i) = (-)^{J'_i + J_i - L'_1} [(2J'_i + 1)(2J_i + 1)]^{1/2} W(J'_i J'_i J_f J_i; k L'_1)$$

Generally the  $u_k$  coefficients are close to one in value, except for jackknife cases ( $l < |J_f - J_i|$ ) and/or where  $J_i$  is small.

When the amounts of top feeding, side feeding, and spins of the preceding states are known, the populations for the level of interest may be calculated by weighting the  $U_k$  coefficients with the feeding  $\gamma$ -intensities vs. the side component. This has been shown to be very successful by Jonesou et al. (1981). One immediate benefit is that the number of free parameters needed to describe the populations may be reduced to one (the Gaussian width parameter  $\sigma$  for side feeding), or even none (for "Method II" geometry). Unfortunately, a major drawback is that the spins of the feeding states are not usually known beforehand so some degree of model dependence is still inescapable. As a convenience, an attenuation coefficient is defined as (Yamazaki)

$$\alpha_k(J_i) \equiv \rho_k(J_i)/B_k(J_i) \quad 3.6.11$$

where  $B_k(J)$  is the statistical tensor for complete alignment ( $\sigma = 0 \Rightarrow \alpha_k = 1$ ):

## 3.6.12

$$B_k(J) = \begin{cases} (2J+1)^{1/2} (-)^J \langle JOJO|kO \rangle & \text{for integral spin} \\ (2J+1)^{1/2} (-)^{J-1/2} \langle J \ 1/2 \ J \ 1/2|kO \rangle & \text{for half} \\ & \text{integral spin} \end{cases}$$

so that the  $A_k$  coefficients may be expressed in terms of their maximum values times the attenuation coefficients:

$$A_k(J_i L_1 L_2 J_f) = \alpha_k(J_i) A_k^{\max}(J_i L_1 L_2 J_f) \quad 3.6.13$$

For top feeding,

$$\alpha_k(J_f) = U_k(J_i L_1 L_2 J_f) \frac{B_k(J_i)}{B_k(J_f)} \alpha_k(J_i) \quad 3.6.14$$

$$\lesssim \alpha_k(J_i) \quad (\text{usually}).$$

A more favourable situation regarding the populations may be found in the so-called "Method II" of Litherland and Ferguson (1963). If a single proton or neutron is emitted following a nuclear reaction between a spin zero target and spin zero projectile (as for the  $^{58}\text{Ni}(\alpha, n\gamma)^{61}\text{Zn}$  experiment), and the emitted particle is detected at  $0^\circ$  or  $-180^\circ$  in coincidence with the  $\gamma$ -ray(s), then only the  $m = \pm 1/2$  states are populated. Where top feeding is applicable, de-alignment may still occur, but this is normally small since most  $U_k$



coefficients are close to one. (One obvious advantage of an  $(\alpha, \text{p}\gamma)$  experiment over an  $(\alpha, \text{n}\gamma)$  experiment is the level selectivity available due to the energy resolution of the charged particle detector.)

Errors for the multipole mixing ratios ( $\delta$ ) were estimated according to the method of James et al. (1979) by determining the  $\delta$  values corresponding to the  $E_{32\%}$  confidence level above R, the  $\chi_{\text{min}}^2$  value at S:

$$E_{32\%} = R/n F_{32\%}(1, n) \text{ or } 1, \text{ whichever is larger} \quad 3.6.15$$

where  $n$  is the number of degrees of freedom and

$$F_{32\%}(1, n=1 \text{ to } 4) = 3.69, 1.84, 1.50, 1.38 \quad 3.6.16$$

In the  $(\alpha, \text{n}\gamma)$  coincidence experiment, it was advantageous to use several  $\gamma$  detectors at different angles in order to offset the slow net counting rates and any changes in the initial conditions (e.g. drifting in the neutron detector electronics, wandering of beam spot, etc.). Normalization of the  $\gamma$  detectors relative to each other was readily accomplished by measuring singles  $\gamma$ -rays following  $\beta$  activity with the beam off (or even on: for instance,  $^{61}\text{Ni}$   $\gamma$ 's can only be produced by  $\beta^+$  decay of  $^{61}\text{Cu}$  following irradiation of  $^{58}\text{Ni}$  with  $\alpha$ 's). Some strict precautions had to be taken. No adjustments could be made to the individual  $\gamma$

timing/energy response during the experiment (the neutron detector is somewhat less critical as all  $\gamma$  signals are affected the same way). It was necessary that normalization measurements be carried out several times over the duration of the experiment. Address recording of all the data allowed any corrections due to drifting, background, etc. to be applied during playback. Choice of  $\gamma$  detectors turned out to be critical as well, partly for their low energy response and partly because the  $\beta$ - $\gamma$  normalizations are not sensitive to  $Q_2$  and  $Q_4$ . It was found that  $\gamma$  detectors of similar volume, construction, and, importantly, resolution gave more reliable results. (When necessary, the distributions could be easily corrected for  $\theta$  dependence of  $Q_2$ ,  $Q_4$ ; maintaining consistency in evaluating areas of peaks for detectors of widely varying resolution and/or level of neutron damage was another matter!)

Where resolution and intensity permitted, singles angular distributions with a single movable counter were also made, with normalization provided by a second fixed angle monitor counter and integrated beam current.

### 3.7 Delayed Decay Studies

#### 3.7.1 Electronic timing

Address recording of the coincidence events afforded the opportunity of examining the data from different perspectives. Lifetimes of  $\gamma$  ray emission of the order of a

few nsec or greater, could be measured by revising the roles of the window and collected spectra. A relevant example is the placing of windows on peaks and backgrounds of the  $\gamma$  events of interest, correcting for intruding  $\bar{\gamma}$  events by setting appropriate windows on the pulse shape analysis spectra, and collecting the time (TAC) spectra. Alternatively the timing for the  $\gamma$ - $\gamma$  recorded events could be similarly examined.

It should be noted that two precautions are in order. Firstly, the timing characteristics of the detectors must be well understood in the energy region of interest -- specifically the jitter and walk in the low energy response. (One immediate solution is to use a smaller  $\gamma$  detector, such as the 15 cc detector, which has better timing characteristics for low energy  $\gamma$ -rays than say, the 26% detector. This is important, particularly for the neutron deficient Ni-Zn region where only the very low lying states are expected to exhibit any appreciable lifetimes; decays from the positive parity states in the odd isotopes are expected to be too fast (under 1 nsec) to measure with these electronics and detectors). Secondly, one has to be certain that any  $\gamma$  top feeding is truly "prompt" or else correct for any such contributions.

### 3.7.2 Beam-off activity

A delay decay method that has already been alluded to is, of course, the  $\gamma$  emission following  $\beta$  ( $\beta^+$ ,  $\beta^-$ , electron capture) decay. The decay of  $^{59}\text{Zn}$ , produced via the ( $^3\text{He}, 2n$ ) reaction, has been studied by Honaku et al. (1981) and Arai et al. (1981) by measuring p,  $\beta$ , and  $\gamma$  activities following physical transfer (and separation) of the reaction products to a low background counting room. An attempt was made in this project to study  $^{59}\text{Zn}$  decays in situ, with the aim of determining if there is sufficient relative activity to inspire further inbeam investigations of the actual levels of  $^{59}\text{Zn}$ . Similarly, inspired by the "reasonable" production of  $^{61}\text{Zn}$  from the ( $^{24}\text{Mg}, 2pn$ ) reaction on  $^{40}\text{Ca}$  it was hoped that the decay of  $^{61}\text{Ga}$  to  $^{61}\text{Zn}$  might also be observed out of beam, prompting further inbeam analysis of  $^{61}\text{Ga}$  itself.

A (slow) pulsed beam experiment was devised to investigate the above decays, employing a solenoid activated mechanical beam chopper, Ge/Ge(Li) detector and a Tektronix oscilloscope. Beam energies ranged from 15 to 30 MeV for  $^3\text{He}$  and 60 to 85 MeV for  $^{24}\text{Mg}$ . Beam on times were typically of one second duration, the anticipated lifetimes being of the order of a few tenths of a second. Collection times between beam pulses ranged from 1 to 30 sec. The longer times were to allow the intermediate-lived competing activi-

ties to die down; buildup of the longer-lived activities remained unavoidable.

The ramp generator from the oscilloscope provided beam-on signals for the chopper and timing information to an ADC. Energy signals from the  $\gamma$  detector fed the other ADC. Both ADC's were gated by the "logical AND" of the  $\gamma$  detector and beam-off requirement. Events were both sorted on-line and address recorded by program ERW on the PDP-9. After data accumulation, the overall "background" events, represented by a window on the tail of the ramp, had merely to be subtracted from the remaining regions to provide spectra representing several "time-slices" of the beam off activities.

Unfortunately the  $\gamma$  events of interest (491, 914 keV in  $^{59}\text{Cu}$ ; 88, 123, 418, 756 keV in  $^{61}\text{Zn}$ ) were so overwhelmed by the competing longer lived events that they remained totally obscured, even after subtraction of the background windows. Further in-beam analysis of  $^{59}\text{Zn}$  or  $^{61}\text{Ga}$ , using relatively simple  $\gamma$  spectroscopic techniques, remains unfeasible.

### 3.7.3 Doppler shift attenuation method (DSAM)

At the other end of the timing scale, heavy ion beams can also facilitate the measurement of nuclear lifetimes. Because the heavy ion projectiles bring a reasonably large quantity of linear momentum into the compound nuclear

systems, the residual nuclei can recoil with considerable velocities, typically up to a few percent of the speed of light for reactions of interest. These velocities are often sufficient such that  $\gamma$ -rays emitted before the recoiling nuclei come to rest, can be measurably doppler shifted in energy. Measurements of the doppler shifts, which may be manifest as doppler broadening of the lines, or other line shape changes or actual shifts in the centroids (which change with angle of  $\gamma$ -rays with respect to the recoil axis), and a knowledge of the recoiling particles' stopping processes may, in principle, be used to calculate the  $\gamma$  lifetimes.

The details of such analyses may be readily found in the literature, e.g. Hoffman and Patter (1973), Morand and Chans (1981). Specifically, these references are typically concerned with:

- lifetimes between  $\sim 0.02$  ps and 5 ps,
- $50 < A < 80$ ,
- target thickness  $\sim \text{mg/cm}^2$ ,
- $v_{\text{recoil}}/c \sim 1\%$ , number of evaporated particles  $\leq 3$ ,
- number of top feeding contributions exhibiting appreciable lifetimes  $\leq 3$ , and
- for either unrestricted recoil direction (e.g.  $\gamma$  singles) or restricted directions (e.g. detection of the evaporated particle at  $0^\circ$  or  $180^\circ$  in coincidence with the  $\gamma$ -rays restricts the recoiling residual nucleus to move on this

axis; the  $\gamma$ -rays themselves impart insufficient momentum to appreciably alter the residual's direction).

For values outside these ranges, beam energies and targets may have to be selected with some care: using beam energies just above reaction threshold to limit the recoil's directions or high energies to impart more linear momentum, thin targets with backings to slow the recoils down at predetermined rates, or even no backings to allow the recoils to decay unimpeded in vacuum. (One must bear in mind that compromises between size of shifts, cross sections, resolution, backgrounds, etc. must often be struck.)

Further details will not be provided here, primarily for two reasons: a DSAM program is not currently available on-line at the McMaster facilities at time of writing and more importantly, the shifts observed for the  $\gamma$ -rays of  $^{60,61}\text{Zn}$  either lie outside the DSAM limits for the targets and projectiles used here or are obscured by peak shape responses of the detectors.

## CHAPTER 4

### $^{61}\text{Zn}$ : Results and Discussion

#### 4.1 Results and general discussion

When work on this project began in 1978, the only information known about the structure of  $^{61}\text{Zn}$  was the ground state spin and lifetime via  $\beta$  decay studies (Hoffmann et al. (1970,1969), Dulfer (1972)), some  $\gamma$ -rays belonging to  $^{61}\text{Zn}$  via  $(\alpha, n\gamma)$  (Sarantites et al. (1973)), and a partial level scheme via a  $(^6\text{Li}, t)$  experiment (Woods et al. (1978)). Since then, additional work has been published on the  $(^{12}\text{C}, ^9\text{Be})$  reaction of Weber et al. (1979) and, more importantly (to this thesis, at least!) similar  $(\alpha, n\gamma)$  studies by Smith et al. (1982).

In the work of Sarantites et al., the most intense  $\gamma$ -ray belonging to  $^{61}\text{Zn}$  was found to be the 123 keV line. After a preliminary  $(\alpha, n)$  yield curve measurement of this line and on the basis of competing  $(\alpha, 2n)$  and  $(\alpha, pn)$  exit channels, it was decided to study  $^{61}\text{Zn}$  in greater detail at 20 MeV  $\alpha$  bombarding energy. Singles- $\gamma$ ,  $\gamma$ - $\gamma$  and  $n$ - $\gamma$  measurements were made. Figures 4.1, 4.2, 4.3 show the  $\gamma$ - $\gamma$  projection,  $n$ - $\gamma$  coincidence and  $\gamma$  singles spectra with  $\gamma$  counters at  $90^\circ$  to minimize any doppler shifts. Many of the  $n\gamma$  lines observed by Sarantites et al. may also be seen in the  $n\gamma$



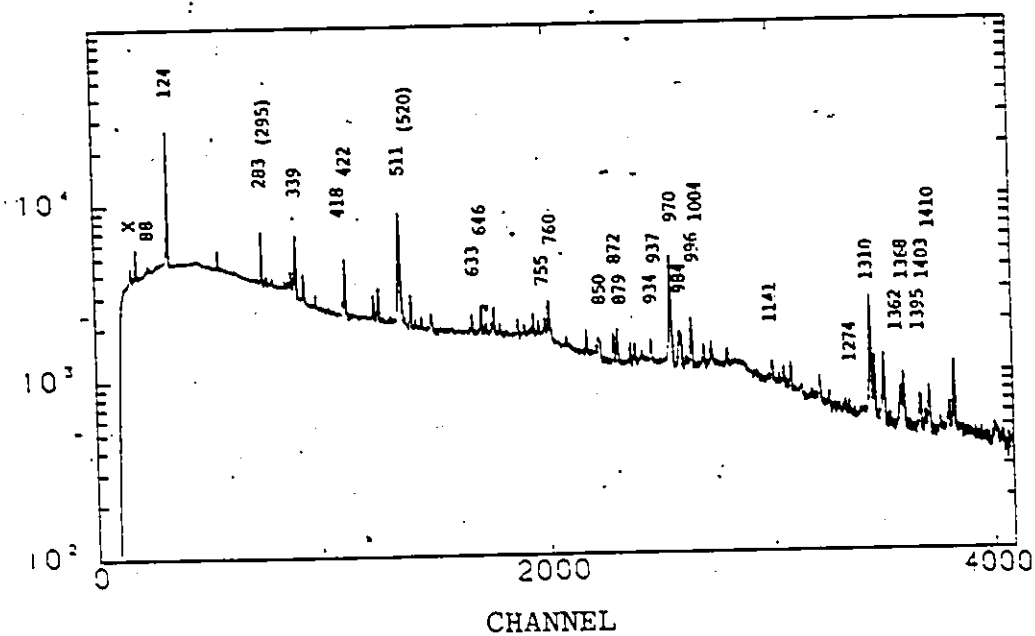


Figure 4.1.  $^{58}\text{Ni}(\alpha, n\gamma)^{61}\text{Zn}$   $\gamma$ - $\gamma$  projections at  $E_\alpha = 20$  MeV.

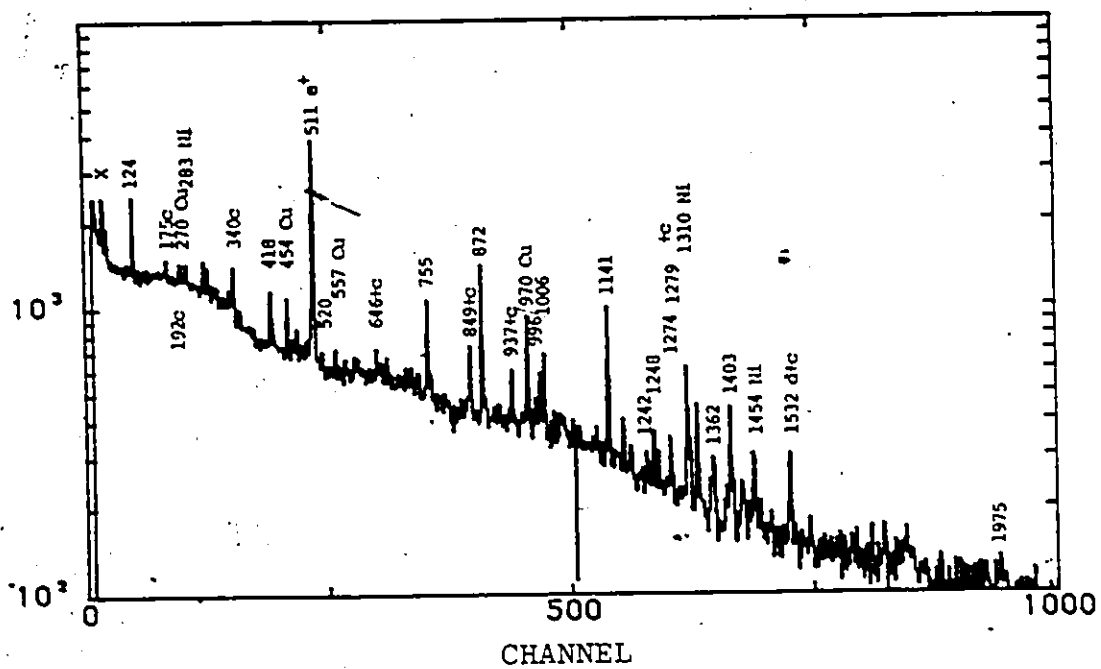


Figure 4.2.  $n\gamma$  spectrum ( $90^\circ$ , in coincidence with neutrons at  $0^\circ$ ) at  $E_\alpha = 20$  MeV.

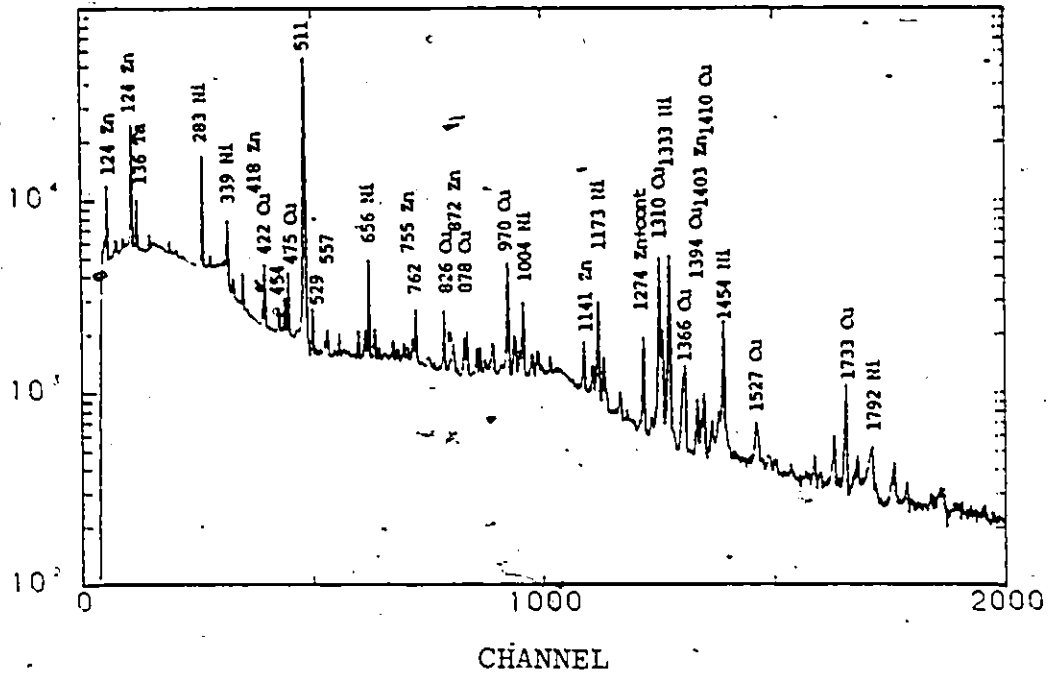


Figure 4.3.  $\gamma$ -singles spectrum at  $E_{\alpha} = 20$  MeV.

spectrum of Fig. 4.2; however, several are not. Some, like the 175, 192, 197 keV lines may be attributed to contaminant reactions on  $^{16}\text{O}$  and  $^{19}\text{F}$ ; others, like the 88 keV are not readily seen because the dynamic range of the neutron detector appears to have been set too low and/or the constant fraction discriminator for the  $\gamma$  electronics was set too high, producing a low energy rolloff -- even the 123 keV line, which is very intense in the singles and  $\gamma$ - $\gamma$  spectra, is severely attenuated. Also appearing in the  $n\gamma$  spectrum are many lines intruding from non neutron exit channels, such as the stronger decay lines of  $^{61}\text{Zn}$  to  $^{61}\text{Cu}$  to  $^{61}\text{Ni}$  (475; 283, 373, 656, 1186 keV, etc.) positron annihilation (511 keV),  $^{61}\text{Cu}$  and  $^{57}\text{Ni}$  in beam lines, and other contaminants, notably  $^{59}\text{Ni}$  via  $^{56}\text{Fe}(\alpha, n)$  (339 keV line, among others), indicating that the stainless steel target chamber walls were also irradiated.

An  $n$ - $\gamma$  angular distribution was measured using 4 Ge(Li) detectors at  $90^\circ$ ,  $60^\circ$ ,  $135^\circ$  and  $150^\circ$  and a neutron detector at  $0^\circ$ , all with respect to the beam axis. The detectors were normalized individually and relative to each other using the beam off decay lines of  $^{61}\text{Cu}$  +  $^{61}\text{Ni}$ . A typical  $\gamma$  spectrum following  $\beta$  decay is shown in Fig. 4.4; a normalization correction curve between two detectors is shown in Fig. 4.5, and a typical inverse efficiency correction for a single detector is shown in 4.6. (The

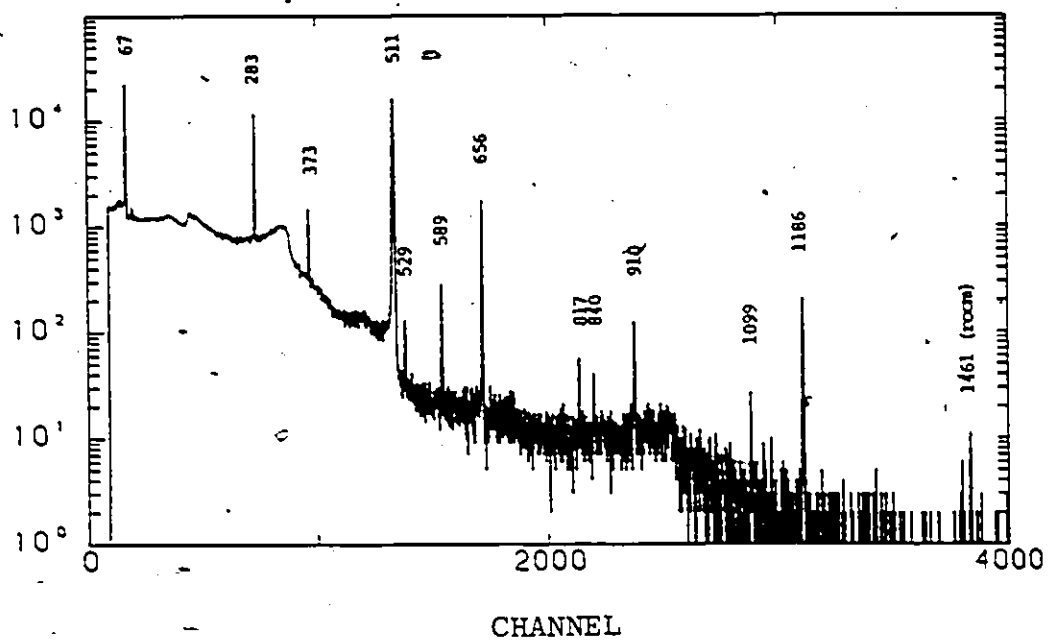


Figure 4.4 Typical beam off  $\gamma$  spectrum used in normalisations ( $^{61}\text{Cu}$  &  $^{61}\text{Ni}$ ).

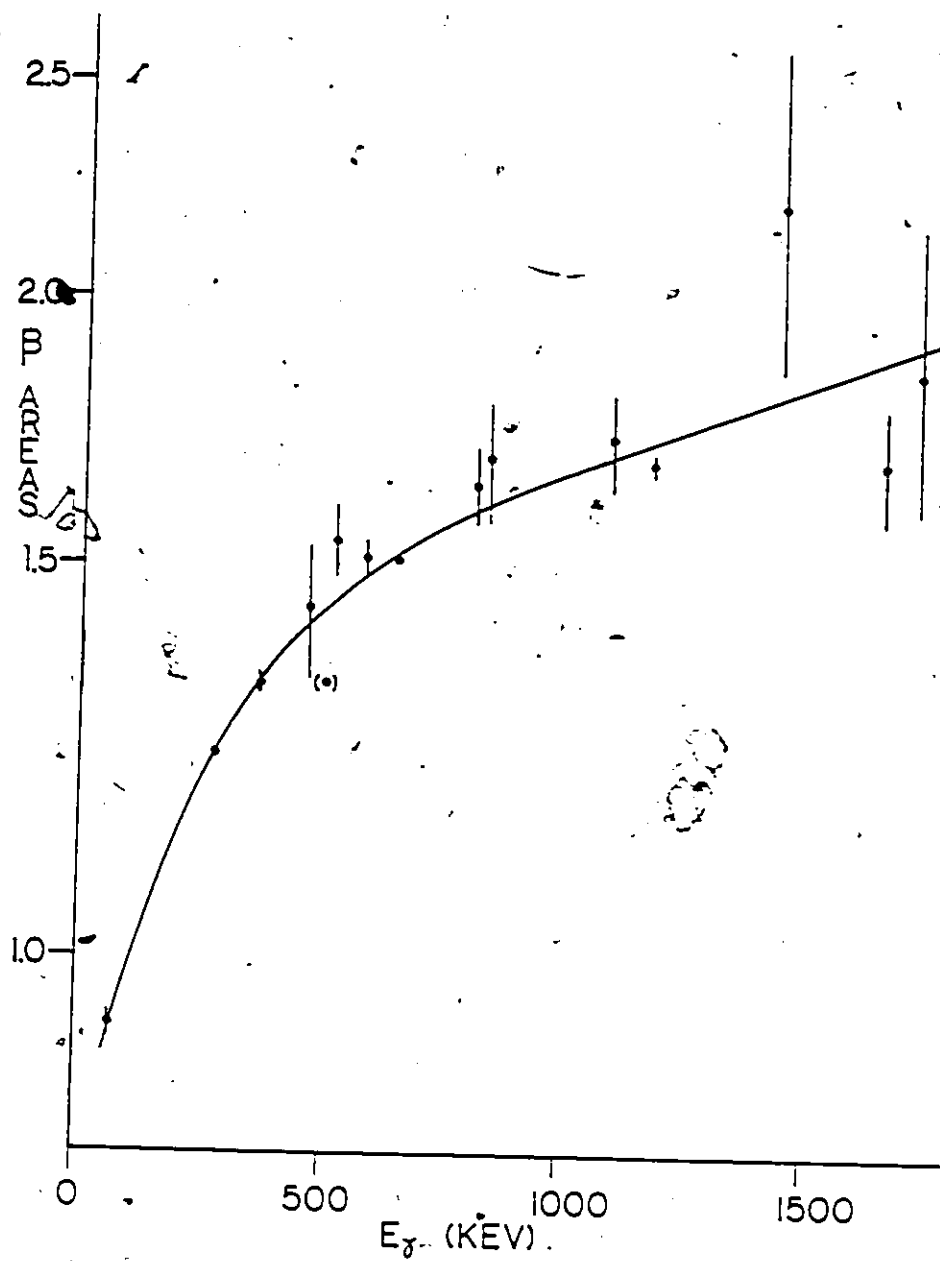


Figure 4.5. Typical inverse normalisation correction curve between two Ge(Li) detectors.

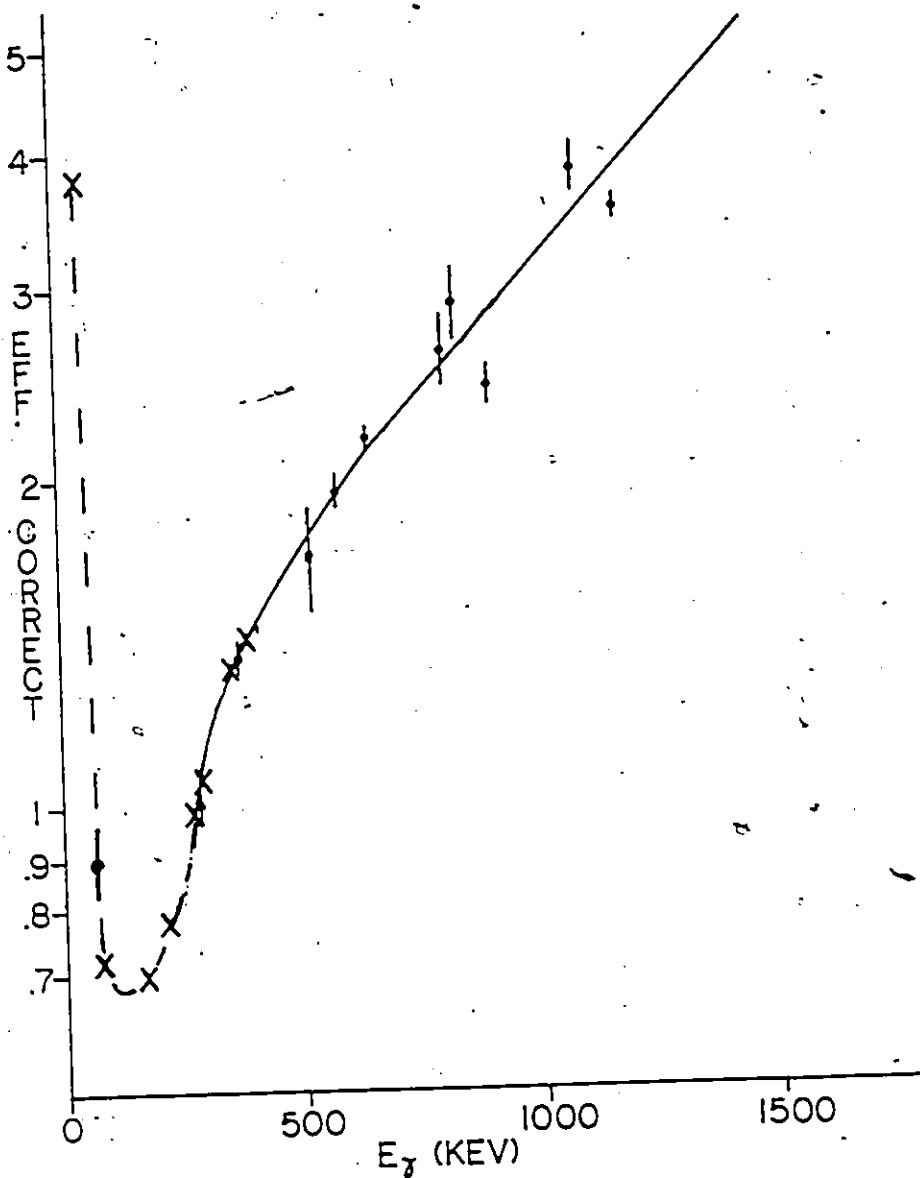


Figure 4.6. Typical inverse normalisation correction curve for a Ge(Li) or Ge(int) detector. The non-smooth response at low energy is due to dead layers in front and on the surface of the detector. (Dots are  $^{61}\text{Cu}$  decays; crosses are  $^{133}\text{Ba}$  (commercial calibration  $\gamma$  source) decays.)

latter also includes data from a run using  $^{133}\text{Ba}$  sources in addition to target decays. Commercial sources could not be used for normalization for the 20-MeV runs because they would not fit inside the target chamber at the target location.) Generally these  $n\gamma$  spectra are somewhat cleaner than the previous ones, but they still suffer from some  $n\gamma$  contaminations and intrusion of  $\bar{n}\gamma$  lines. (These data were collected in the gated singles mode only, so fine adjustments to the pulse shape analysis could not be made afterwards to correct for drifts.) Tables 4.1 and 4.4 summarize the energies and intensities of the  $\gamma$ -rays belonging to  $^{61}\text{Zn}$  seen in the  $(\alpha, n\gamma)$  work.

For the  $\gamma$ - $\gamma$  coincidence experiment at  $E_\alpha = 20$  MeV, 7 magnetic tapes of data were collected, each containing  $\sim 1.4 \times 10^6$  three parameter ( $E_{\gamma 1}$ ,  $E_{\gamma 2}$ ; TAC) events. Windows generally were set on all peaks observed in the projection spectra; specifically, the windows of interest were set on those  $\gamma$ -rays definitely belonging to  $^{61}\text{Zn}$ . Figures 4.7 to 4.9 show the collected spectra for the 123, 756 and 873 keV windows. Table 4.2 summarizes the peaks seen in  $^{61}\text{Zn}$  gates.

With the aid of these coincidence data, energy sums and intensities, a preliminary level scheme was established. Some spin and parity assignments were made based upon the analysis of the angular distributions, branchings, and intensities.



Table 4.1

<sup>61</sup>Zn γ energies in the (α,nv) reaction

E <sub>γ</sub> (keV)	Present work			
	E <sub>α</sub> = 15 MeV	E <sub>α</sub> = 20 MeV	Smith et al. (E <sub>α</sub> = 15 MeV)	Sarantites et al. (E <sub>α</sub> = 15 MeV)
88	x	x	x	
124	x	x	x	x
205	x	x	x	x
330	x		x	
337	x		x	
418	x	x	x	x
520	x	x	x	x
578	x		x	
606	x	x	x	x
631	x		x	
646	x		x	
755	x	x	x	x
850	x		x	
872	x	x	x	x
937	x	x	x	x
938	x	x	x	x
942	x	x	x	
963	x		x	
986	x	x	x	x
1006	x		x	
1007	x	x	x	
1141	x	x	x	x
1237	x	x	x	
1241	x		x	
1248	x	x	x	x
1274	x	x	x	x
1279	x		x	
1361	x		x	
1402	x	x		
1404	x	x	x	x
1533	x		x	
1536	x	(x)		
1975	x	(x)		
175	o	o	o	x
192	o	o( <sup>16</sup> O+α)	o	x
197	o	o	o	x

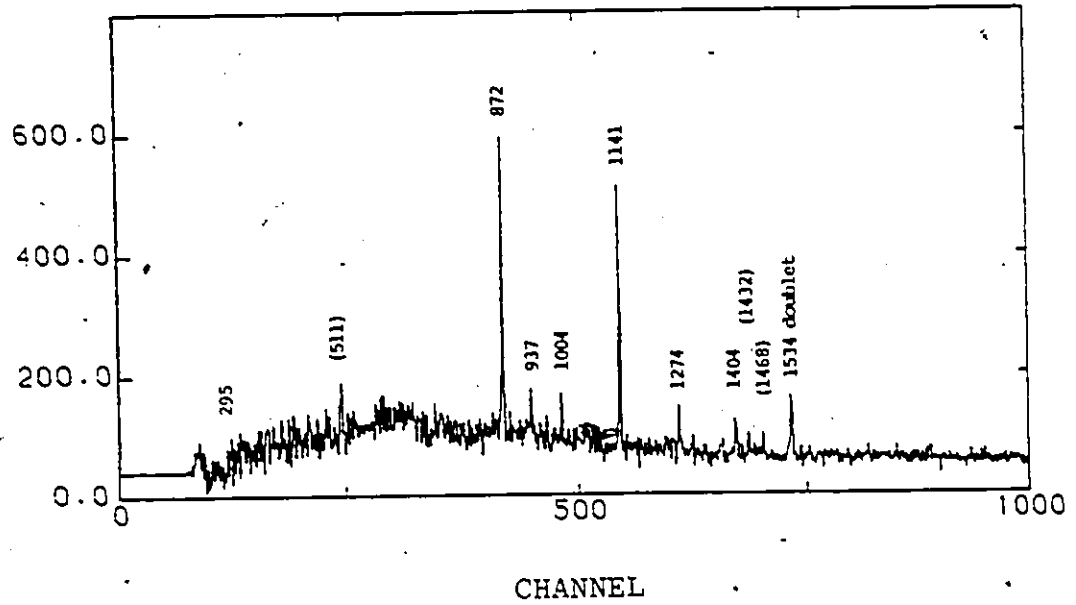


Figure 4.7. 124 keV coincidence gate spectrum at 20 MeV.

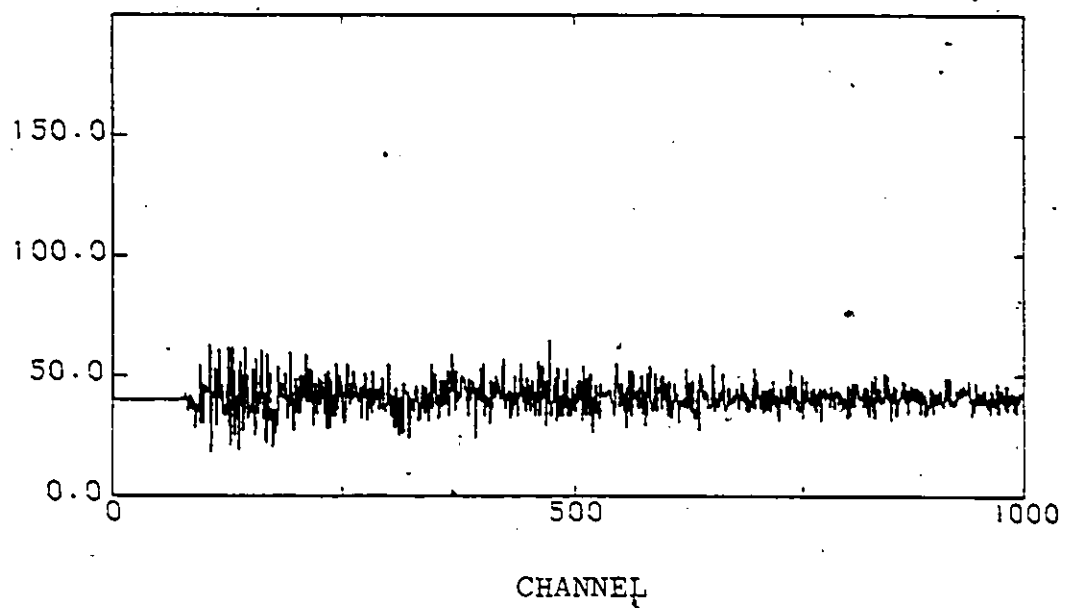


Figure 4.8. 755 keV coincidence gate spectrum at 20 MeV.

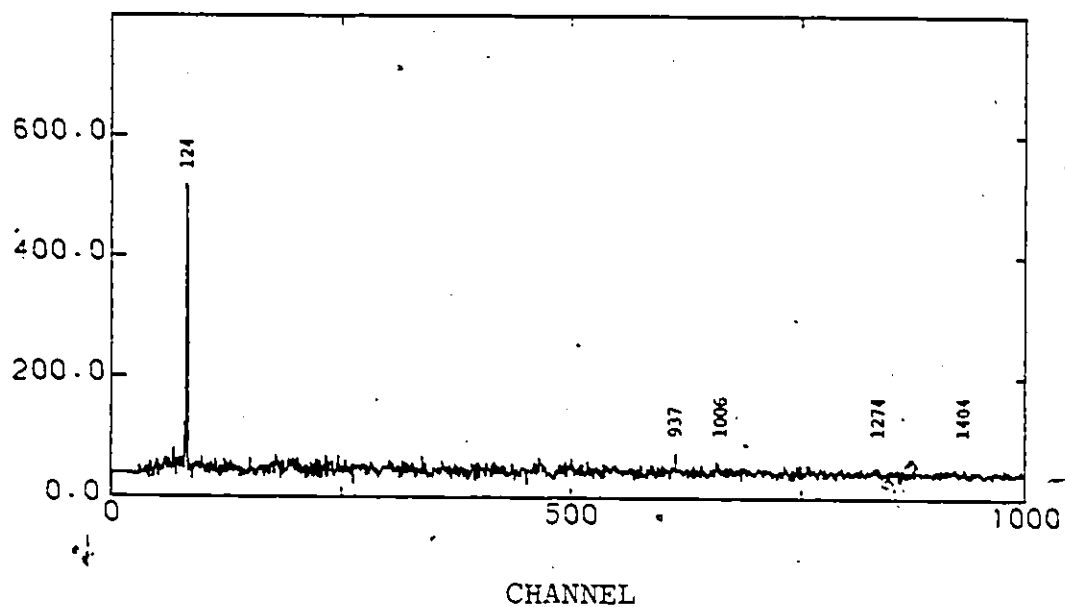


Figure 4.9. 872 keV coincidence gate spectrum at 20 MeV.  
(The spectrum shown is for a small detector with low efficiency at  $E_{\gamma} \sim 1$  MeV; the complimentary spectrum shows the high energy peaks with greater prominence, but at the expense of the 124 keV peak.)

Table 4.2

Contents of  $^{61}\text{Zn}$  coincidence gates at  $E_{\alpha} = 20 \text{ MeV}$ 

gate (keV)	Contents
88	--
124	873 937 1006 1141 1274 1279 1403 (1434) (1467) 1531 1534 (1946)
295	--
339	contaminated
418	--
520	(295)
578	--
608	--
646	contaminated
756	(646)
873	123 937 1274 1404
937	123 873 + contaminated
996	1404 + contaminated
1005	123 + contaminated
1141	123 (1006)
1247	1141
1274	123 873
1403	123 873
1531	123 1141
1974	--

There still remained several problems. The normalization measurements did not provide sufficient data points at the critical (see below) low energy end of the spectra. Departures from the smoothly varying response were due to absorber and dead layers in front of the detectors and electronic cutoffs especially from the fast timing electronics. Since the 88 and 123 keV lines form the basis for determining the spins of higher levels, their spin and parity assignments should be made on a firmer foundation than just the "weak" arguments of shell model predictions, systematics of the odd-Zn isotopes, and  $^{59}\text{Ni}$  (2 protons removed) structure for the first three closely lying states with spins/parities of  $1/2^-$ ,  $3/2^-$ ,  $5/2^-$ : since the ground state is known to have spin  $3/2^-$ , this leaves  $1/2^-$  and  $5/2^-$  for the 88 and 123 keV levels; the 123 keV line is seen strongly both in  $n\gamma$  and  $\gamma\gamma$  spectra whereas the 88 keV is not, suggesting that the spin of the 123 keV level is higher because the higher spin states would prefer to decay to this level and spin rather than to a level of similar energy and lower spin. (Recall that the Weisskopf transition rate estimates are proportional to factors and powers of multipolarity- $l$  for the same transition energy.) The most severe problem remained the intrusion of  $n\text{-}\gamma$  contamination and  $\bar{n}\text{-}\gamma$  lines affecting both identification and the angular distributions (by contamination and/or dealignment of the  $n\text{-}\gamma$  distributions by  $\bar{n}\text{-}\gamma$  correlations).

The solutions to these difficulties were found by repeating the experiments at 15 MeV  $\alpha$  bombarding energy (well below where  $(\alpha, pn)^{60}\text{Cu}$  makes any appreciable contribution) and with a physically larger, tantalum (lined) target chamber. Both the  $(n)\text{-}\gamma\text{-}\gamma$  (16 magnetic tapes worth) and  $n\text{-}\gamma$  angular distribution measurements (6 angles) were repeated at this bombarding energy. A projection spectrum at 15 MeV is shown in Figure 4.10. Gates on the 123, 756 and 873 keV lines are shown in Figures 4.11 to 4.13. The contents of the gates are summarized in Table 4.3. For the  $n\text{-}\gamma$  distribution, both  $n\text{-}\gamma$  and  $\bar{n}\text{-}\gamma$  spectra for target and beam dump only (tantalum) were taken, again in gated singles mode. Figure 4.14 illustrates the method used in attempting to correct for intruding  $\bar{n}\text{-}\gamma$  lines in the  $n\text{-}\gamma$  spectra: Figure 4.14a represents the original (neutron gated)  $n\gamma$  taken at  $90^\circ$  with the 26% detector; 4.14b represents  $\bar{n}\gamma$  spectrum; 4.14c is the  $n\gamma$  spectrum corrected for background  $n\gamma$  events by subtracting the  $n\gamma$  background spectrum normalized to known  $n\gamma$  contaminations appearing in the original, and 4.14d is the final  $n\gamma$  spectrum corrected also for  $\bar{n}\gamma$  events. All channels have an extra 500 counts to facilitate comparisons. It is clear that some  $\bar{n}\gamma$  peaks are severely overcompensated (i.e. appear negative) in the "final" spectrum because of energy dependence in the pulse shape analysis gating. A very "clean"  $\bar{n}\text{-}\gamma$  spectrum was taken using the 11% detector, a gold lined plastic chamber, gold

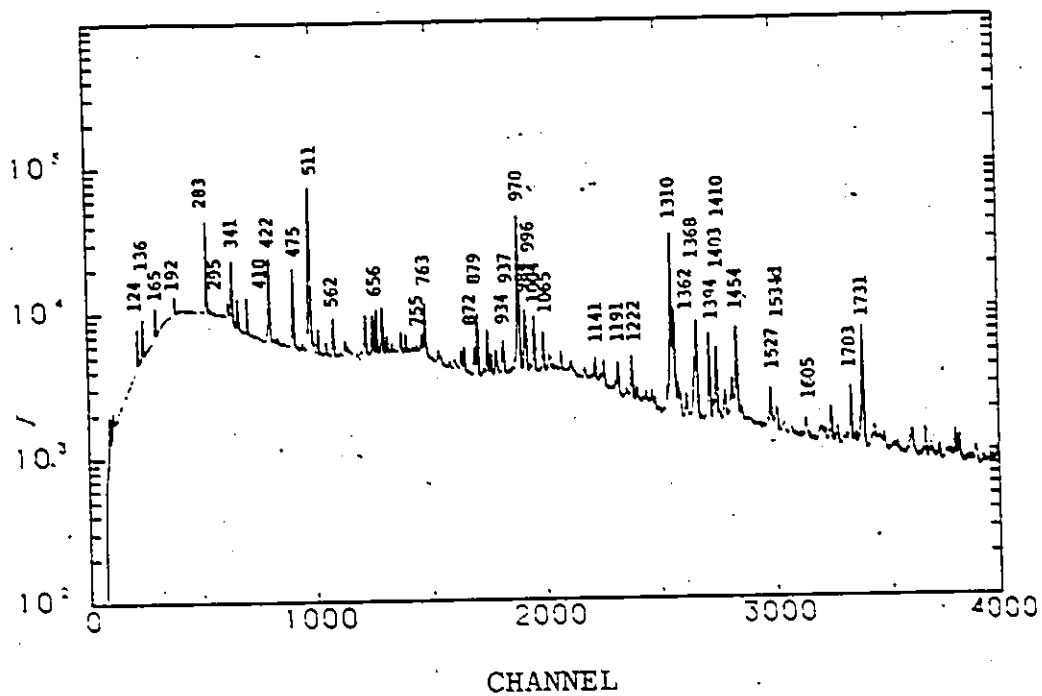


Figure 4.10.  $^{58}\text{Ni}(\alpha, n\gamma)^{61}\text{Zn}$  at  $E_\alpha = 15$  MeV :  $\gamma$ - $\gamma$  projections.



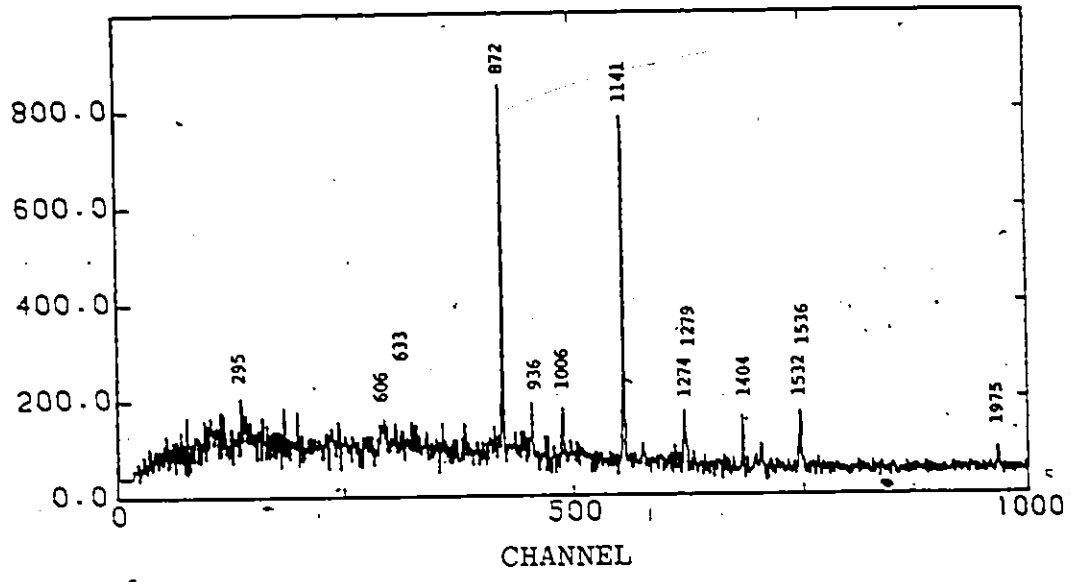


Figure 4.11. 124 KeV coincidence gate spectrum at 15 MeV.

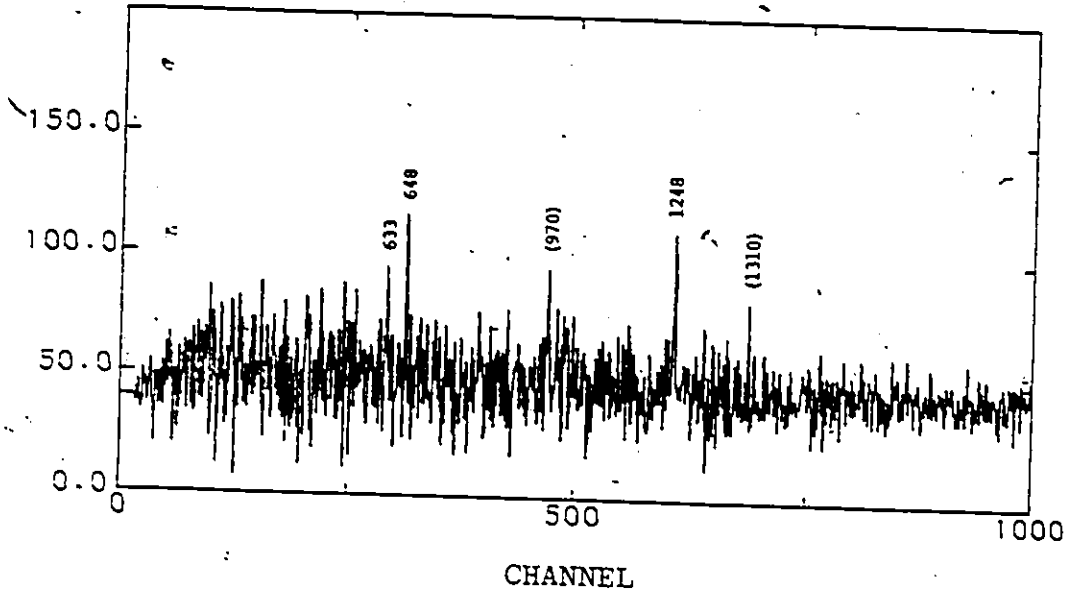


Figure 4.12. 755 keV coincidence gate spectrum at 15 MeV.

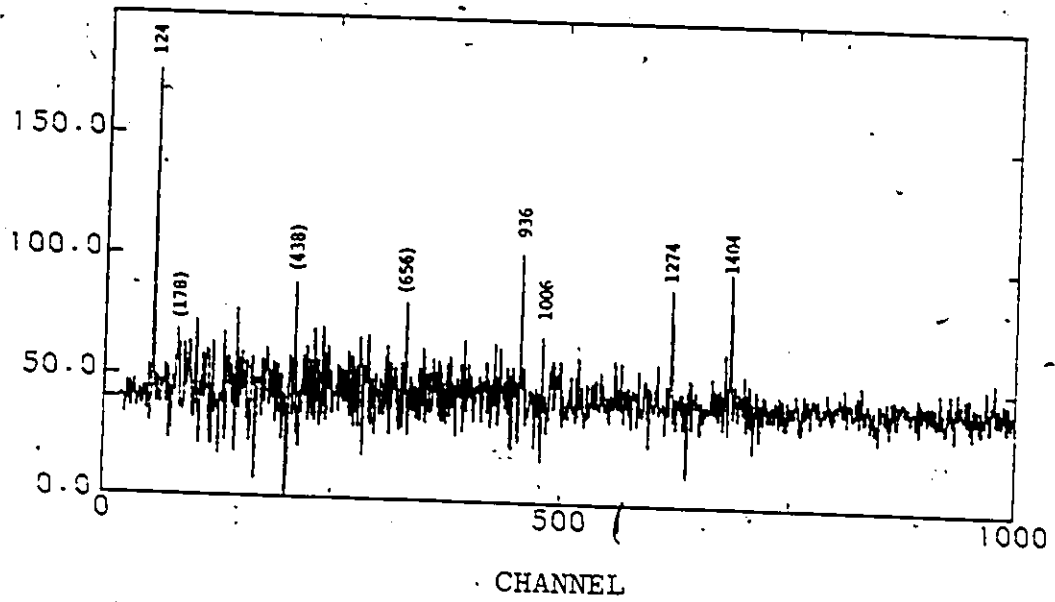


Figure 4.13. 872 keV coincidence gate spectrum at 15 MeV.

Table 4.3

Contents of  $^{61}\text{Zn}$  coincidence gates at  $E_{\alpha} = 15 \text{ MeV}$ 

gate (keV)	Contents
88	--
124	295 3897 (632) 873 937 1005 1141 1274 1279 1404 14447 1974 <1534>
295	123 + contaminated
338	contaminated
418	520 578 (944)
520	418
578	418
606	--
646	756 + contaminated
756	(606) 646 1247
873	123 (4377) 936 (1005) 1274 1404
937	873 1404 + contaminated
996	1404 + contaminated
1005	contaminated
1141	123 (1005) 1531
1247	756
1274	123 873
1403	123 873 936 996 13037
1531	123 1141
1974	123

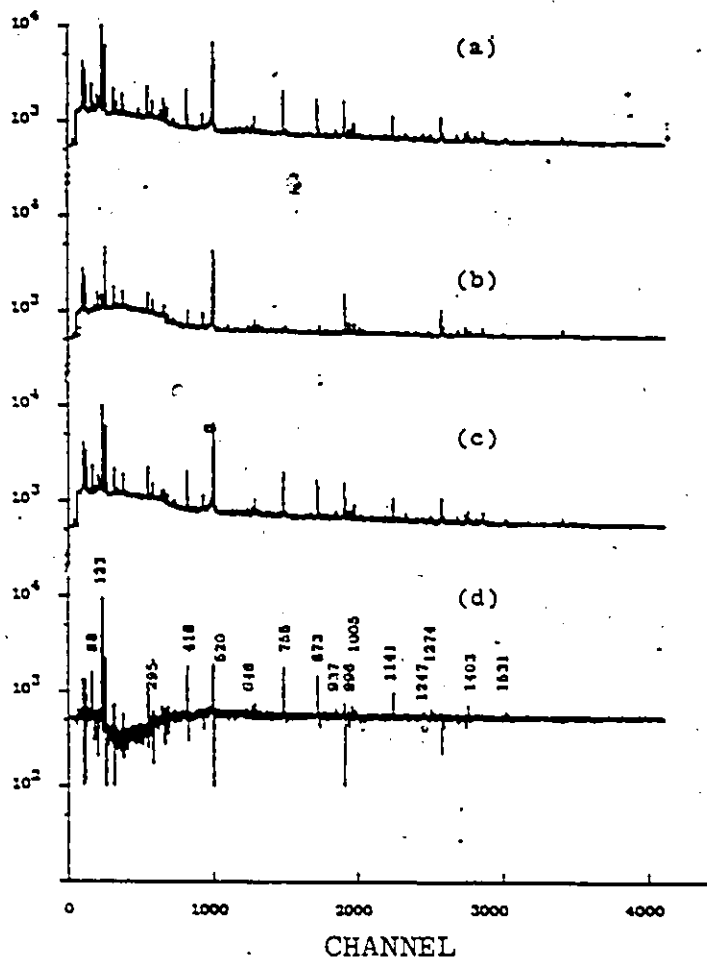


Figure 4.14. Illustration of method for crude compensation of  $\bar{n}\gamma$  events in  $n\gamma$  spectra:

- a) Initial  $^{61}\text{Zn}$   $n\gamma$  spectrum + 500 counts/channel.
- b) Separate  $\bar{n}\gamma$  (i.e.  $\gamma$  events in both neutron and  $\gamma$  detectors) + 500 counts/channel.
- c) Same as (a) but with subtraction of background  $n\gamma$  events.
- d) Same as (c) but also with subtraction of  $\bar{n}\gamma$  events of (b).

beam dump, (gold being "cleaner" than tantalum from the point of view of both reaction induced activity and chemical inertness) and address recording of  $E\gamma$ , nPHA, nPSA,  $\bar{n}\text{-}\gamma$  TAC events for careful offline sorting of the n- $\gamma$  energy and timing events. The n- $\gamma$  spectrum thus obtained is shown in Figure 4.15; Figure 4.16 shows the n- $\gamma$  TAC spectrum for the 1141 keV window. Only the 88 and 123 keV lines showed any signs of lifetimes greater than a few nsec but this could be attributed to low energy timing jitter and walk: when repeated using the smaller 15 cc planar detector no evidence for nsec lifetimes for these two lines was found.

Unfortunately for the angular distribution measurements, severe drifting in the neutron detector, changes in  $\gamma$  normalizations, detector and electronic malfunctions required that these measurements be repeated yet again. As an added precaution, the gold lined chamber was used. Furthermore, the n/ $\bar{n}\text{-}\gamma$  ( $5E_\gamma$ , nPSA, nYTAC) coincidences were address recorded and several  $\beta$  normalization runs were made over the course of the experiment. Four similar volume Ge(Li) detectors at  $90^\circ$ ,  $60^\circ$ ,  $135^\circ$  and  $155^\circ$  were used. (A fifth counter (15 cc) at  $165^\circ$  malfunctioned in the middle of the experiment so its spectra are not reliable for the angular distribution measurements.) Superposition of the n- $\gamma$  spectra from different angles after matching the gains (via  $\bar{n}\gamma$  in beam decay lines) showed no signs of any centroid doppler shifts within experimental errors. The 873 and 1147

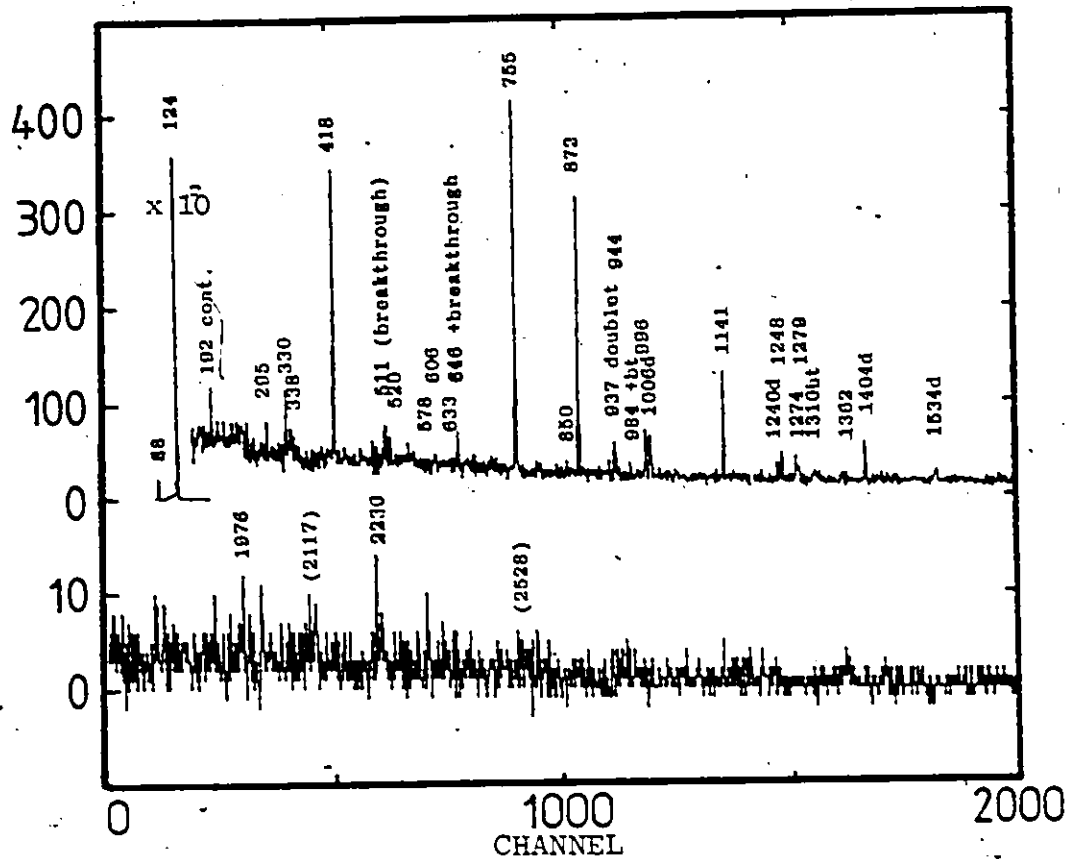
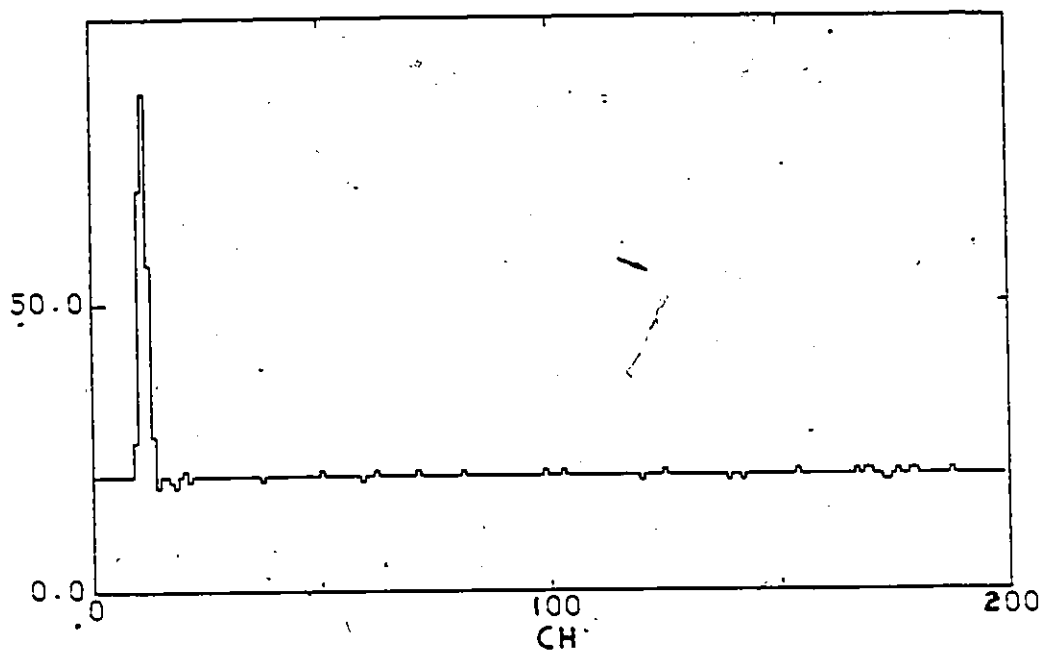


Figure 4.15. Clean n $\gamma$  coincidence spectrum for  $^{61}\text{Zn}$  using gold beam dump, 11% intrinsic Ge  $\gamma$  detector and sorted from address recorded {E $_{\gamma}$ , nPSA, nPHA, n $\gamma$ TAC} data at 15 MeV.



1 CHANNEL  $\approx$  1 NSEC

Figure 4.16. 1141 keV gate  $\gamma$  TAC spectrum for  $\gamma$  events of previous figure.



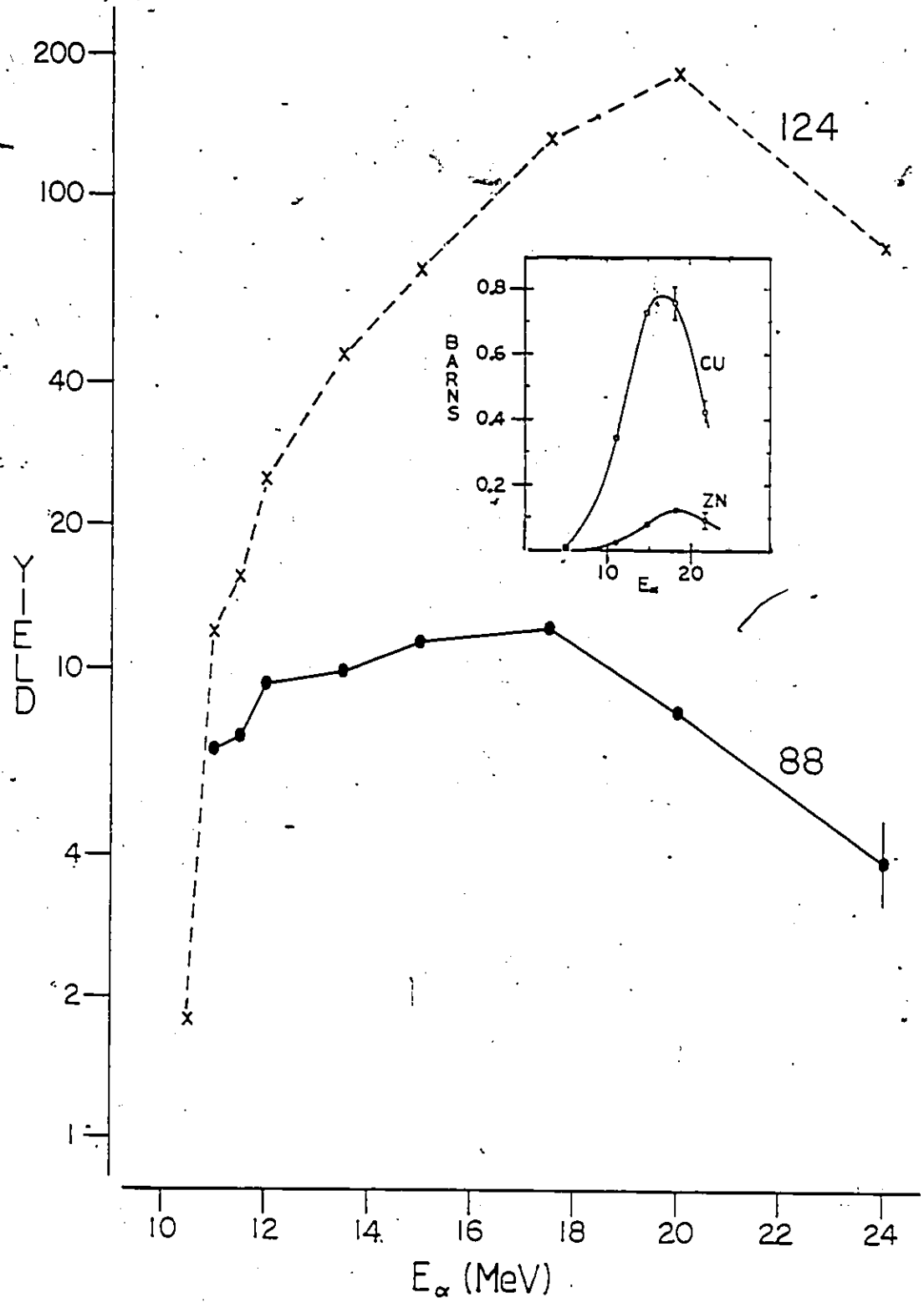
keV lines did show a slight high energy tail at forward angles and low energy tail at back angles but the effect is small and may possibly be attributed to peak shape responses of the detectors. In any case, the effects on the tails and shifts for the  $^{61}\text{Cu}$  lines with known lifetimes (Sarantites) could be seen in the  $\bar{n}\gamma$  and  $\gamma$  singles spectra. (The maximum possible shifts (if decay time  $\ll$  stopping time) are on average larger for  $^{61}\text{Zn}$  than for  $^{61}\text{Cu}$  because the Q value is more negative, so the recoil velocity is greater.) Conservative lower and upper limits for the lifetimes of all the stronger  $^{61}\text{Zn}$  levels seen in the  $(\alpha, n\gamma)$  work are between 1 psec and 5 nsec, respectively.

Angular distributions were also measured in singles mode using a moving counter, with a second counter fixed at  $90^\circ$  to serve as a monitor. Reliable distributions of the 88, 123, 418, 756, 873 and 1141 keV lines were obtained. There was still no evidence of any doppler shift effects for the  $^{61}\text{Zn}$  lines.

In order to minimize dealignment from top feeding and enhance the gaussian alignment for side feeding for the 88 and 123 keV lines, singles angular distributions were also measured slightly above threshold at 11.5 MeV  $\alpha$  bombarding energy.

Singles mode yields with projectile energy were taken as a function of bombarding energy using both the 15 cc and 11% detectors. The yields of the 88 and 123 keV lines

Figure 4.17. Singles  $\gamma$  yields for 88 and 123 keV lines at  $90^\circ$ . Inset: Excitation functions for the reactions  $^{58}\text{Ni}(\alpha, p)^{61}\text{Cu}$  and  $^{58}\text{Ni}(\alpha, n)^{61}\text{Zn}$  of Cumming (1959).



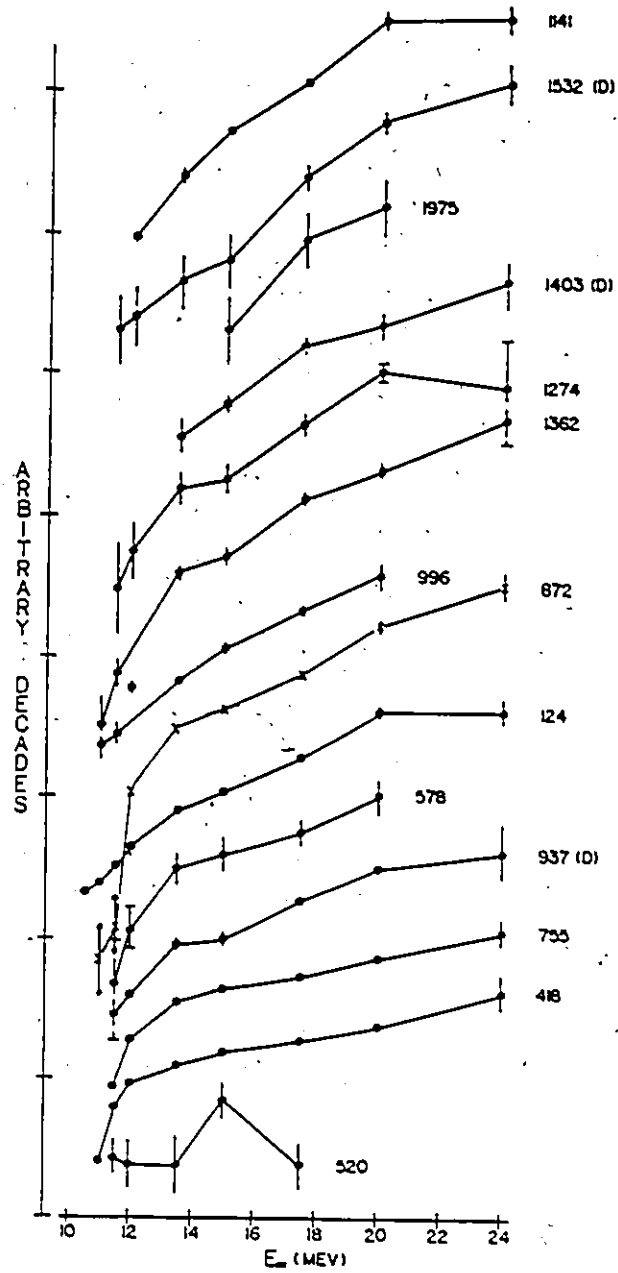


Figure 4.18. Singles  $\gamma$  yields relative to 88 keV line at  $90^\circ$ .

taken at  $90^\circ$  are shown in Figure 4.17. For comparison, the  $(\alpha, n)$  and  $(\alpha, p)$  excitation functions via off line chemical separation and  $\beta$  and  $\gamma$  scintillation techniques of Cumming (1959) are also indicated in Figure 4.17 (insert). Singles yields of well separated lines relative to 88 keV yields are plotted in Figure 4.18. A singles spectrum taken with the 11% detector (4 MeV full scale) at 15 MeV and  $90^\circ$  is shown in Figure 4.19.

For the angular distribution analyses, an initial pass assuming complete alignment ( $\sigma=0$ ) was made. For levels with appreciable top feeding, populations of the m-substates were varied individually and/or via the (modified) gaussian model. Finally, some estimates of m state populations were made by weighting the  $U_k$  coefficients for the top feeding intensities under preferred spin assumptions. The uppermost  $\gamma$ 's in the cascades are expected to exhibit complete alignment, at least for the n- $\gamma$  coincidence work. Dealignment due to finite neutron detector size can be ignored due to the small size and location of the detector (the effective solid angle is considerably less than the example given by Litherland and Ferguson (1963) where dealignment effects were already shown to be small). The angular distributions and  $x^2$  vs  $\delta$  plots for the 756 keV line illustrate the methods used: Figures 4.20 to 4.22 show the plots for 20 MeV n $\gamma$ , 15 MeV singles, and 15 MeV n $\gamma$  with pure alignment (i) with varying populations, (ii) and with pure alignment

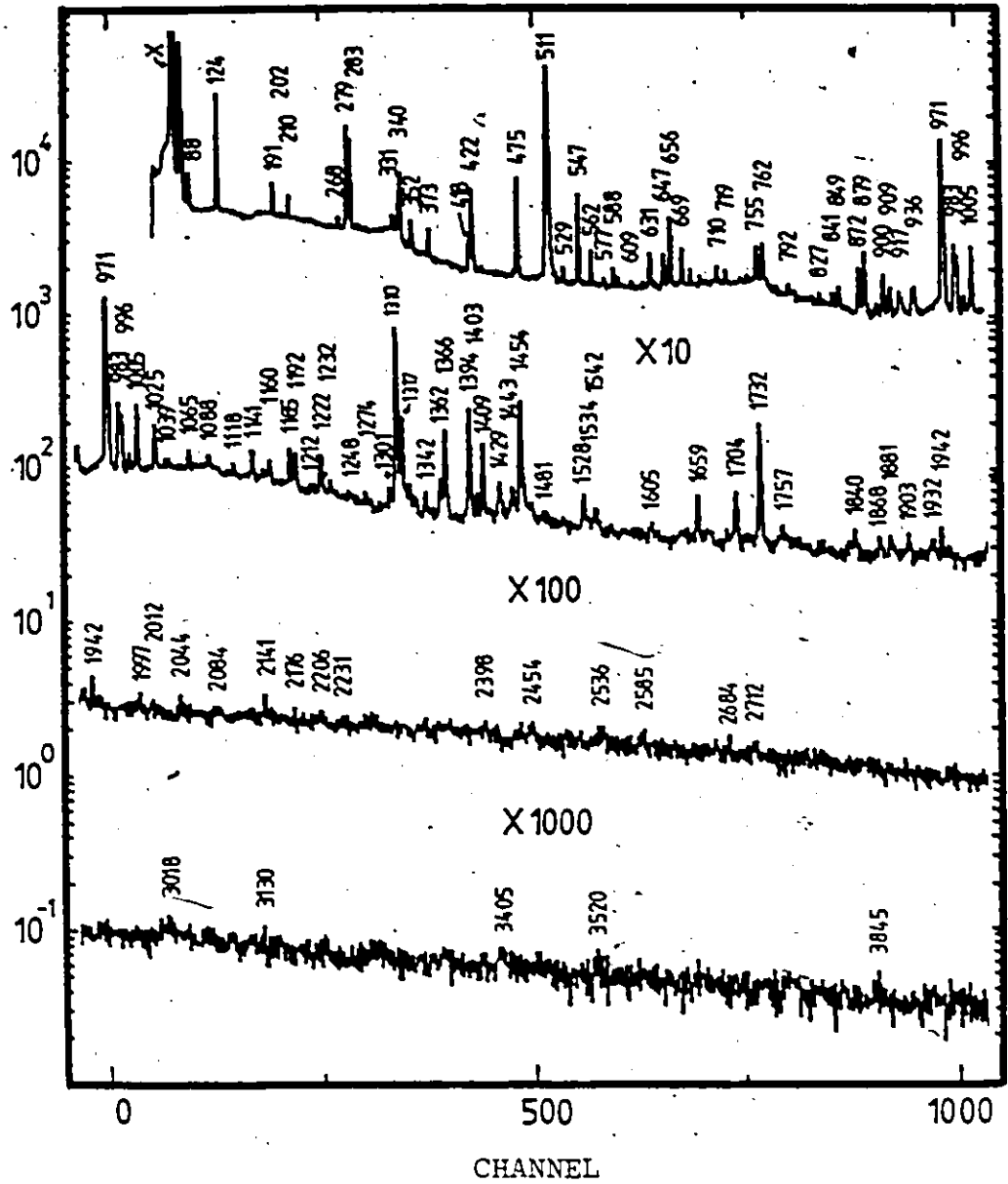
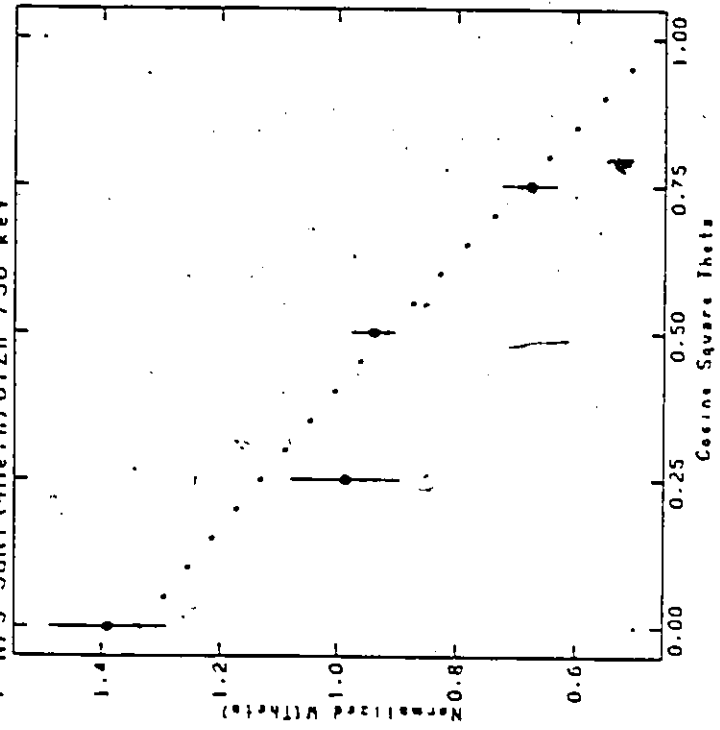


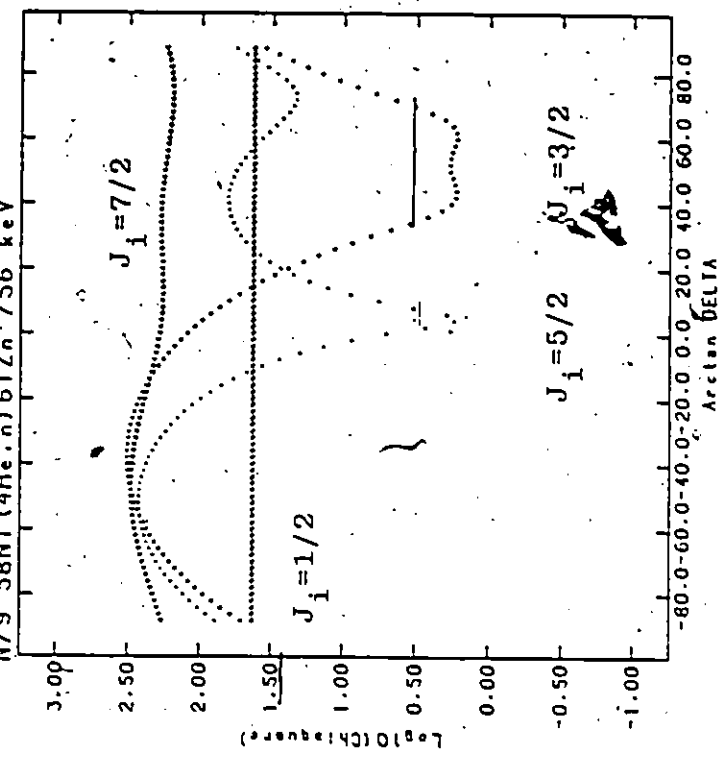
Figure 4.19. High resolution singles spectrum at  $E_c = 15 \text{ MeV}$ ,  $90^\circ$ .

Figure 4.20. 756 keV  $\gamma$  angular distribution and  $\chi^2$  vs  $\delta$  plots at  $E_\alpha = 20$  MeV

N79 58Ni (4He,n)61Zn 756 keV



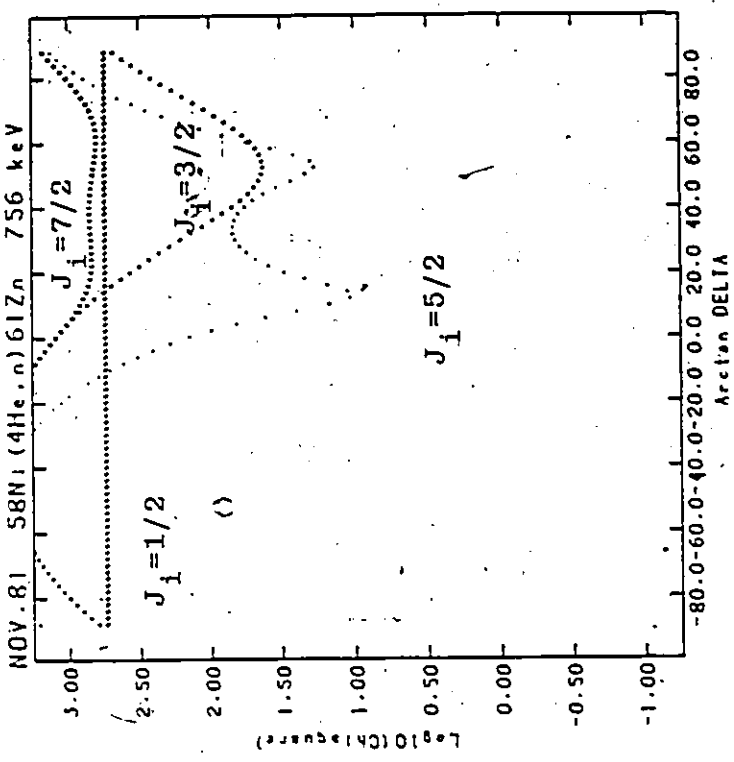
N79 58Ni (4He,n)61Zn 756 keV



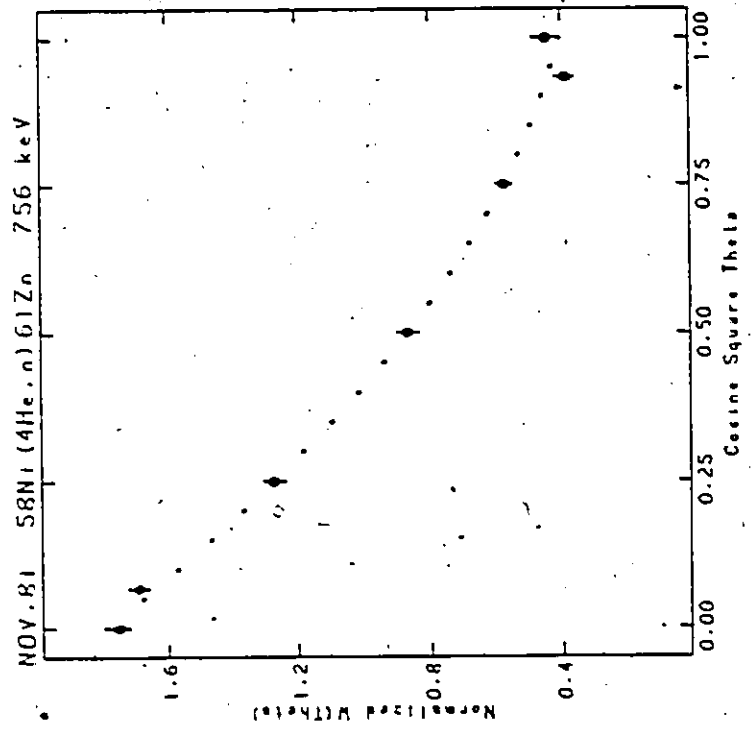
sigma=0.0  $J_f = 3/2$

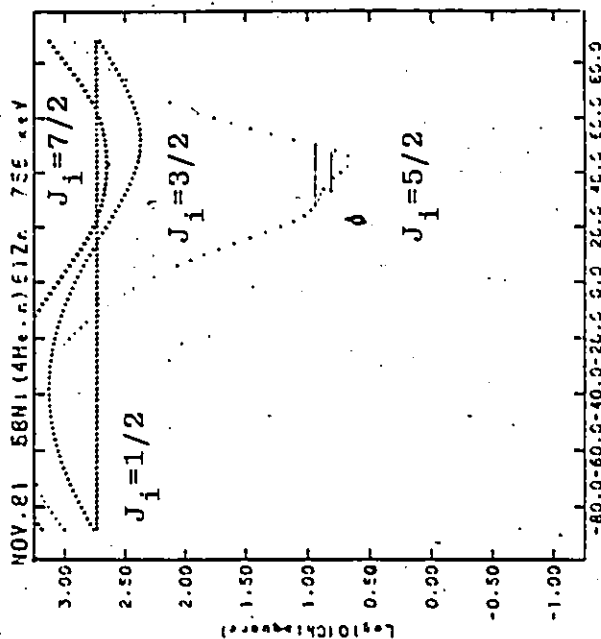


Figure 4.21. 756 keV  $\gamma$  singles angular distribution and  $\chi^2$  vs  $\delta$  plots at  $E_{\alpha} = 15$  MeV

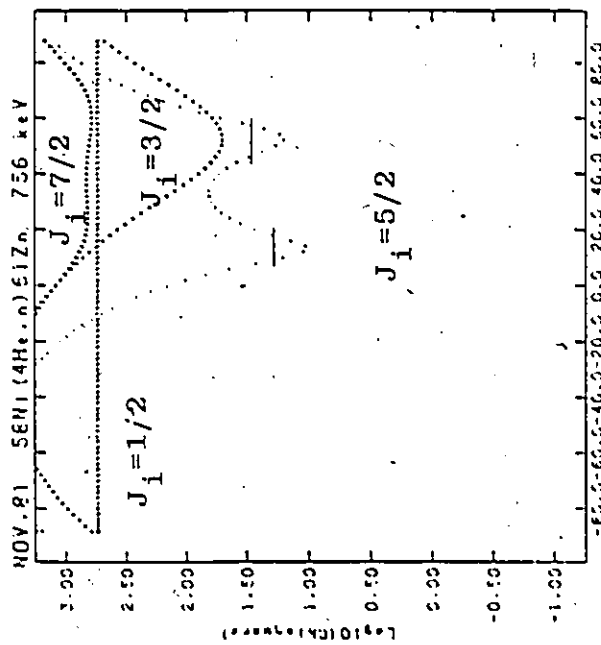


sigma=0.0  $J_f = 3/2$



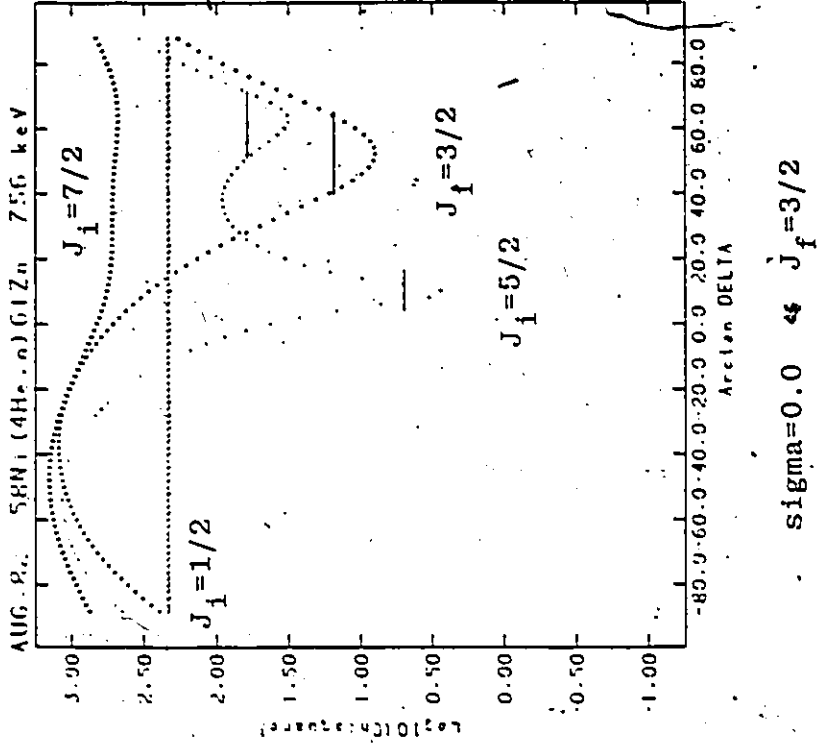
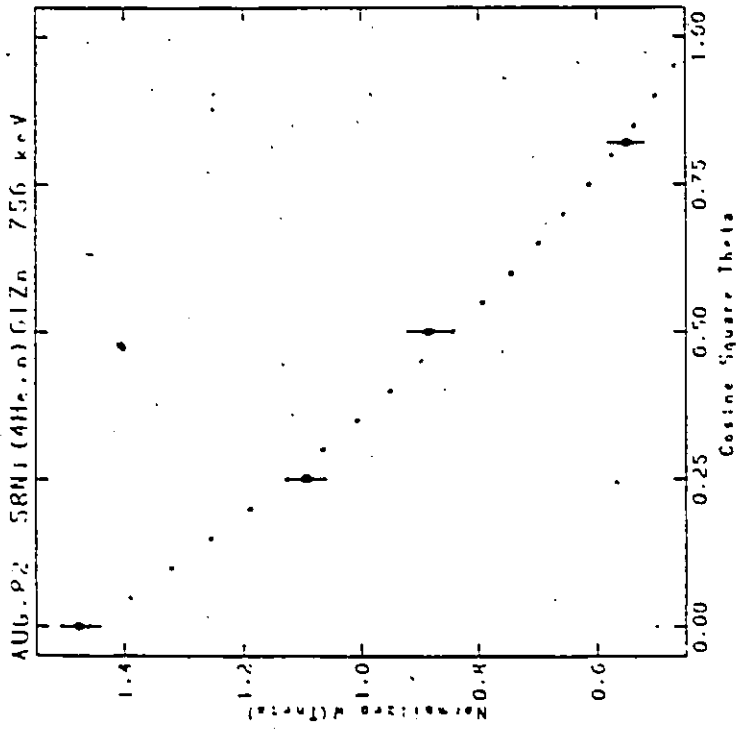


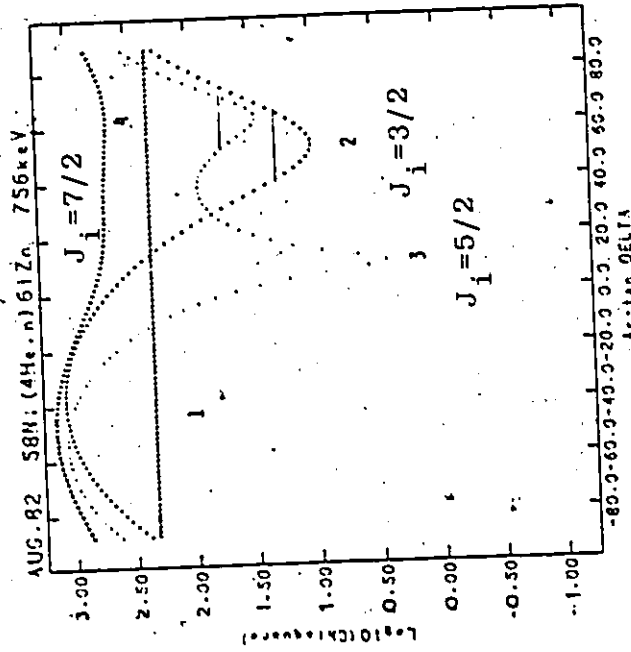
$\sigma = 1.0$   $J_f = 3/2$



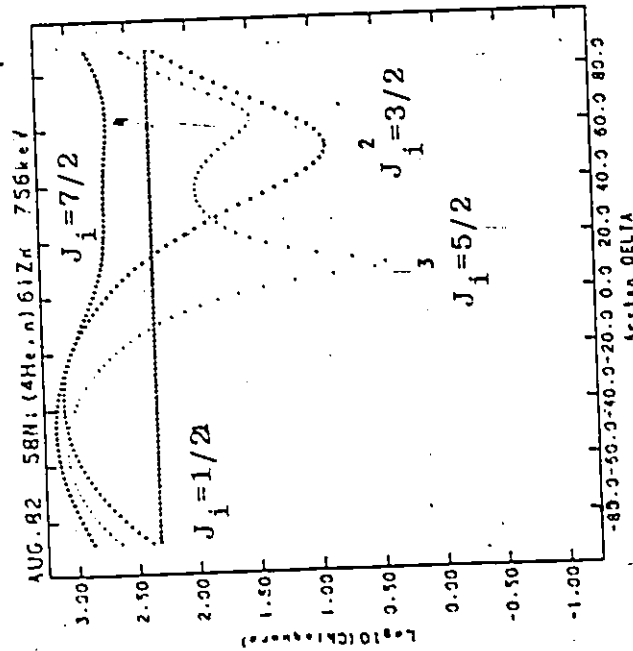
$\sigma = 0.5$   $J_f = 3/2$

Figure 4.22. 756 keV  $n\gamma$  angular distributions and  $\chi^2$  vs  $\delta$  plots at 15 MeV.  $\alpha$ : case i -- if  $\theta=0$  (perfect alignment) is considered, ii -- allowing populations to vary; iii --  $\theta=0$  for side ( $n$ ) feeding weighted with  $U_k$  dealignment for top ( $\gamma$ ) feeding.

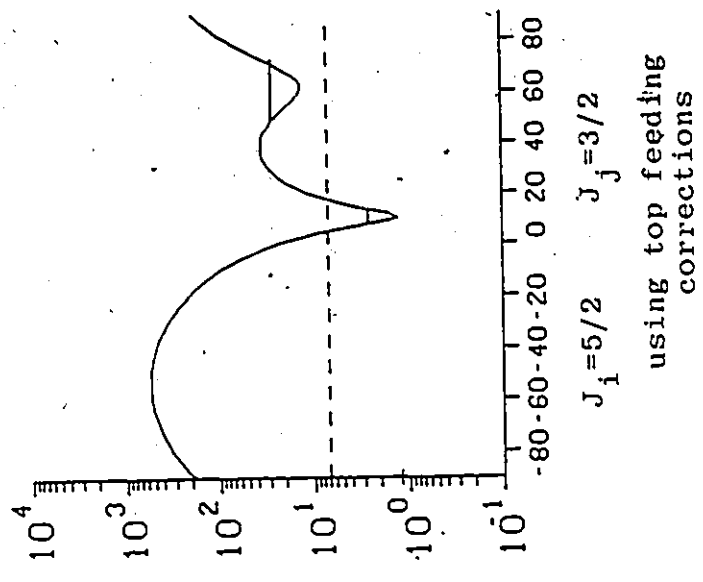
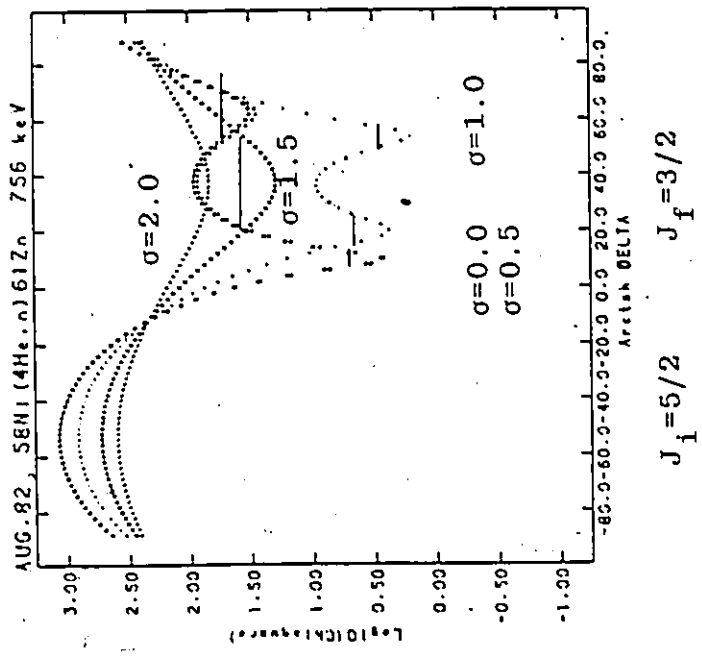




sigma=0.5  $J_f = 3/2$



sigma=0.25  $J_f = 3/2$



2

for side feeding weighted with top feeding via  $U_k$  coefficients (iii), respectively.

Parity assignments were based on mixing ratios, lifetimes and systematics of the odd-zinc isotopes (positive parity states are expected to occur only above 2 MeV in excitation. It must be emphasized that systematics arguments fall under the (very) weak category. A tabulation of the different types of arguments may readily be found in the preface to any volume of the Nuclear Data Sheets, eg., Auble (1975) and Ekström (1983).

Table 4.4 summarizes the results of all the  $(\alpha, n\gamma)$  measurements performed in this project and by Smith et al. (1982). The listed branching ratios are based upon the  $60^\circ$   $n\text{-}\gamma$  intensities, except where indicated. Relative intensities of the stronger  $\gamma$ -rays are based upon the 15 MeV  $60^\circ$   $\gamma$ -singles data, thereby removing any extraneous energy dependence in the neutron detector. (This is not necessary for the branching ratios as the  $\gamma$ -rays originate from the same levels.) The proposed level scheme based on the  $(\alpha, n\gamma)$  data is shown in Figure 4.23.

A neutron spectrum of the  $(\alpha, n)$  reaction at 14 MeV bombarding energy taken with the Seforad neutron detector is shown in Figure 4.24. Although the detector was calibrated by the  $^{27}\text{Al}(p, n)^{27}\text{Si}$  reaction at 7, 8 and 9 MeV, an in beam energy calibration was found to be more reliable. Calibration points corresponding to the ground state, 755 and 1265



Summary of (n,n')<sup>61</sup>Zn work  
 Table 4.41: Present at work at E<sub>0</sub> = 15 MeV

E <sub>ex</sub>	E <sub>γ</sub>	J <sub>π</sub> <sup>1</sup> - J <sub>π</sub> <sup>2</sup>	1/2 <sup>+</sup> - 3/2 <sup>-</sup>	1/2 <sup>+</sup> - 3/2 <sup>-</sup>	RR (%)	g <sub>2</sub>	g <sub>4</sub>	tan <sup>-1</sup> g <sub>4</sub> /g <sub>2</sub>	g <sub>2</sub> g <sub>4</sub>	g <sub>2</sub> <sup>2</sup> g <sub>4</sub> <sup>2</sup>	at slope <sup>a</sup>
88.52±.12	88.52±.12	1/2 <sup>-</sup> - 3/2 <sup>-</sup>	18.0±.9	100		not reliable				3x10 <sup>3</sup>	80±.03
123.73±.04	123.73±.04	5/2 <sup>-</sup> - 3/2 <sup>-</sup>	3100±5	100		not reliable				3x10 <sup>5</sup>	.32±.03
618.20±.12	618.20±.13	3/2 <sup>-</sup> - 3/2 <sup>-</sup>	17.7±.9	65±4		-.15±.04	-.00±.03	623.±.82±3		1280	.08±.04
	330.03±.16	- 1/2 <sup>-</sup>	2.0±.3	9.6±1.4		.02±.10	.13±.20	-1247.75±7		111	
	294.53±.28	- 3/2 <sup>-</sup>	1.1±.2	5.3±1.0		.28±.19	.20±.26	19±1.39±1		2880	.45±.08
755.31±.12	755.31±.12	5/2 <sup>-</sup> - 3/2 <sup>-</sup>	23.9±1.4	97±6		-.66±.12	.10±.02	4.2±(8K)		210	.16±.03
	631.45±.6	- 3/2 <sup>-</sup>	.3±.4	1.3±1.7		.28±.35	1.63±.47	16±80		170	
	337.0±.7	- 3/2 <sup>-</sup>	.3±.2	1.3±.9		-.14±.03	-.16±.05	-8±3		382	
938.08±.24	938.10±.30	1/2 <sup>-</sup> - 3/2 <sup>-</sup>	2.3±.3	38±5		.42±.37	.73±.53	--		0	.08±.07
	849.57±.41	- 1/2 <sup>-</sup>	2.3±.5	38±8		-.00±.20	.52±.30	--		0	.35±.07
	518.77±.26	- 3/2 <sup>-</sup>	1.8±.5	26±8						2.6	
996.12±.12	996.34±.26	7/2 <sup>-</sup> - 3/2 <sup>-</sup>	15.0±1.1	46±3		.19±.05	-.49±.09	[E2] (8±8)		780	.43±.03
	672.37±.13	- 5/2 <sup>-</sup>	18.0±1.2	53±4		-.77±.03	-.24±.08	63±3 (8K)		1680	.27±.03
	578.26±.40	- 3/2 <sup>-</sup>	1.0±.5	2.9±1.5		.98±.29	.31±.41	[E2] (20±20)		780	.87±.11
1264.91±.16	1264.18±.18	9/2 <sup>-</sup> - 5/2 <sup>-</sup>	29.1±1.8	100		.35±.06	-.28±.08	[E2] (4±5)		908	.29±.03
1360.98±.40	1361.36±.49	3/2 <sup>+</sup> - 3/2 <sup>-</sup>	4.7±.7	51±8		-.02±.16	.35±.20	16±9/-10±6		2/180	.31±.03
	1237.35±.32**	- 5/2 <sup>-</sup>	2.2±.6	26±6						5/24	.39±.08
	941.52±.33	- 3/2 <sup>-</sup>	1.6±.4	17±4		-.68±.29	-.68±.50	80±22/10±1		268/12	
	604.91±.60	- 5/2 <sup>-</sup>	.8±.4	9±4		-.50±.36	.43±.30	-24.78/50±1		1850/1120	846/8779±80K
1401.66±.31	1401.66±.30**	7/2 <sup>-</sup> - 3/2 <sup>-</sup>	12±3	69±18		not reliable		.2±.2			.08±.09
	1278.89±.44	- 5/2 <sup>-</sup>	2.9±.5	17±3		-.54±.30	-.10±.74	6±1.75±1		1400/8400	212/28000
	982.87±1.06	- 3/2 <sup>-</sup>	2.1±.6	12±3		.20±.29	-.75±.43	14±1.68±1		180/33000	2/40000
	616.40±.22	- 5/2 <sup>-</sup>	4±.2	2.3±1.2		-.19±.47	.04±1.1	-4±14		41/23000	21/380000

Summary of (e,av)<sup>63</sup>Zn work  
Table 4.41 (cont'd)

$E_{ex}$	$E_{\gamma}$	$J_{\gamma}^{\pi} - J_{\gamma}^{\pi'}$	$I_{123}^{\dagger}$	BA (\$)†	$E_2$	$E_4$	$\tan^{-1} \theta$	BA <sub>W.U.</sub>	$\chi^2$ r.u.	at slope <sup>g</sup>
1659.31±.37	1535.58±.37	$(\frac{5}{2}^-) - (\frac{5}{2}^-)$	3.1±.6	78±18	-39±.13	-98±.21	$82 \frac{-17}{-18} \frac{-11}{-11}$	16000/33	38000/0	.24±.10
	1241.01±.37**	- 3/2	1.4±.6	22±10	-0.0±.12	-21±.25	-10±.6/8.7±.23	400/13000	38 / E2	.53±.08(c)
2002.13±.37	1247.6±.3	9/2	6.8±.7	68±8	.30±.11	-39±.16	$122 \frac{8.6}{8.6}$	3000	107	.15±.10
	1008.8±.4 <sup>g</sup>	- 7/2	3.5±.6	31±6	-77±.11	.13±.18	14±.14	38000	E2	-.07±.04(c)
2098.67±.37	1974.94±.37	7 - 5/2	1.2±.3	100						
2269.80±.35	1215.74±.33	$(\frac{7}{2}^-) - (\frac{7}{2}^-)$	8.4±.8	957±2	.28±.10	-81±.14	-61±.5/9±.8	38000	3515	.40±.04
	1004.99±.38	- 9/2	4.2±.2	52±2						.89±.13(c)
2399.78±.19	1403.60±.18**	$(\frac{7}{2}^-) - (\frac{7}{2}^-)$	4.6±.7	100	not reliable			(32000)	(E2)	.42±.04
2798.69±.44	1531.78±.44	$(\frac{8}{2}^-) - (\frac{8}{2}^-)$	6.2±.7	100	-26±.12	-47±.18	$-88 \frac{15.4}{15.4} \frac{11}{11} \frac{6.2}{6.2} \frac{11}{11}$	14000	1417	.20±.08
3336.61±.26	938.85±.23 <sup>g</sup>	$(\frac{11}{2}^-) - (\frac{11}{2}^-)$	3.0±.6	100	not reliable					.44±.09
	(4412.6±.6 <sup>g</sup> 1078.0±.5 <sup>g</sup> )									

† 938 doublet resolved by coin. windows and energy shifts; unfolded areas for ang. dist. are not fully uncorrelated.  
 \* 1004 doublet resolved by energy sums and shifts; most of intensity belongs to 1007.  
 \*\* 1241 doublet resolved by energy sums and shifts; most of intensity belongs to 1241.  
 \*\*\* 1403 doublet resolved by coin. windows and energy shifts; unfolded areas for ang. dist. are not fully uncorrelated.  
 (c) possible intrusion by Ni/Cu Xy lines  
 ‡ seen only in (Wg,2pa) experiment  
 § at intensities measured at 60°  
 ¶ at slope 1.0±.2 in ((for @ 20 KeV)/(av @ 15 KeV))

Summary of (n,n $\gamma$ )<sup>61</sup>Zn work

Table 4.411

Present work singles  $\gamma$  at  $E_n = 15$  MeV

$E_{ex}$	$E_\gamma$	$J_1^{\pi_1} - J_2^{\pi_2}$	rel int <sup>2</sup>	BR	$a_2$	$a_4$	$\tan^{-1} a_4$
88	88	1/2 <sup>-</sup> - 3/2 <sup>-</sup>	13.4 $\pm$ 3.5	100	-.04 $\pm$ .06	-.10 $\pm$ .09	
124	124	5/2 <sup>-</sup> - 3/2 <sup>-</sup>	8100 $\pm$ 3	100	-.13 $\pm$ .01	-.02 $\pm$ .02	3 $\pm$ 1
418	418	3/2 <sup>-</sup> - 5/2 <sup>-</sup>	15.1 $\pm$ 1.5	77 $\pm$ 6	.10 $\pm$ .03	-.01 $\pm$ .04	10. -86 $\pm$ 2
	330	- 1/2 <sup>-</sup>	4.5 $\pm$ 1.0	23 $\pm$ 5			
755	755	5/2 <sup>-</sup> - 3/2 <sup>-</sup>	30.0 $\pm$ 3.4	<100	-.71 $\pm$ .03	.15 $\pm$ .03	12.52 $\pm$ 3
	631 cont		<<34. $\pm$ 3.1				(6 $\pm$ 2 BR)
	337 cont		<8.9 $\pm$ 1.3				
938	937 cont	1/2 <sup>-</sup> - 3/2 <sup>-</sup>	<15.4 $\pm$ 3.1				
	850 cont	- 1/2 <sup>-</sup>	<17.3 $\pm$ 3.5				
	520	- 3/2 <sup>-</sup>	2.6 $\pm$ 1.3				
996	996	7/2 <sup>-</sup> - 3/2 <sup>-</sup>	15.5 $\pm$ 3.3	33 $\pm$ 7	not reliable		
	872	- 5/2 <sup>-</sup>	23.6 $\pm$ 3.1	51 $\pm$ 7	-.37 $\pm$ .03	-.04 $\pm$ .04	11 $\pm$ 1
	578	- 3/2 <sup>-</sup>	7.2 $\pm$ 2.1	16 $\pm$ 5			
1265	1141	9/2 <sup>-</sup> - 5/2 <sup>-</sup>	21.9 $\pm$ 3.9	100	.40 $\pm$ .03	-.24 $\pm$ .04	1. 86 $\pm$ 2
1364	1361 cont	( $\frac{3}{2}, \frac{5}{2}$ ) - 3/2 <sup>-</sup>	<<23.9 $\pm$ 3.1	<100			
1402	1402 cont	7/2 <sup>-</sup> - 3/2 <sup>-</sup>	12.5 $\pm$ 3.0	<100	not reliable		
	982 cont						
	646 cont						
2270	1274	( $\frac{7}{2}, \frac{11}{2}$ ) - 7/2 <sup>-</sup>	5.7 $\pm$ 1.5	<100			
	1005 cont						
2400	1404 cont	( $\frac{7}{2}, \frac{9}{2}, \frac{11}{2}$ ) - 7/2 <sup>-</sup>	4.7 $\pm$ 2.7	100	not reliable		

Summary of (n,n $\gamma$ )<sup>61</sup>Zn work

Table 4.4111

Present work singles  $\gamma$  at  $E_n = 11.5$  MeV

$E_{ex}$	$E_\gamma$	$J_1^{\pi_1} - J_2^{\pi_2}$	rel int <sup>2</sup>	BR	$a_2$	$a_4$	$\tan^{-1} a_4$
88	88	1/2 <sup>-</sup> - 3/2 <sup>-</sup>			-.07 $\pm$ .06	-.04 $\pm$ .04	
124	124	3/2 <sup>-</sup> - 3/2 <sup>-</sup>			-.22 $\pm$ .04	-.02 $\pm$ .04	-4 $\pm$ 2

Summary of  $(\alpha, \alpha)^{61}\text{Xe}$  work

Table 4.4iv

Present by work at  $E_\alpha = 30 \text{ MeV}$

$E_x$	$K_y$	$J_1^{\pi} - J_2^{\pi}$	rel int <sup>a</sup>	BR	$a_2$	$a_4$	$\tan^{-1} \delta$
88	88	$1/2^- - 3/2^-$	$3.7 \pm .8$	100	not reliable		
124	124	$5/2^- - 3/2^-$	$9100 \pm 10$	100	not reliable		
418	418	$7/2^- - 3/2^-$	$5.3 \pm .9$	$59 \pm 10$	$.50 \pm .08$	$-.02 \pm .12$	$2 \pm 60 \pm 4$
	330	$- 1/2^-$	$1.5 \pm .4$	$17 \pm 4$			
	396	$- 5/2^-$	$2.1 \pm .7$	$24 \pm 8$			
755	755	$5/2^- - 3/2^-$	$10.4 \pm 1.5$	$> 71 \pm 10$	$-.54 \pm .07$	$-.02 \pm .11$	$5 \pm 3(7 \pm 2) \text{BK}$
	633c	$5/2^-$	$4.4 \pm .9$	7			
	337c	$3/2^-$	7	7			
838	838 <sup>b</sup> c	$1/2^- - 3/2^-$	$.7 \pm 2.3$		$(-.06 \pm .13)$	$(.28 \pm .19)$	
	850	$1/2^-$	$2.0 \pm .4$				
	520	$3/2^-$	$1.8 \pm .7$				
996	996c	$7/2^- - 3/2^-$	$28 \pm 3$	<	not reliable		$4 \pm 4(0 \pm 2) \text{BK}$
	872	$- 5/2^-$	$14 \pm 2$	>	$-.52 \pm .05$	$-.17 \pm .08$	
	578	$- 3/2^-$	$3.5 \pm .9$	>			
1265	1141	$9/2^- - 5/2^-$	$25 \pm 3$	100	$.31 \pm .08$	$-.03 \pm .08$	$0 \pm 1 \text{BK}$
1361	1361	$(\frac{3}{2}, \frac{5}{2})^- - 3/2^-$	$6.2 \pm 1.3$		$.32 \pm .13$	$.16 \pm .16$	$5 \pm 8(5 \pm 5) / -19 \pm 5$
	1237c	$- 5/2^-$	$2.6 \pm .7$		not reliable		
	942	$- 3/2^-$	$4.5 \pm .7$				
	606c	$- 5/2^-$	$45.8 \pm 1.1$				
1402	1402 <sup>c</sup>	$7/2^- - 3/2^-$	$4.1 \pm 1.5$		not reliable		
	1279	$- 5/2^-$	$1.0 \pm .9$				
	982c	$- 3/2^-$	$6.4 \pm 1.5$				
	646c	$- 5/2^-$	$3.8 \pm .9$				
1658	1536	$(\frac{5}{2}, \frac{7}{2})^- - 3/2^-$	$3.1 \pm 1.0$	$32 \pm 15$	not reliable		
	1247c	$- 3/2^-$	$4.9 \pm 1.1$	$68 \pm 17$			
2002	1248	$(9/2)^- - 5/2^-$	$2.9 \pm 1.3$	$55 \pm 28$	$.09 \pm .28$	$-.25 \pm .35$	
	1007c	$- 7/2^-$	$.5 \pm 2.0$	$15 \pm 69$			
2098	not seen						
2270	1274	$(\frac{7}{2}, \frac{11}{2})^- - 7/2^-$	$13 \pm 2$		$-.54 \pm .33$	$-.50 \pm .38$	$66 \pm 10 / 82 \pm 10$
	1006c	$- 9/2^-$	$< 12 \pm 0$				
2400	1404 <sup>c</sup> (c)	$(\frac{7}{2}, \frac{9}{2}, \frac{11}{2})^- - 7/2^-$	$7.8 \pm 2.2$		$.47 \pm .10$	$-.20 \pm .14$	$-.82 \pm .12, 2 \pm 11 / 0 \pm 9 / 0 (\text{BK})$
2787	1532	$(\frac{9}{2}, \frac{13}{2})^- - 9/2^-$	$3.9 \pm 1.0$				
3337	837 <sup>b</sup> c	$(\frac{7}{2}, \frac{13}{2})^- - (\frac{11}{2})^-$	$5.5 \pm 2.3$		$(.06 \pm .13)$	$(-.28 \pm .18)$	

<sup>a</sup> - expect mostly 1404 is 1403 doublet  
<sup>b</sup> - expect mostly 837 is 832 doublet

Table 4.4v

NY work of Smith et al.

Level energies and spin-parities determined for the excited states in  $^{60}\text{Zn}$ , with transitional  $\gamma$  ray energies, relative intensities, branching ratios, measured Legendre coefficients  $a_2$  and  $a_4$ , multipole mixing ratios  $\delta$  and linear polarisations  $P(\gamma)$ . (The  $\gamma$  ray relative intensities were derived from the  $55^\circ$  n- $\gamma$  coincidence data, bombarding energy 15 MeV, and normalised to the 124 keV transition.)

$E_x$ (keV)	$E_\gamma$ (keV)	$J_i^\pi$	$J_f^\pi$	Relative intensity	Branching ratio	$a_2$	$a_4$	$\delta$	$P(\gamma)$
88.0 ± 0.1	88.0 ± 0.1			4.3 ± 0.2	100	-0.03 ± 0.03	-0.07 ± 0.03		
123.6 ± 0.1	123.6 ± 0.1			100	100	-0.25 ± 0.07	-0.05 ± 0.09	-0.01 ± 0.11 or 3.2 ± 1.1	
418.4 ± 0.1	294.8 ± 0.3			2.6 ± 0.3	5				
	330.4 ± 0.3			6.5 ± 0.2	12				0.01 ± 0.20
	418.4 ± 0.1			45.2 ± 0.9	83	0.24 ± 0.03	0.02 ± 0.04	0.04 ± 0.11	0.18 ± 0.08
755.6 ± 0.1	337.0 ± 0.7			3.4 ± 0.1	5				
	632.0 ± 0.7			5.7 ± 0.5	8				
	755.6 ± 0.1			64.4 ± 1.2	87	0.75 ± 0.03	0.08 ± 0.04	0.3 ± 0.1	0.17 ± 0.08
938.0 ± 0.4	520.0 ± 0.4			2.6 ± 0.6	11				
	850.2 ± 0.7			4.4 ± 0.4	19				
	938.0 ± 0.4			16.4 ± 1.0	70				0.8 ± 0.3
996.4 ± 0.2	577.8 ± 0.3			3.8 ± 0.4	5				
	872.7 ± 0.5			49.0 ± 0.8	66	0.73 ± 0.02	0.29 ± 0.02	1.7 ± 0.1	0.14 ± 0.09
	996.4 ± 0.2			21.8 ± 1.0	29	0.31 ± 0.05	0.14 ± 0.05	0.09 ± 0.17	0.32 ± 0.27
1264.7 ± 0.2	1141.1 ± 0.1			63.9 ± 1.0	100	0.42 ± 0.02	0.15 ± 0.02	-0.02 ± 0.11	0.42 ± 0.14
1362.0 ± 1.0	606.0 ± 0.5			1.0 ± 0.1	9				
	944.0 ± 1.0			2.4 ± 0.4	23				
	1362.0 ± 1.0			7.2 ± 0.4	68				
1402.8 ± 0.4	646.7 ± 0.3			7.1 ± 0.5	32				
	984.4 ± 0.3			8.8 ± 0.7	40				
	1278.6 ± 0.7			6.1 ± 0.6	28				
1658.0 ± 1.0	1534.0 ± 1.0			20.9 ± 2.1	100	0.53 ± 0.05	0.05 ± 0.06	0.1 ± 0.1	0.9 ± 0.3
2002.5 ± 0.3	1006.1 ± 0.2			17.8 ± 1.4	58				
	1247.4 ± 0.4			12.9 ± 0.9	42				
2270.0 ± 0.5	1273.7 ± 0.4			12.5 ± 0.5	100				0.4 ± 0.4
2400.0 ± 0.7	1403.6 ± 0.7			34.7 ± 1.5	100				0.1 ± 0.2

† May be contaminated by a possible ground state decay from the 1402.8 keV level.

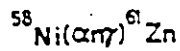
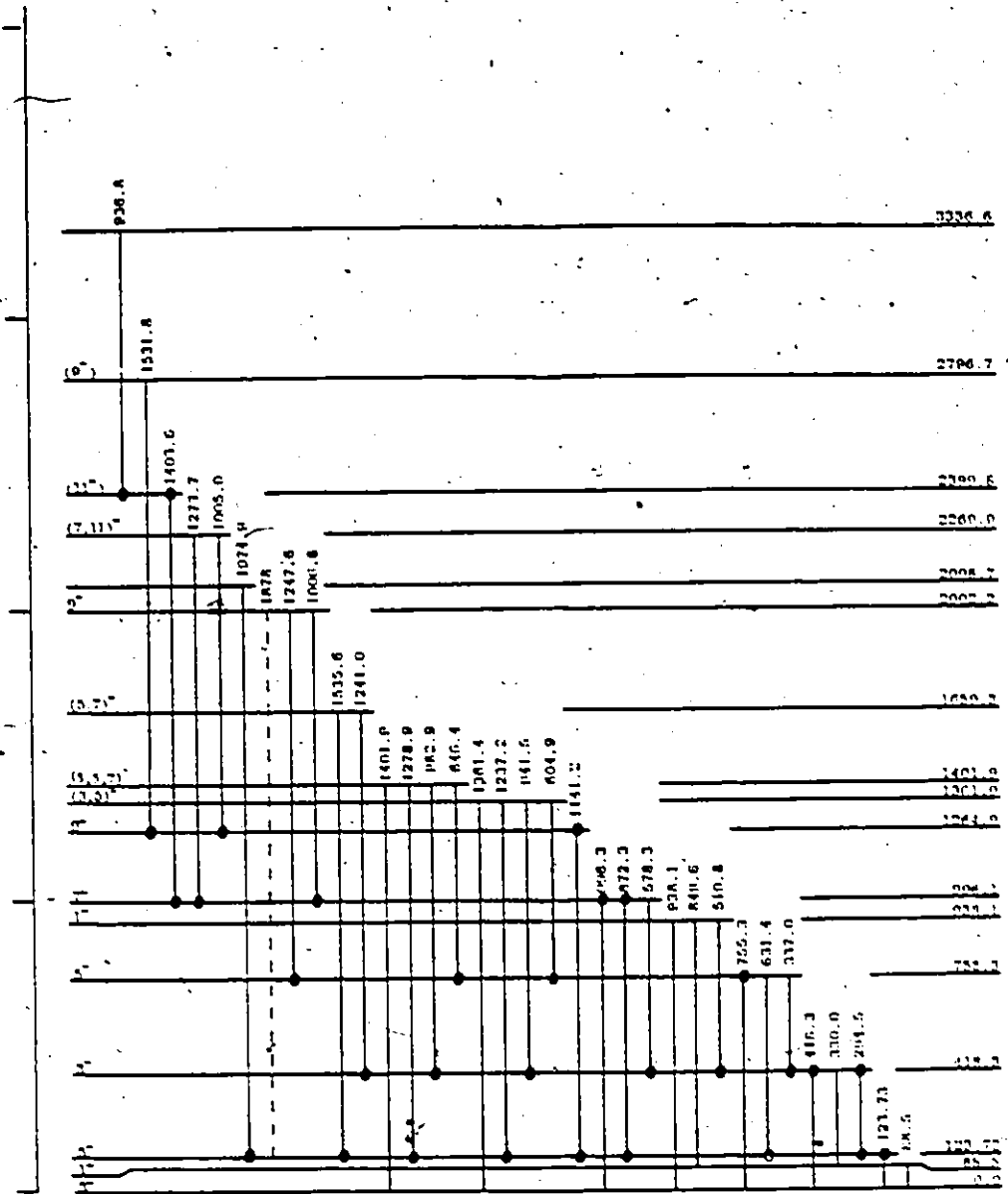


Figure 4.23. Proposed level scheme of  $^{61}\text{Zn}$  based upon the  $(\alpha, n)$  experiments in this project.

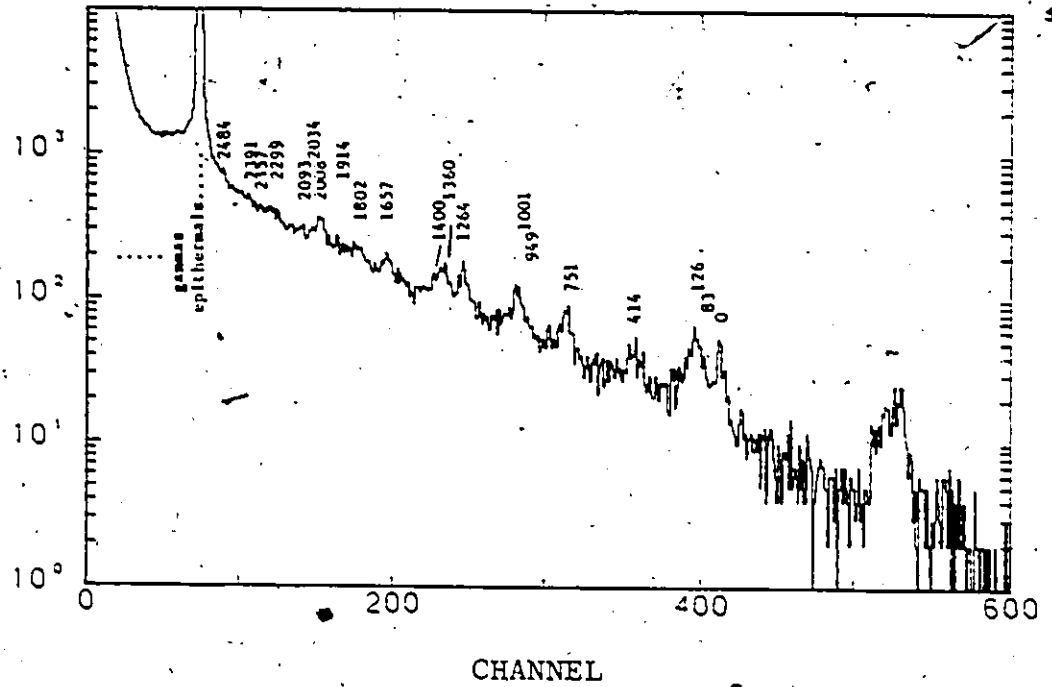


Figure 4.24.  $^{58}\text{Ni}(\alpha, n)^{61}\text{Zn}$  neutron energy spectrum using the Seforad  $^3\text{He}$  ion chamber.

peaks and the epithermal peak were used.

The excitation energies and efficiency corrected intensities are given in Table 4.5. Using the 8 and 9 MeV (p,n) calibration points and correcting for energy losses due to target thickness (Table of Isotopes 1978) the mass excess for  $^{61}\text{Zn}$  was found to be  $-56369 \pm 8$  keV (error includes uncertainties from statistics, energy calibration, calibration masses and beam energies) in good agreement with the value reported by Woods et al. (1978) of  $-56352 \pm 20$  keV.

Singles  $\gamma$  spectra were taken at several bombarding energies for the following reactions:

$^{16}\text{O}$  on  $^{50}\text{Cr}$  @ 49, 55, 60, 65, 70 MeV

$^{10}\text{B}$  on  $^{54}\text{Fe}$  @ 40, 45, 50, 54 MeV

$^6\text{Li}$  on  $^{58}\text{Ni}$  @ 20, 25, 30, 35 MeV

$^{24}\text{Mg}$  on Ca @ 53, 58, 62, 66, 70, 74, 85 MeV

$^{23}\text{Na}$  on Ca @ 50, 55, 60, 65, 70, 75 MeV

Of these five reactions,  $^{16}\text{O}$  on  $^{50}\text{Cr}$  and  $^{23}\text{Na}$  on Ca showed no (useful) yield of  $^{61}\text{Zn}$  in-beam activity. Yields of the 123 keV line generally peaked at 45, 30 and 74 MeV for the  $^{10}\text{B}$ ,  $^6\text{Li}$  and  $^{24}\text{Mg}$  induced reactions, but even at these energies they remain disappointingly small. Figures 4.25 to 4.29 show the singles spectra for the  $^{16}\text{O}$ ,  $^{10}\text{B}$ ,  $^6\text{Li}$ ,  $^{24}\text{Mg}$ , and  $^{23}\text{Na}$  induced reactions taken at 60, 45, 30, 66 and 70 MeV, respectively. A summary of the  $^{61}\text{Zn}$   $\gamma$  lines seen in the heavy ion work is given in Table 4.6 and  $^{61}\text{Zn}$  levels based on  $\gamma$  work in Table 4.8.



Table 4.5

Energies and intensities of  $^{61}\text{Zn}$  levels in the (a,n) reaction

$E_{\text{ex}}$	$\frac{d\sigma}{d\Omega} \left( \frac{\mu\text{b}}{\text{str}} \right)$	$E_{\text{ex}}$	$\frac{d\sigma}{d\Omega} \left( \frac{\mu\text{b}}{\text{str}} \right)$
$0 \pm 2.5$	$63 \pm 11$	$1802 \pm 4$	$57 \pm 10$
$83 \pm 6$	$39 \pm 10$	$(1914 \pm 12)$	$13 \pm 8$
$127 \pm 3$	$72 \pm 13$	$2008 \pm 3$	$132 \pm 14$
$414 \pm 5$	$37 \pm 7$	$2034 \pm 3$	$37 \pm 10$
$751 \pm 3$	$71 \pm 9$	$2093 \pm 7$	$30 \pm 11$
$949 \pm 9$	$13 \pm 5$	$2299 \pm 10$	$10 \pm 8$
$1001 \pm 3$	$90 \pm 10$	$2357 \pm 8$	$13 \pm 9$
$1264 \pm 3$	$125 \pm 11$	$2391 \pm 10$	$6 \pm 6$
$1360 \pm 6$	$86 \pm 21$	$2484 \pm 5$	$13 \pm 8$
$1400 \pm 11$	$49 \pm 12$		
$1657 \pm 3$	$61 \pm 7$		

$$\frac{d\sigma}{d\Omega} = \frac{\text{peak area}}{c \text{ (wrt 1 MeV)}} \times \frac{1}{\text{pt}} \times \left\{ \frac{1}{c \text{ (wrt 1 MeV)}} \times \frac{1}{\Omega} \right\} \times \frac{e}{\text{chg}} \times \frac{A}{N_A} \times 10^{30} \left( \frac{\mu\text{b}}{\text{str}} \right)$$

$$A = .58$$

$$\text{pt} = 40 \times 10^{-6} \text{ g/cm}^2$$

$$\Omega \times c \text{ (1 MeV)} = 5.1 \times 10^{-5} \text{ str}$$

$$e = 1.602 \times 10^{-19} \text{ coul.}$$

$$\text{chg} = \frac{1108614}{2} \times 6 \times 10^{-6} \text{ coul.}$$

$$c \text{ (wrt 1 MeV) from relative eff. graph}$$

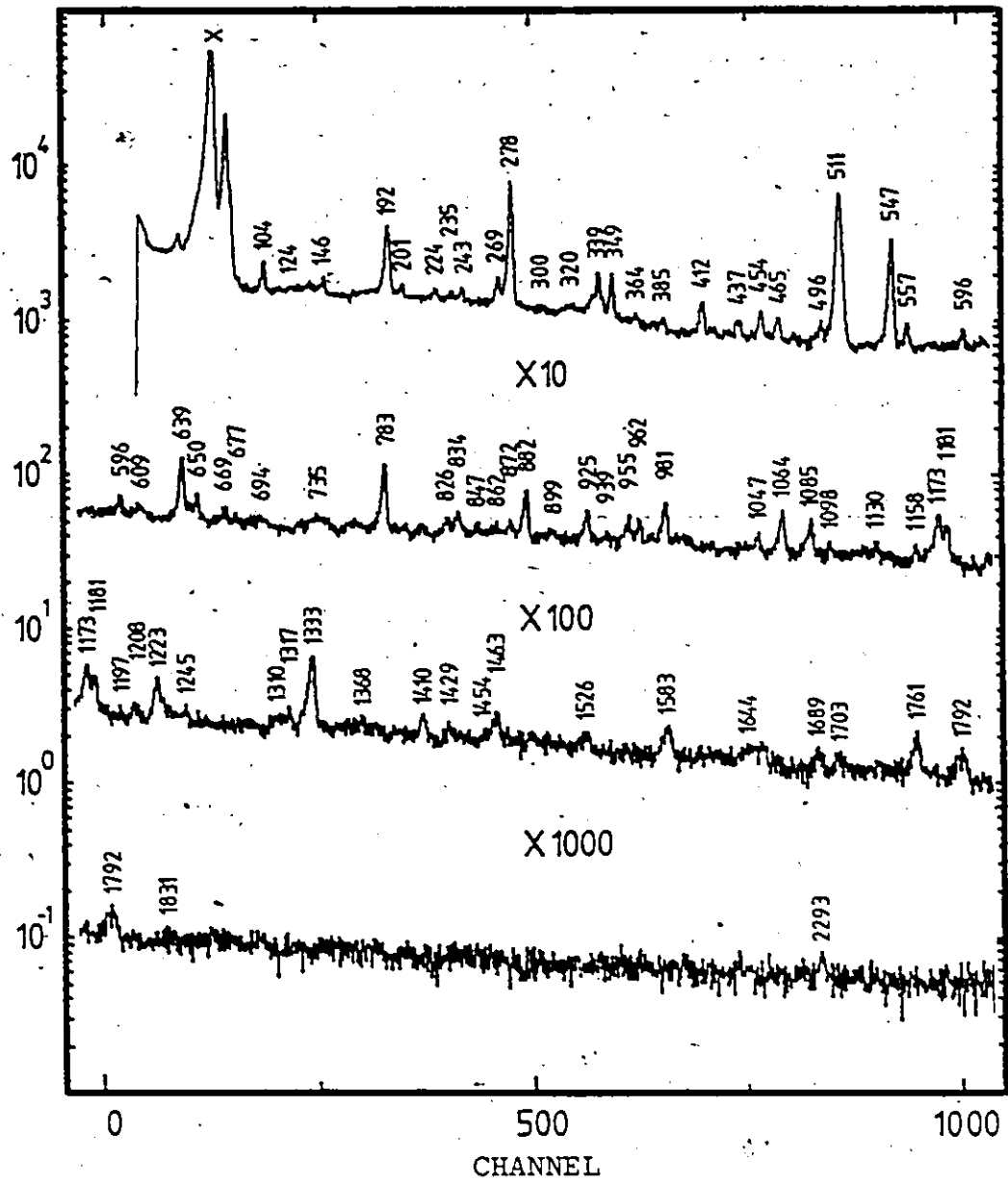


Figure 4.25.  $^{16}\text{O}$  on  $^{50}\text{Cr}$  singles  $\gamma$  spectrum at 60 MeV.

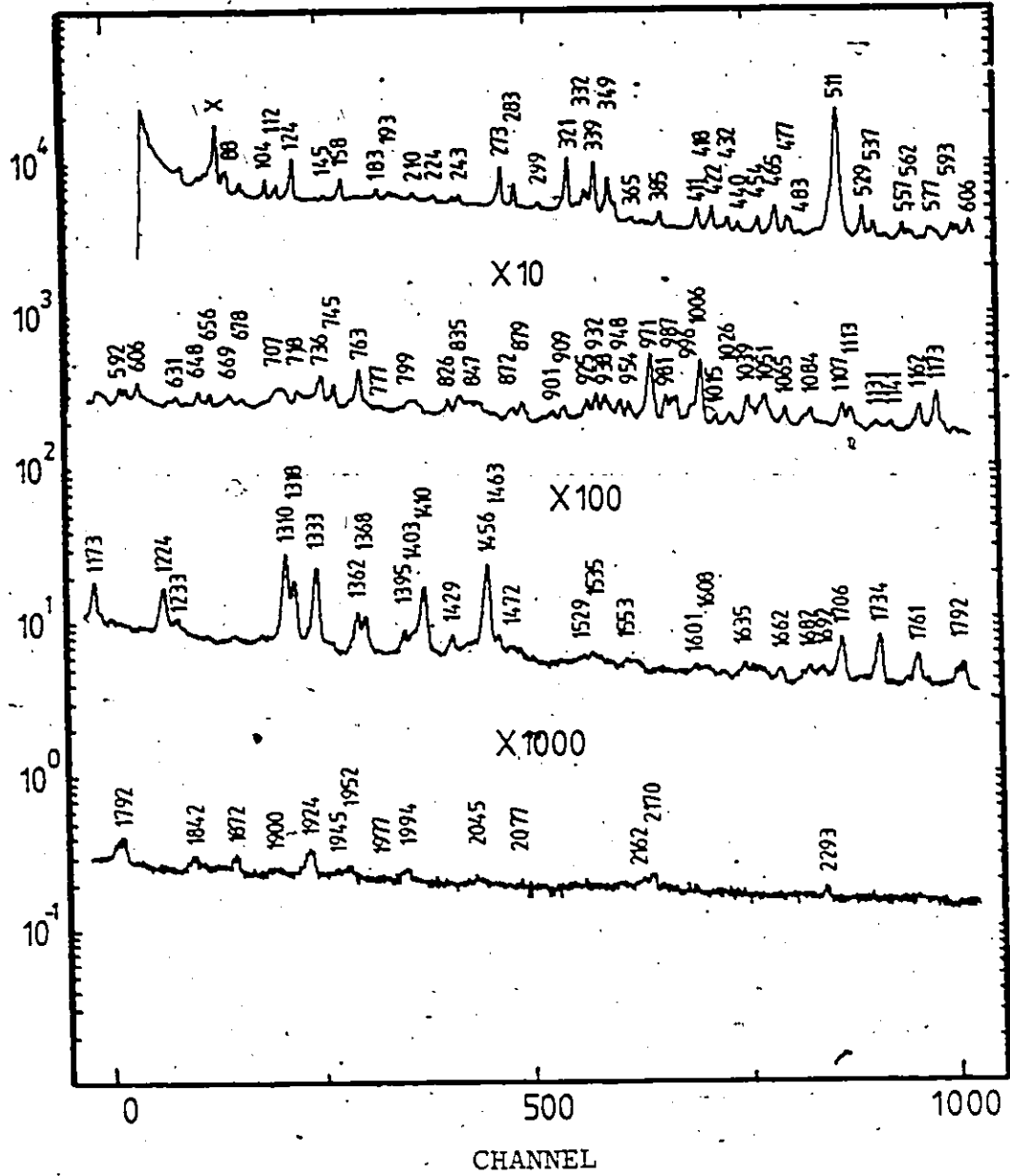


Figure 4.26.  $^{10}\text{B}$  on  $^{54}\text{Fe}$  singles  $\gamma$  spectrum at 45 MeV.

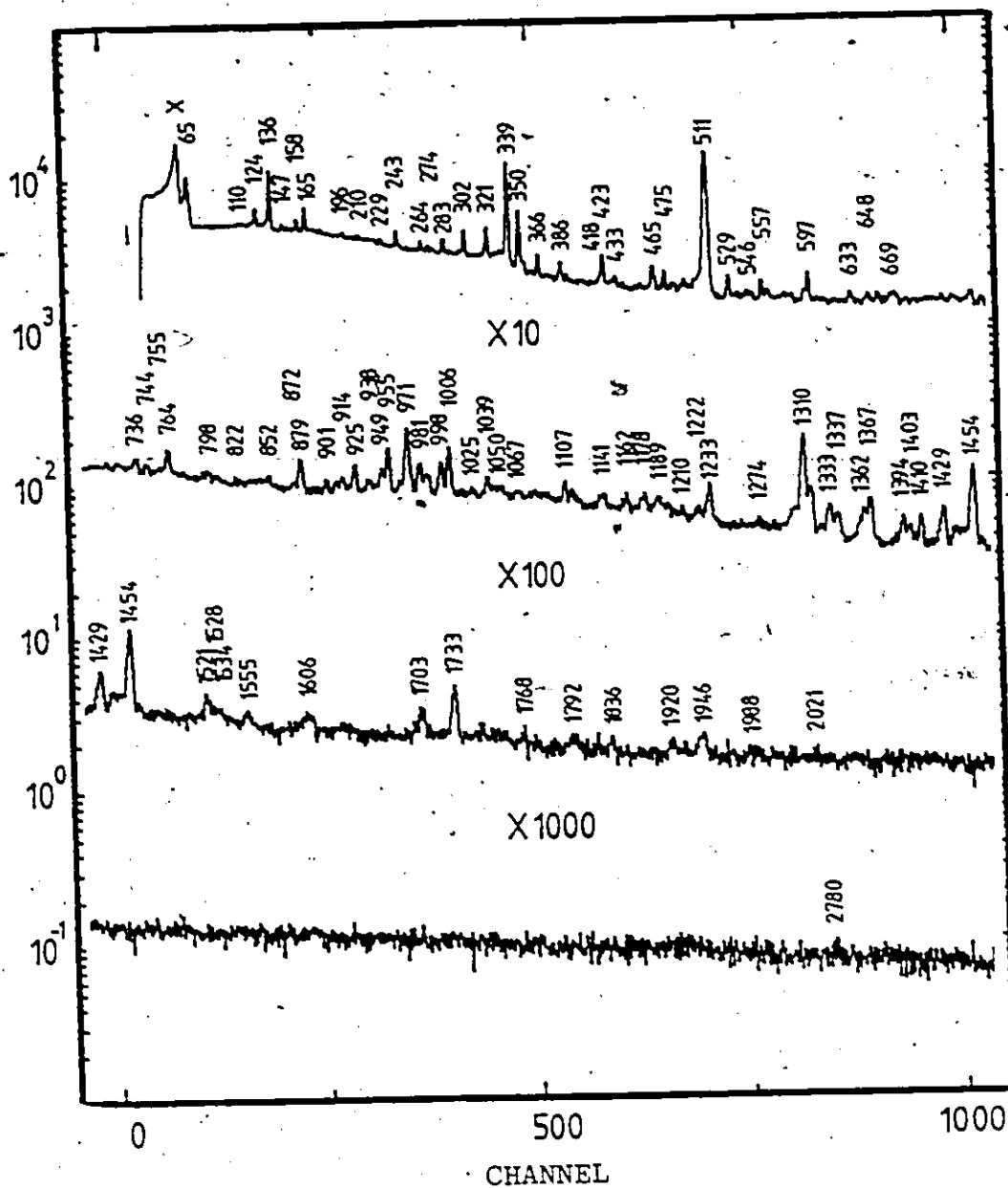


Figure 4.27.  ${}^6\text{Li}$  on  ${}^{58}\text{Ni}$  singles  $\gamma$  spectrum at 30 MeV.

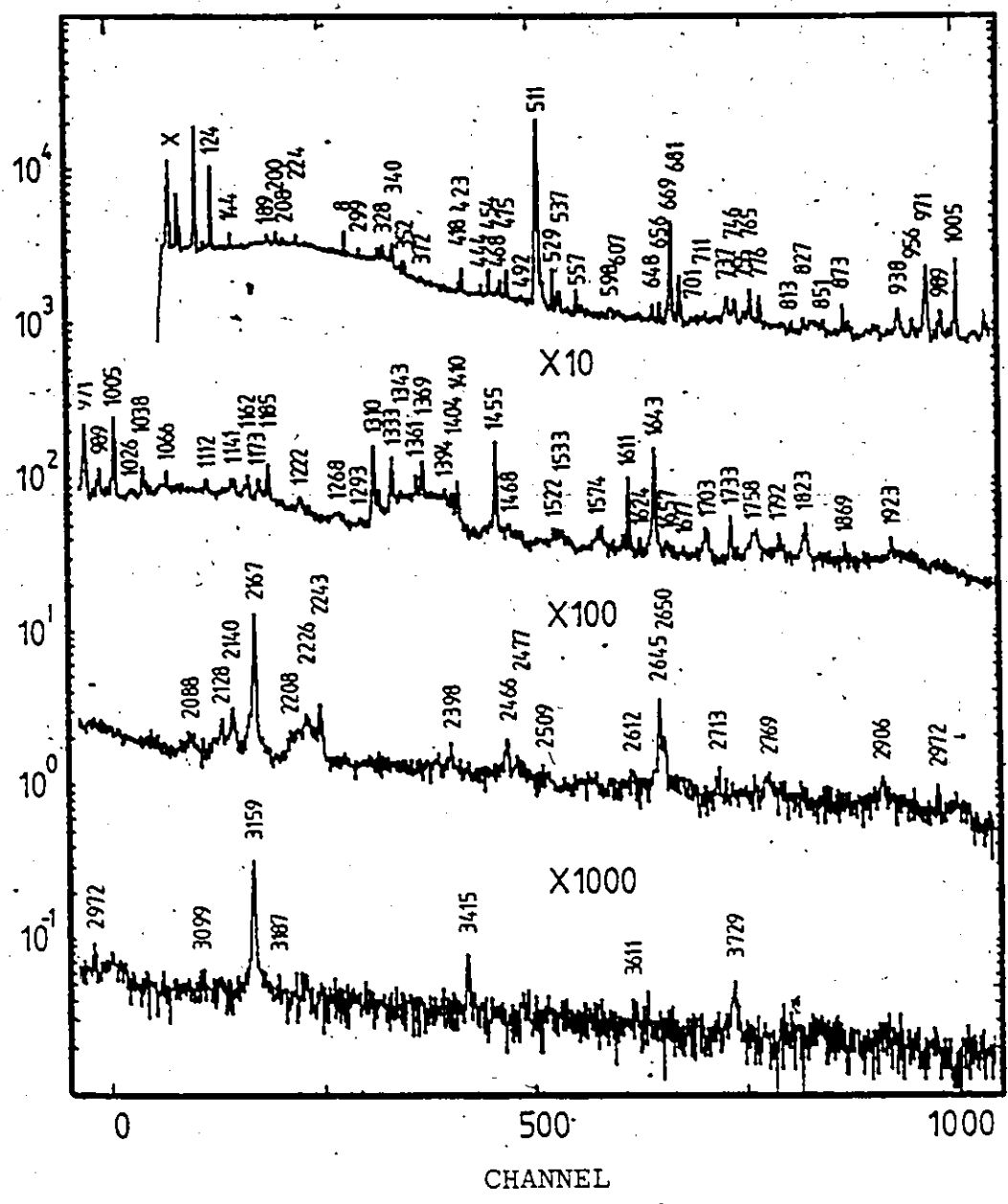


Figure 4.28...  $^{24}\text{Mg}$  on Ca singles spectrum at 66 MeV.

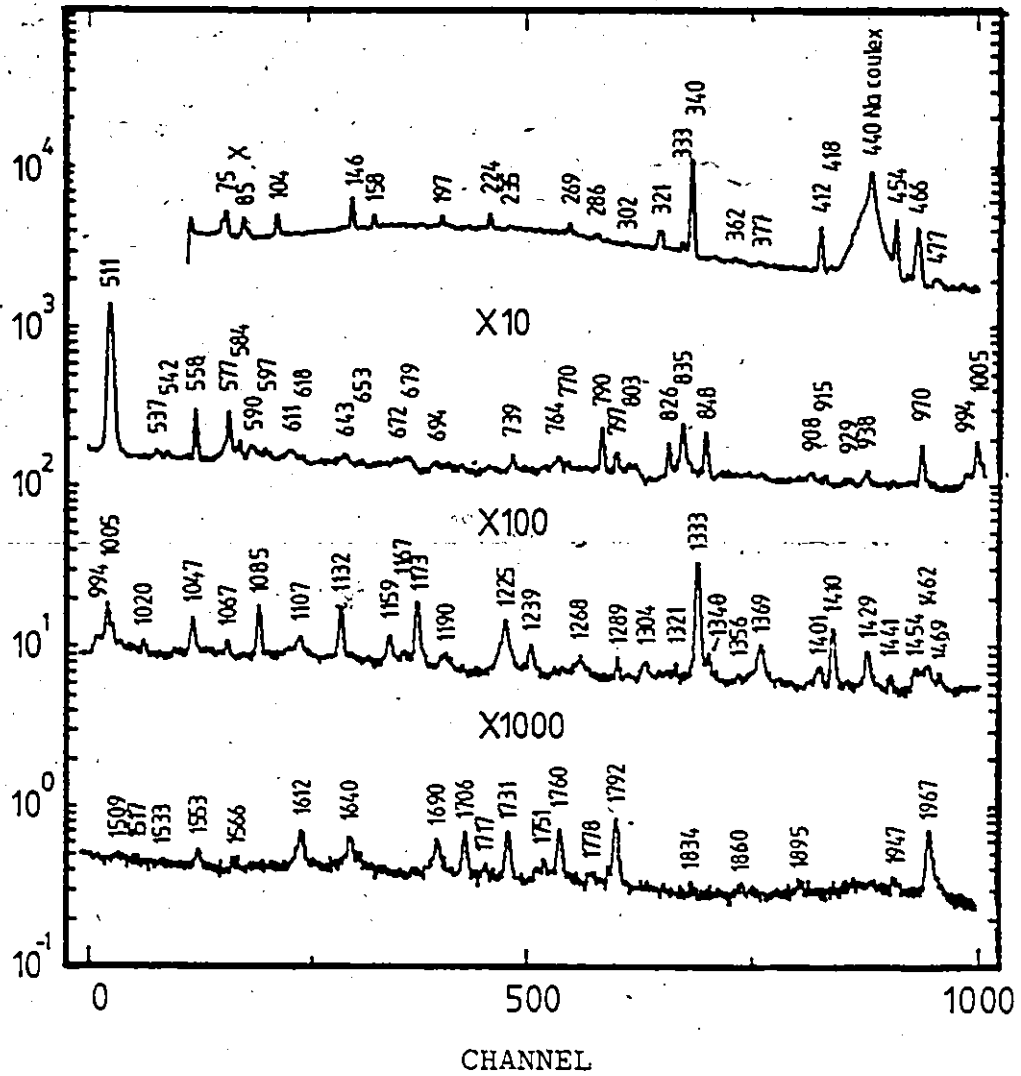


Figure 4.29  $^{23}\text{Na}$  on Ca singles  $\gamma$  spectrum at 70 MeV.

Table 4.8

 $^{61}\text{Zn}$   $\gamma$  energies in other HI reactions

$E_\gamma$	$\text{Ca} + ^{24}\text{Mg}$	$\text{Ca} + ^{23}\text{Na}$	$^{58}\text{Ni} + ^6\text{Li}$	$^{50}\text{Cr} + ^{16}\text{O}$	$^{54}\text{Fe} + ^{10}\text{B}$	$\text{Ca} + ^{24}\text{Mg}$ $\gamma\gamma$
88	x + xray	not	x		(x)+xrays?	x
124	x	seen	x	(x)	x	x
295	(x)		x		(x)	
330	c		(c)		c	
337	c		c		c	
418	x	((?))	x	((?))	x	x
520	c		(x)			
578			x		x + c	
608	x + c?		c		(x)c	
632	c		c		x + c	
646	c		c		c	
755	x		x	((?))	x	x
850	(x + c?)		x(+c)		x + d	
872	x	((?))	x	((?))	x	x
937	xx + c		c		x + c	x
943			c			
984	c?		c		x + c	
996	(x)				x + c	x
1006	c				c	
1078	x		(x)		x + c	x
1141	x		x	((?))	x	x
1240	(?)					
1247	(x)					
1274	(x + c)		x + c		x + c?	
1279						
1362	x(+c)		c		(x) + c	
1403	x		(x)		x	x
1532	xx + c?		x + c		(x)	
1974					(x)	

Table 4.7

Contents of  $^{61}\text{Zn}$  coincidence gates at 66 MeV  $^{24}\text{Mg}$  on Ca

gate (keV)	Contents
88	--
124	(295) 873 (1004) 1076 1141 1404 1534
(295)	--
330	c
337	c
418	--
520	c
(578)	--
(606)	--
632	c
646	c
(756)	--
850	c
873	124 936 1404
937	c (+ 124 873 996 1076 1404)
943	c
984	--
996	(1403)
1006	c
1076	(873) (936) (1403)
1141	124 1531
(1240)	--
(1247)	--
1274	-c
(1279)	--
1362	--
1403	124 873 936 996 1076
1532	c
(1974)	



Table 4.8

Summary of levels from  $\gamma$  work

	a	Li	B	O	Na	Mg
88	x		x			x
124	x	x	x	(x)		x
478	x	x	x			x
755	x	x	x			x
938	x	x	x			?
996	x	x	x			x
1265	x	x	x			x
1361	x	((x))	(x)			x
1402	x					
1659	x					x
2002	x					x
2099	x		(x)			
2270	x	(x)	(x)			(x)
2400	x	x	x			x
2797	x					x
3337	x	(x)	x			x
4413		(x)	x			x

Multiplicity filter measurements were made using the  $^{24}\text{Mg}$  on Ca reaction at 66 and 85 MeV, and the  $^{23}\text{Na}$  on Ca reaction at 70 MeV. Only one new transition belonging to  $^{61}\text{Zn}$  was found, namely the 1076 keV line feeding the 937 - 1403 - 873 - 123 keV  $\gamma$  cascade. The ( $^{24}\text{Mg}, 2\text{pn}$ ) gates are summarized in Table 4.7. Examinations of the  $\gamma$  singles and projections taken between  $10^\circ$  and  $105^\circ$  again failed to reveal any convincing evidence for doppler shifts of the  $^{61}\text{Zn}$  lines.

The mechanically chopped beam experiments incorporating the  $^{24}\text{Mg}$  beam on (natural) calcium targets at 66, 72.2 and 81.7 MeV failed to reveal any activity from the decay of  $^{61}\text{Ga}$  to  $^{61}\text{Zn}$ , though there was ample evidence for decays of  $^{61}\text{Zn}$  to  $^{61}\text{Cu}$  to  $^{61}\text{Ni}$ . The short-lived  $^{61}\text{Ga}$  activity was still overwhelmed by the activities from zinc, copper and nickel isotopes.

Level schemes based upon the results of the experiments performed in the project are presented in Figure 4.30, along with the experimental level schemes of Smith et al (1982), Woods et al (1978), Weber et al. (1979). The experimental levels are compared with the theoretical shell model calculations of van Hienen et al. (1976) in Figure 4.31. Systematics of the lower lying levels across the odd  $N=31$  isotones and  $Z=30$  isotopes may be viewed in Figure 4.32. (Notably, the single particle positive parity  $g_{9/2}$

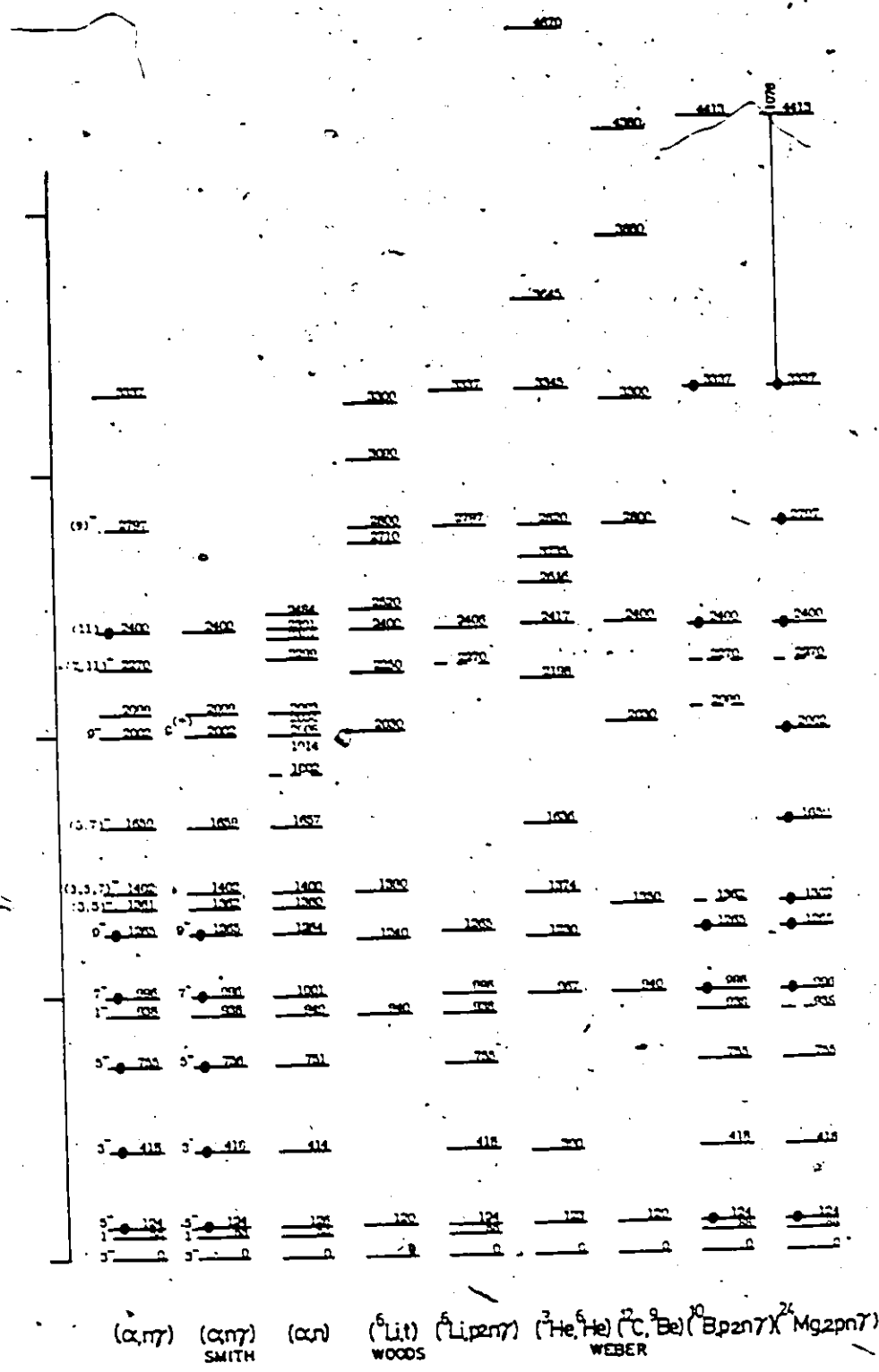


Figure 4.30. Summary of experimental  ${}^{61}\text{Zn}$  level schemes from present work and elsewhere.

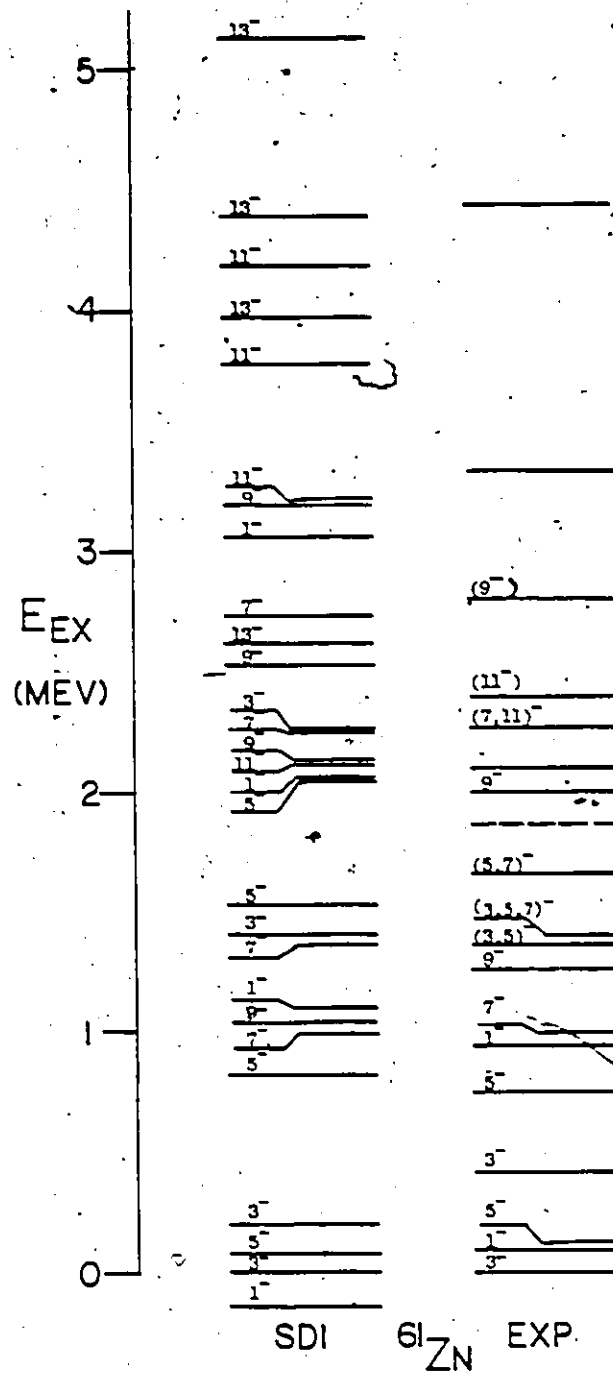


Figure 4.31. Comparison of experimental  $^{61}\text{Zn}$  level schemes with SDI shell model of van Kienen et al.

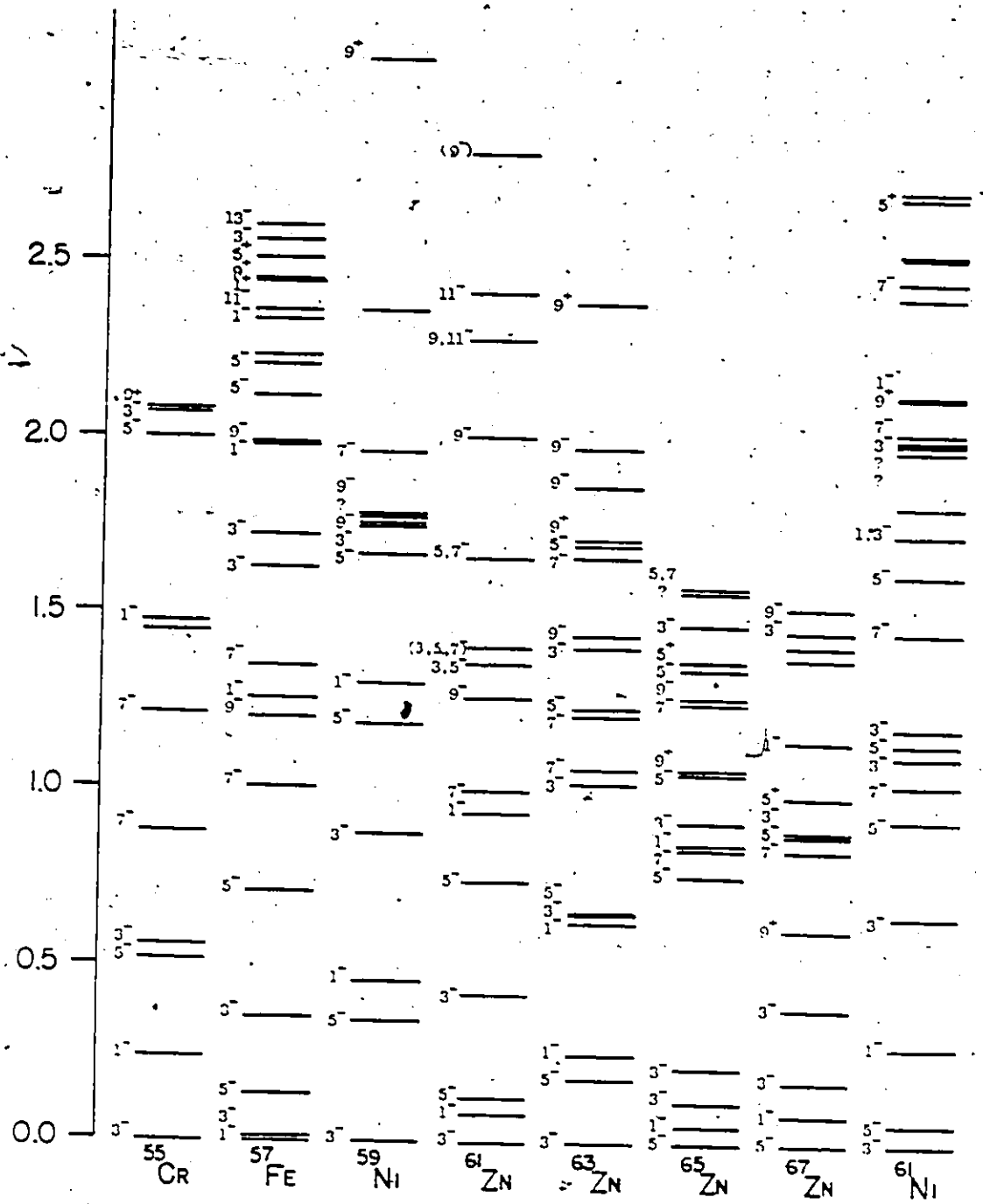


Figure 4.32. Odd-A systematics for N=31 isotones and Z=30 isotopes near  $^{61}\text{Zn}$ .

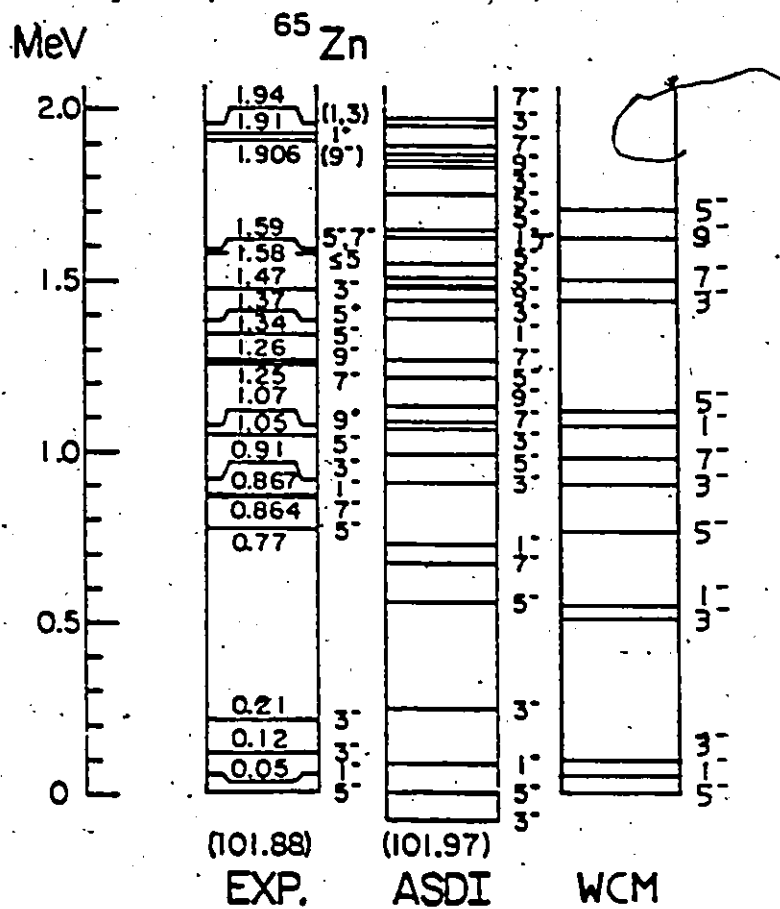


Figure 4.33. WCM (Weidinger et al. (1970)) and experimental level scheme for  $^{65}\text{Zn}$ . Also shown is a shell model (SM) calculation for  $^{65}\text{Zn}$  (from van Hienen et al. (1976)).

and  $d_{5/2}$  states are predicted to occur near 2.5 MeV based upon extrapolation of the odd-zinc states.)

Agreement between the various results is generally consistent when resolution, ranges and statistics are considered. Comparison with the work of Smith et al. (1982) is good, with a few discrepancies appearing in intensities (the 88 and 124 keV  $\gamma$  rays lie in a non linear non exponential region in the large Ge(Li) spectra so great care must be taken in calculating the efficiency in this region otherwise one might end up with "negative" top feeding!), identification and placement of some  $\gamma$  rays (five have been found to be actually doublets: 937/938, 1005/1007, 1239/1242, 1403/1404, 1531/1534 and several spin assignments). The heavy ion reactions are expected to populate predominantly the higher spin states, but the  $\gamma$  work may still uncover some of the intermediate levels due to  $\gamma$  feeding. Overall the comparison with theory, particularly below 2 MeV excitation, is good, especially when it is remembered that only copper and nickel data were used to fit the MSDI shell model parameters. Below 1 MeV the number and spins of states are predicted correctly, but the order, notably the three lowest states, is slightly in error. It is conceivable that only slight adjustments to the configuration mixing and potential parameters need to be made to reproduce the correct sequence and spacings.

As a crude comparison, the weak coupling model calculation for  $^{65}\text{Zn}$  of Weidinger et al. (1970) is shown in Figure 4.33 along with a shell model calculation and the low lying experimental levels of  $^{65}\text{Zn}$ , as well as the SDI shell model levels for  $^{65}\text{Zn}$  of van Hienen et al. (1976). In the case of  $^{61}\text{Zn}$ , one would expect exactly the same number of levels and spins but with slightly different orderings. In fact, the model for  $^{61}\text{Zn}$  should be even more successful in the limited WCM because  $^{60}\text{Zn}$  should provide a better (vibrational) core and more "room" in f2p space is available for the valence neutron. (A WCM calculation for  $^{61}\text{Zn}$  is not as yet available at time of writing.)

Discussion of individual levels will follow below. To avoid needless repetition, relevant key features from theory and systematics will be mentioned as required in the same subsections as the experimental arguments rather than separately at the end, seeing that the most convenient comparisons were already made visually in Figures 4.30 to 4.32. However, it must be emphasized that theoretical predictions did not prejudice arguments leading to any spin and parity assignments.

## 4.2 Discussion of Levels

### 4.2.1 The 88 and 124 keV levels

In addition to the shell model predictions, systematics and intensities, data from the angular distributions



and lifetime measurements support the spin and parity assignments of  $1/2^-$  and  $5/2^-$  for the 88 and 124 keV levels, respectively. The 88 keV transition is definitely isotropic (where almost all other lines exhibit a large degree of anisotropy), indicative of  $J_i = 1/2$ . The negative parity assignment is partly based upon systematics, and is consistent with the weak 330 and 850 keV transitions feeding the 88 keV level. The lifetime limits rule out any other spin/parity hypothesis that gives unacceptably large E2/M1 mixing ratios.

On the basis of the angular distributions alone, a spin/parity hypothesis of  $3/2^-$  cannot be ruled out for the 123 keV level. However, the two possible solutions for the mixing ratio are both unacceptably large. One Weisskopf unit for a 123 keV E2 transition implies a lifetime of the order of  $10^{-6}$  second. Since 300 W.u. represents the (extreme) recommended upper limit (RUL) for E2 transitions in this mass region (Endt (1979)), the lifetime would then be expected to (well) exceed several nanoseconds, which is contra-indicated by the lifetime results. The 996 keV line feeding the  $3/2^-$  ground state has a characteristic "stretched E2" ( $L = |\Delta J| = 2$ ;  $\pi_i \times \pi_f = +1$ ) distribution whereas the 873 keV line feeding the 123 keV level from the same 996 keV level is definitely not a stretched E2. The sign of the  $a_2$  coefficient for the 123 keV distribution is the same as for the 756 keV distribution (spin  $5/2^-$ ) and

opposite to that of the 418 keV distribution (spin  $3/2^-$ ). Unfortunately, the singles relative yield curve of the 123 keV line does not support either the  $3/2^-$  or even  $5/2^-$  hypotheses; rather it is much steeper, indicative of a  $7/2$  or  $9/2$  spin. This apparent anomaly may be explained by the large degree of top feeding experienced by this level.

#### 4.2.2 The 418 keV level

On the basis of the 418 keV angular distributions alone and under various realistic assumptions of populations ( $\sigma = 0$ , or  $\sigma =$  "small", or  $P(3/2) =$  "small"),  $3/2^-$  is definitely the preferred value for initial spin and parity. This is also consistent with the 418 keV relative yield curve, the branching ratios to the ground, 88, and 123 keV levels via 418, 330 and 295 lines, and the weakness of the top feeding 337, 520, 578, 944 and 984 keV transitions (decays to the ground state are favoured over those to the 418 keV state because of the energy enhancement of the transition rates, other factors being equal). Normally for  $3/2$  states there are two equivalent values of mixing ratio obtained from the  $\chi^2$  vs  $\arctan \delta$  analysis. Here the larger (absolute) value ( $-84^\circ$ ) should be rejected on the basis of the lack of observed electronic lifetimes (although only 1 W.u. for 418 keV is equivalent to 3 nsec), and that such an extreme value would be very unusual, if not unrealistic. The angular distributions of the 295 and 330 keV lines are

unreliable, but 418 keV level is nevertheless assigned a spin and parity of  $3/2^-$ .

#### 4.2.3 The 755 keV level

The 755 keV level decays predominantly to the ground state, but also branches to the 123 and 418 keV states via the weak 632 and 338 keV transitions. The angular distribution of the 756 keV line under various realistic population assumptions strongly support the  $5/2^-$  spin and parity hypotheses. When the  $B_k$  statistical tensors are adjusted to incorporate the weighted top and side feeding components, the  $\chi^2$  minimum value for the n- $\gamma$  distributions under  $5/2^-$  assumption plummets even further (see Figures 4.20 to 4.22). The yield curve slope is also consistent with the  $5/2^-$  hypothesis, being steeper than the 418 keV line ( $3/2^-$ ) and shallower than the 873 keV line ( $7/2^-$ ). The 632 keV line is too weak to provide a reliable angular distribution, while the 337 keV line is contaminated (heavily in the 20 MeV run by the 339 keV line from  $^{59}\text{Ni}$ , less so for the 15 MeV run, but strong 338 and 340 keV lines from  $^{61}\text{Cu}$  may partially intrude into the n- $\gamma$  spectra) so its angular distribution is also not reliable (although it does appear consistent with  $5/2^- \rightarrow 3/2^-$  for both  $^{59}\text{Ni}$  and  $^{61}\text{Zn}$ ). The 755 keV level is therefore assigned a spin and parity of  $5/2^-$ . From the branching ratios of levels feeding both the 124 and 755 keV levels, it is evident that the wavefunctions for the 755 keV

level are already becoming somewhat dissimilar to those of the 124 keV level.

#### 4.2.4 The 938 keV level

The 938 keV level deexcites by 938, 850 and 520 keV transitions to the 0, 88 and 418 keV states respectively. Exhaustion of the nearby unattributed theoretical states suggests that this level is perhaps the second  $J = 1/2^-$  state. However, a 937 keV line is also seen feeding the 1404 - 873 - 123 keV cascade and exhibits some degree of anisotropy. It is also contaminated in singles by the stronger 934 keV line of  $^{61}\text{Cu}$ . For the 20 MeV  $n\gamma$  distribution, the strong intrusion of the 934 keV line into the  $n\gamma$  spectrum poses a problem, coupled with poor statistics, resolution and density of nearby lines, making unfolding and subsequent analysis of the distribution unreliable. The  $n\gamma$  yield curve of the 938 keV line, after unfolding by the centroid shift method, is also consistent with the spin 1/2 hypothesis. On the other hand, the 15 MeV  $n\gamma$  angular distributions for both the 937 and 938 keV lines still exhibit some degree of anti-correlation after the same unfolding method, indicating that some of the local energy calibrations for the detector array are not entirely correct. (Line shape unfolding is useless as the separation of the two lines is much less than the FWHM of the detectors at 1 MeV. For the 938 keV centroid shift unfolded distribution

as it stands, acceptable fits are obtained by  $1/2^-$ ,  $3/2^-$  and  $5/2^-$  hypotheses. Therefore the 938 keV  $\gamma$  angular distribution can not be invoked to provide a strong argument in favour of the  $1/2^-$  hypothesis. The 520 and 850 keV distributions do not yield unique fits for the spin hypotheses  $1/2^-$ ,  $3/2^-$  or  $5/2^-$ : all are equally acceptable (with one exception: the  $5/2^- + 3/2^-$  hypothesis for 520 keV yields a very low  $\chi^2$  but at an unacceptably large mixing ratio ( $82^\circ$ )). The yield curve for the 520 keV transition is consistent with the  $1/2^-$  hypothesis (though it suffers from poor statistics owing in part to the large effective background from the proximity of the 511 keV positron annihilation radiation), both in shape and magnitude (states of extreme spin are expected to be less populated than for intermediate spins). The 850 keV line is also seen in  $^{61}\text{Cu}$ , so it cannot be used in singles. The 850 keV branch to the 88 keV level puts an upper limit of  $5/2^-$  on the spin of the 938 keV state; however no branch is observed to populate the  $5/2^- - 123$  keV state, which is more consistent with a spin  $1/2^-$  hypothesis. Therefore a spin and parity of  $(1/2^-)$  is assigned to the 938 keV level. (The brackets around the spin and/or parity indicate an uncertain assignment, or one based on the so-called "weak" arguments.)

#### 4.2.5 The 996 keV level

The 996 keV level deexcites to the 0, 124 and 418 keV levels via 996, 873 and 578 keV transitions. It is also top fed by the 2001, 2270 and 2400 keV levels via 1007, 1274 and 1404 keV  $\gamma$  transitions. As mentioned previously, the 996 keV angular distribution ( $n\gamma$  at 15 MeV only; the others appear to be contaminated by  $n\gamma$  events from the tantalum beam dump, shielding and (upstream) stainless steel walls) is consistent with the  $J_1^\pi = 7/2^-$  hypothesis. Acceptable fits for the 873 keV distribution are obtained for  $3/2^-$  and  $7/2^-$  assumptions, the former of which may be rejected on the grounds of the definite non zero  $a_4$  coefficient of the 996 keV distribution. The 578 keV distribution gives acceptable fits for  $3/2^-$ ,  $5/2^-$  and  $7/2^-$  hypotheses, but of course suffers from much poorer statistics. When the top feeding contributions are estimated for the  $n\gamma$  distributions, the  $\chi^2$  minimum values plummet even further. Of the two equivalent arctan  $\delta$  solutions,  $13^\circ$  and  $61^\circ$ , to the 873 keV  $n\gamma$  distribution at 15 MeV, only the latter solution improves significantly and is consistent with the value found by Smith et al. (1982). (This is further evidence that the gaussian population assumption is not valid when there exist appreciable top feeding components). On the basis of the 873 and 996 keV yield curves,  $7/2^-$  is also favoured. Thus the 996 keV level is assigned a spin and parity of  $7/2^-$ .

#### 4.2.6 The 1265 keV level

The 1265 keV level deexcites by emitting a 1141 keV  $\gamma$  ray to the 124 keV level. It is populated mostly by side feeding with a small amount of top feeding from the 2796 keV level via the 1532 keV transition and an even smaller amount by the 1005 keV line from the 2270 keV level (note that this line is overwhelmed, even in  $n\gamma$  coincidence, by the 1007 keV transition from the 2002 to 996 keV levels). Qualitatively, the 1141 keV distributions at 15 MeV exhibit a stretched  $E_2$  character. For reasonable values of gaussian or  $m = 1/2, 3/2$  only populations,  $\chi^2$  minima for  $5/2^-$  and  $9/2^-$  assumptions are obtained. On the basis of the yield curve gradient and the lack of any observed transition to the ground state (which should then be much stronger than to the  $5/2^- - 123$  keV state, if the 755 keV line is any indication), the  $5/2^-$  hypothesis may be ruled out. Positive parity may be ruled out on the basis of ( $l=3/l=2$ ) mixing ratios as well as systematics and shell model. Unfortunately the 20 MeV  $n\gamma$  distribution presents an anomaly in that the  $a_4$  coefficient is much too small ( $-0.03 \pm .08$ ). (Generally the 20 MeV data are not as reliable as the 15 MeV data because of statistics, backgrounds, and detector responses.)

The 1265 keV level is therefore assigned a spin and parity of  $9/2^-$ .

#### 4.2.7 The 1361, 1402 and 1659 keV levels

Four transitions, 1362, 1238, 943 and 606 keV, depopulate the 1361 keV level to the 0, 124, 418 and 755 keV levels, respectively. (A 1241 keV  $\gamma$  ray also deexcites the 1658 keV level: discussed below.) Based on these branchings, an upper limit of  $7/2^-$  may be placed on the spin and parity of the 1361 keV level. The 1361 keV yield curve indicates a preference for spin  $7/2$ , contradicted by the 15 MeV  $n-\gamma$  angular distributions for which acceptable fits are provided by  $1/2^-$ ,  $3/2^-$  or  $5/2^-$  assumptions for the spin, with a slight preference for  $5/2^-$ . Similarly a slight, though unreliable, preference for  $5/2^-$  is indicated by the 1240 keV distribution, although in reality acceptable fits are obtained for  $1/2^-$  to  $7/2^-$  assumptions. The 943 and 606 keV distributions rule out spin  $1/2^-$ , but contradict each other regarding  $7/2^-$ ; otherwise  $3/2$  and  $5/2$  also provide acceptable fits. Note that the quality of these four distributions, particularly the latter two, is rather poor.

The SDI shell model predicts the spin of the 1361, 1402 and 1659 keV levels to be  $7/2^-$ ,  $3/2^-$  and  $5/2^-$ , but not necessarily in that order as the predictions for energy cannot be trusted to the required degree of accuracy here.

The 1402 keV level deexcites to the 755, 418, 124 and 0 keV levels via 646, 983, 1279 and 1402 keV transitions. The 646 and 984 keV  $\gamma$  rays appearing in singles are heavily contaminated by transitions from  $^{61}\text{Cu}$ ; they may only be



trusted in clean n- $\gamma$  coincidence. The 1402 keV transition  $\gamma$  ray is also contaminated by another, stronger 1404 keV line feeding the 996 keV level in  $^{61}\text{Zn}$  as determined by the 124, 872 and 996 keV gates. Again, the branchings place an upper limit on the spin of  $7/2^-$ . The 646, 983 and 1279 keV n $\gamma$  distributions -- all of poor quality -- cannot rule out any of the  $3/2^-$ ,  $5/2^-$  or  $7/2^-$  spin possibilities (although the 983 keV distribution indicates a strong preference for  $7/2^+$   $3/2^-$  with large  $\lambda=3/\lambda=2$  mixing ratios).

The 1659 keV level deexcites via a 1536 keV  $\gamma$  transition to the 124 keV level and possibly by a weak and contaminated 1241 keV branch to the 418 keV level (as determined from energy sums and shifts, although this is not verified by the coincidence gates). The  $\chi^2$  vs  $\arctan \delta$  distribution for the 1534 keV line at 15 MeV shows no truly sharp minimum, although the  $5/2^+ \rightarrow 5/2^-$  hypothesis is favoured over others at large mixing angles ( $40^\circ$  to  $90^\circ$ ); the  $9/2^+ \rightarrow 5/2^-$  hypothesis, also favoured, may be ruled out on the basis of the 1241 keV branch. (The 1241 keV distribution definitely favours  $7/2^-$  at large mixing angles but is of no value owing to the stronger presence of the 1238 keV line feeding the 123 keV level.) The lack of branching to the ground state may indicate a preference for  $7/2^-$ . The 1533 keV yield curve is not really very useful since it incorporates both 1532 and 1536 keV lines and is situated on the tails of much larger  $^{61}\text{Cu}$  lines.

Spin assignments for the 1361, 1402 and 1659 are therefore  $(3/2, 5/2)^-$ ,  $(3/2, 5/2, 7/2)^-$  and  $(5/2, 7/2)^-$ , respectively.

#### 4.2.8 The 1802, 2034 and 2098 keV levels

The 1802 and 2034 keV levels are seen only weakly in the  $(\alpha, n)$  experiment as levels of  $^{61}\text{Zn}$  (the  $(^{12}\text{C}, ^9\text{Be})$  experiment of Weber et al. (1979) cannot distinguish the 2034 level from the nearby 2003 and 2098 keV levels) and are therefore only tentative.

The 2098 keV level is seen weakly both in the  $(\alpha, n)$  spectrum, as a 1975 keV  $\gamma$  ray feeding the 124 keV level and conceivably as part of an unresolved doublet (or even a triplet) in the  $(^6\text{Li}, t)$  and  $(^{12}\text{C}, ^9\text{Be})$  work. The 1975 keV line is also seen in singles  $(\alpha, n\gamma)$  spectra. (This line may be contaminated as it is also seen in the 12.2 MeV singles spectrum of Sarantites et al (1973), which is below threshold for the 2098 keV level -- unless the reported bombarding energy is incorrect.) Only an upper limit of 9/2 for the spin may be assigned for the 2097 keV level in view of its prompt coincidence as the angular distributions are much too poor to be useful.

#### 4.2.9 The 2003, 2270 and 2796 keV levels

The 2003 keV level deexcites to the 996, 755 and 124 keV levels via 1007, 1248 and (weak) 1880 keV  $\gamma$  transitions.

This state is claimed by Smith et al. (1982) to be a good candidate for the  $9/2^+$  -  $g_{9/2}$  state, based on their  $\gamma$  yield curve, angular distribution and polarization analysis of the 1006 keV line and on systematics of the odd-zinc isotopes. However, their systematics calculations appear too low: if the quadratic trend is maintained, then the  $g_{9/2}$  state should appear at  $2.6 \pm .1$  MeV (fitting error only) and the  $d_{5/2}$  state at  $2.8 \pm .1$  MeV, with the caution that systematics calculations to this accuracy are unwarranted. (The above errors reflect only the standard deviations of the fitting procedure; they do not incorporate any model or systematic errors). Also, the 1007 keV line may suffer from intrusion by the 1003 keV line from inelastic excitation in  $^{58}\text{Ni}$  and from a much weaker 1005 keV line branching from the 2270 keV line in  $^{61}\text{Zn}$ . The 20 MeV distribution of the 1007 keV line, which suffers strongly from the  $^{58}\text{Ni}$  intrusion, prefers a  $7/2^-$  value for spin, but obviously this distribution is not reliable. The much cleaner 15 MeV  $\gamma$  distribution prefers  $9/2$  with mixing angle  $\arctan \delta = 14^\circ$  or  $66^\circ$  and  $3/2^-$  with  $\arctan \delta = -63^\circ$ . The  $3/2^-$  hypothesis may easily be ruled out because of the large  $l=3/l=2$  mixing ratio and also by the 1248 keV distribution which definitely favours  $9/2 - 5/2^-$  with both small ( $8^\circ$ ) and large ( $77^\circ$ ) mixing angles, the latter of which may also be ruled out. ( $5/2^- + 5/2^-$  also provides an acceptable fit but at larger  $\chi^2$  and may be ruled out by the 1007 keV distribution; the 20 MeV distribution

for 1248 keV is too poor in quality to be useful.) It is very doubtful that the 1248 keV transition is indeed E3/M2 as Smith et al. suggest, for one would then definitely expect an E1 transition to the  $7/2^-$  - 996 keV level with a mixing ratio of 0, in contradiction with above, and a greater branching to the  $5/2^-$  - 124 keV level. The spin and parity of the 2002 keV level is therefore assigned as  $9/2^-$ .

The 2270 keV level deexcites to the 996 keV level by emitting a 1274 keV  $\gamma$ -ray in addition to the weak 1006 keV branching to the 1265 keV level mentioned previously. An estimate for the intensity of this branch was calculated by multiplying the 1006 keV  $\gamma$  intensity by the 1006 keV area in the 1141 gate over the sum of the 1006 keV areas in the 1141 and 873 gates, the latter corrected for relative efficiencies and branching ratios. The angular distribution at 15 MeV for the 1274 keV line shows a definite preference for  $7/2^-$  and  $11/2^-$  hypotheses. The  $11/2^-$  hypothesis gives rise to a very large mixing ratio; smaller values of  $\delta$  occur at  $\chi^2$  levels comparable to the remaining hypotheses' levels, which are still below the 0.1% confidence limit. The 20 MeV distribution prefers only the  $7/2^-$  assumption. The 1274 keV yield curve gradient suggests that the spin lies between  $7/2$  and  $11/2$ . If the spin is indeed  $7/2$  then it would appear unusual that no decay to the  $5/2^-$  123 or 756 keV states, or even the  $3/2^-$  ground state, is seen. It should be emphasized that the errors involved are rather large; therefore

only a tentative value of  $(7/2^-, 11/2^-)$  is assigned for the spin and parity of the 2270 keV level.

The 2796 keV level deexcites to the 1265 keV level via a 1532 keV  $\gamma$  transition. The level is seen in the particle work of Woods et al. (1978) and Weber et al. (1979), but appears to have been missed by Smith et al. (1982). No branching to any other states is observed, either in the coincidence data or even in singles. The 15 MeV angular distribution prefers a  $9/2^- \rightarrow 9/2^-$  hypothesis with large mixing angles of  $90^\circ$  (ruled out) and  $54^\circ$ . The  $13/2^- \rightarrow 9/2^-$  hypothesis also gives an acceptable though larger  $\chi^2$ , with a large mixing angle of  $66^\circ$ , but this may be ruled out due to electronic lifetime measurements. The fact that no decays are observed to states of different spin could lend some credence to the hypothesis that this is the  $8_{9/2}$  state, although one would still expect a  $9/2^+ \rightarrow 7/2^-$  branch. However the positive parity is contra-indicated by the definite non zero mixing ratio; furthermore, the shell model still predicts, with less certainty, that there are nearby  $9/2^-$  states, among others. The singles yield curve and distribution cannot provide useful information as the 1536 keV line intrudes somewhat and both lines are situated on the tails of more intense  $^{61}\text{Cu}$  transitions. A value of  $(9/2^-)$  is proposed for the spin and parity of the 2795 keV level.

#### 4.2.10 The 2400, 3337 and 4413 keV levels

The 2400 keV state decays to the 996 keV level by emission of a 1404 keV  $\gamma$ -ray. As mentioned previously, this  $\gamma$  ray also appears as a transition to the ground state from the 1402 keV level. The 2400 keV level is also fed by a 937 keV  $\gamma$  ray from the 3336 keV level. (A similar energy  $\gamma$  ray is also seen in a decay to the ground state.) No other branchings are observed, suggesting a spin greater than  $7/2$  for the 2400 keV level. Singles yield curve measurements of the 1403 keV  $\gamma$  ray are naturally ambiguous; however, the  $n\gamma$  centroid shift unfolded yields suggest a spin near  $1/2$ . The angular distributions at 20 MeV are expected to show much more ( $> 90\%$ ) of the 2400 keV level character than the 1402 keV level, and less so (60%) at 15 MeV as verified by an estimate of the relative contributions by comparing the efficiency corrected areas of the 1403 to 1274 keV  $\gamma$  lines appearing in the 123 keV gates to the 1403 to 1274 keV singles and  $n\gamma$  relative to intensities and by the centroid shift method. The 20 MeV angular distribution does show a stretched E2 shape but the  $x^2$  vs  $\arctan \delta$  plots show no preference between  $11/2^-$  or  $7/2^-$  for the spin of this level, and both have reasonable mixing ratios ( $0^\circ$ ,  $90^\circ$  (ruled out) and  $\{-52^\circ, -2^\circ\}$ , respectively). When the  $U_k$  coefficients are estimated to include the effect of top feeding (assuming that half of the 937 keV intensity feeds the 2400 keV level, and that the spin of the 3337 keV level is  $15/2$ ), the  $x^2$

is reduced by a factor of 3 for the  $11/2^- \rightarrow 7/2^-$  ( $\delta=0$ ) hypothesis but only 30% for the  $7/2^- \rightarrow 7/2^-$  hypothesis. As expected, the 15 MeV distribution remained ambiguous. (Further tests of different assumptions are unwarranted due to the large uncertainties involved in the intensities; although both the 1402 and 2400 keV levels are seen in the  $(\alpha, n)$  particle work, the relative intensities cannot be estimated because of the unknown particle angular distributions and the fact that the measurements are at a very different energy.) A spin and parity of  $(11/2^-)$  is proposed for the 2400 keV level.

Angular distributions of the 937 keV line are not very useful due to intrusions of nearby  $n\gamma$  and  $\bar{n}\gamma$  lines as well as the unresolved  $938 + 0$  keV transition. Again the high spin transition--possibly as high as  $15/2^-$ --is expected to dominate at 20 MeV and less so at 15 MeV  $\alpha$  bombarding energy.

The identity of the 4413 keV level is well established from the  $^{24}\text{Mg}$  on Ca coincidence experiment, as the 1076 keV  $\gamma$  ray depopulating this level is seen in the gates of the 937 - 1404 - (873 - 124)/996 keV cascade. In principle a singles angular distribution has been performed as singles mode data were also acquired from the 5 Ge(Ge(Li)) detector multiplicity filter run, but the overall weakness of the transitions in question does not warrant further analysis of the data.

## CHAPTER 5

### $^{60}\text{Zn}$ : Results and Discussion

#### 5.1 Results and general discussion

There already existed a considerable amount of information about  $^{60}\text{Zn}$  when work began on this part of the project in 1980: ( $\tau, n$ ) neutron time-of-flight (TOF) studies by Evers et al. (1974, 1972), Greenfield et al. (1972), Alford et al. (1975), and Winsborrow et al. (1972), ( $\tau, n\gamma$ )  $n\gamma$  coincidence studies by Kamermans et al. (1974), the heavy ion-particle (HI) transfer reactions ( $^{12}\text{C}, ^{10}\text{Be}$ ) by Weber et al. (1979) and ( $^{16}\text{O}, ^{14}\text{C}$ ) by Pougheon et al. (1972) and  $\beta$  decay studies by Dulfer et al. (1972) and Hoffmann et al. (1969), as well as numerous theoretical studies, as mentioned previously. (Many of these references, both theoretical and experimental, are conveniently summarized in the Nuclear Data Sheets, vol. 28 by Auble (1979).) The main reasons for pursuing further investigations of  $^{60}\text{Zn}$  were to study the weaker states seen in the TOF and/or HI work but missed by Kamermans, (Table 5.1i; the high energy threshold placed on the neutron detector by Kamermans essentially limited the excitation energy to a maximum of just over 4 MeV), to measure any lifetimes by DSAM and electronic techniques, and to discover any higher spin states populated



Table 5.1i.

$^{60}\text{Zn}$   $\gamma$  energies in the  $(\tau, n\gamma)$  reaction

Placed  $\gamma$ 's from work of Kamermans et al.

$E_{\gamma}$	$I_{\gamma}$ (10 MeV) <sup>†</sup>
1004.2 $\pm$ .5	100
1189.4 $\pm$ .5	17 $\pm$ 3
2006.8 $\pm$ 1.0	4 $\pm$ 2
2500.1 $\pm$ 1.0	23 $\pm$ 4

<sup>†</sup> relative intensity in coincidence with  
 $E(n) > 3600$  keV

Table 5.111

 $^{60}\text{Zn}$   $\gamma$  energies in the ( $\tau, n\gamma$ ) reactionPlaced  $\gamma$ 's from present work

$E_\gamma$	I(8 MeV)	I(12 MeV)	Comments (I's based on $90^\circ$ n $\gamma$ coincidence)
462	1 $\pm$ 1	1 $\pm$ 1	contaminated by $^{59}\text{Cu}$
690	—	1 $\pm$ 1	
713	—	—	
1003.02 $\pm$ 1.4	$\pm 100 \pm 5$ (c)	$\pm 100 \pm 5$	possible breakthrough by 1004 keV from ( $\tau, \tau'$ ) $^{58}\text{Ni}$
1188.22 $\pm$ 1.4	17 $\pm$ 2	34 $\pm$ 3	contaminated by nearby $\gamma$ 's in singles (but no breakthrough in tight n $\gamma$ coin)
1308.0 $\pm$ 1.4	—	3 $\pm$ 1	
1403.6 $\pm$ 2.5	2 $\pm$ 1	4 $\pm$ 2	contaminated by $^{59}\text{Cu}$ at 12 MeV; I estimated by centroid shift
1531.77 $\pm$ 1.65	3 $\pm$ 1	12 $\pm$ 2	not $^{59}\text{Cu}$ because no other BR seen
1724	—	—	
1779.81 $\pm$ 1.63	10 $\pm$ 2	2 $\pm$ 2	
1827.21 $\pm$ 1.30	—	10 $\pm$ 2	
2007.83 $\pm$ 1.61	7 $\pm$ 2	5 $\pm$ 2	
2031.44 $\pm$ 1.99	—	4 $\pm$ 2	not $^{59}\text{Cu}$ , because no other BR seen
2063.21 $\pm$ 1.92	—	6 $\pm$ 2	
2157.75 $\pm$ 1.85	9 $\pm$ 2	5 $\pm$ 2	cont. by $^{59}\text{Ni}$ in singles (no breakthrough in tight n $\gamma$ coin)
2440.3 $\pm$ 1.6	—	6 $\pm$ 3	
2505.89 $\pm$ 2.20	23 $\pm$ 2	25 $\pm$ 3	
2582.4 $\pm$ 1.2	—	7 $\pm$ 3	cont. by nearby $\gamma$ in singles
2622.55 $\pm$ 1.73	10 $\pm$ 2	2 $\pm$ 2	
2808.3 $\pm$ 1.3	—	5 $\pm$ 2	
2969.6 $\pm$ 1.0	9 $\pm$ 2	2 $\pm$ 2	
3029.2 $\pm$ 2.2	3 $\pm$ 2	3 $\pm$ 3	
3128.6 $\pm$ 1.4	—	5 $\pm$ 3	cont. in singles by $^{59}\text{Cu}$ , $^{60}\text{Ni}$ but no BR seen in n $\gamma$ coin.
3399.1 $\pm$ 2.1	5 $\pm$ 2	4 $\pm$ 3	
3545.5 $\pm$ 1.6	—	7 $\pm$ 3	
3971.31 $\pm$ 1.54	21 $\pm$ 2	12 $\pm$ 2	
3989.9 $\pm$ 2.1	—	4 $\pm$ 3	
4333	—	6 $\pm$ 4	
4496.8 $\pm$ 6.0	—	3 $\pm$ 3	

\* fitted energy from level differences

Table 5.1111

 $^{60}\text{Zn}$   $\gamma$  energies in the ( $\tau, n\gamma$ ) reactionUnplaced  $\gamma$ 's from present work

$E_\gamma$	I(8 MeV)	I(12 MeV)	$E_\gamma$	I 8 MeV	I 12 MeV
473.81 $\pm$ .74		3 $\pm$ 1			
1152.34 $\pm$ .50	--	7 $\pm$ 1	4039.8 $\pm$ 3.2	--	4 $\pm$ 4
1210.58 $\pm$ .66	--	4 $\pm$ 1	4079.9 $\pm$ 1.9	--	5 $\pm$ 3
1369.64 $\pm$ .62	9 $\pm$ 1	--	4179.7 $\pm$ 1.7	4 $\pm$ 1	--
1500.85 $\pm$ .96		4 $\pm$ 2			
1555.71 $\pm$ .22	6 $\pm$ 1	11 $\pm$ 2			
1596.09 $\pm$ .57	--	8 $\pm$ 2	4952.5 $\pm$ 5.6	1 $\pm$ 1	--
1779.81 $\pm$ .63	10 $\pm$ 2	--			
1920.4 $\pm$ 6.4	1 $\pm$ 1	--			
1950.57 $\pm$ .63	2 $\pm$ 1	--			
2326.9 $\pm$ 1.2	--	4 $\pm$ 2			
2557.01 $\pm$ .25	12 $\pm$ 2	6 $\pm$ 3			
2779.6 $\pm$ 2.5	5 $\pm$ 2	--			
3115.6 $\pm$ 1.6	--	6 $\pm$ 3			
3462.5 $\pm$ 1.0		7 $\pm$ 4			
3588.1 $\pm$ 5.0	2 $\pm$ 2	--			

by (HI,xnpy) reactions. Furthermore, the shell models predicted a higher density of levels above 3 MeV excitation than has been to date observed experimentally.

Seven magnetic tapes of three parameter ( $E_{\gamma 1}, E_{\gamma 2}, TAC$ ) address recorded events were collected during irradiation of a  $2 \text{ mg/cm}^2$  self-supporting  $^{58}\text{Ni}$  target in the tantalum lined chamber by a 12 MeV  $^3\text{He}$  beam. This energy was chosen because the  $^{60}\text{Zn}$  yield was anticipated to be a maximum there; a preliminary singles yield with energy curve was not very useful as the 1003 and 1188 keV lines -- the two strongest -- are heavily contaminated by  $^{58}\text{Ni}$  inelastic and  $^{59}\text{Ni}$ ,  $^{59}\text{Cu}$  and other sources. A projection spectrum is shown in Figure 5.1. For comparison, a singles spectrum taken under similar conditions is displayed in Figure 5.2. On the whole, the singles  $\gamma$  spectra are dominated by  $^{59,60}\text{Cu}$  and  $^{57,58,59}\text{Ni}$  events, as expected. Coincidences of one of the  $\gamma$  detectors with the neutron detector were collected in the gated singles mode as shown in Figure 5.3. Because of the problem associated with too many events from the beam dump and linings, apertures etc. ( $^3\text{He}$  on tantalum, surface oxides and any trace impurities), a  $120 \text{ mg/cm}^2$   $^{58}\text{Ni}$  target -- sufficiently thick to stop the beam, yet thin enough so that self absorption of low energy  $\gamma$ -rays of interest could be neglected -- was used for the n- $\gamma$  angular distribution experiment. Coincident n $\gamma$ ,  $\bar{n}\gamma$  and background n $\gamma$  events from four Ge/Ge(Li) detectors at  $90^\circ$ ,  $60^\circ$ ,  $45^\circ$  and  $165^\circ$  were

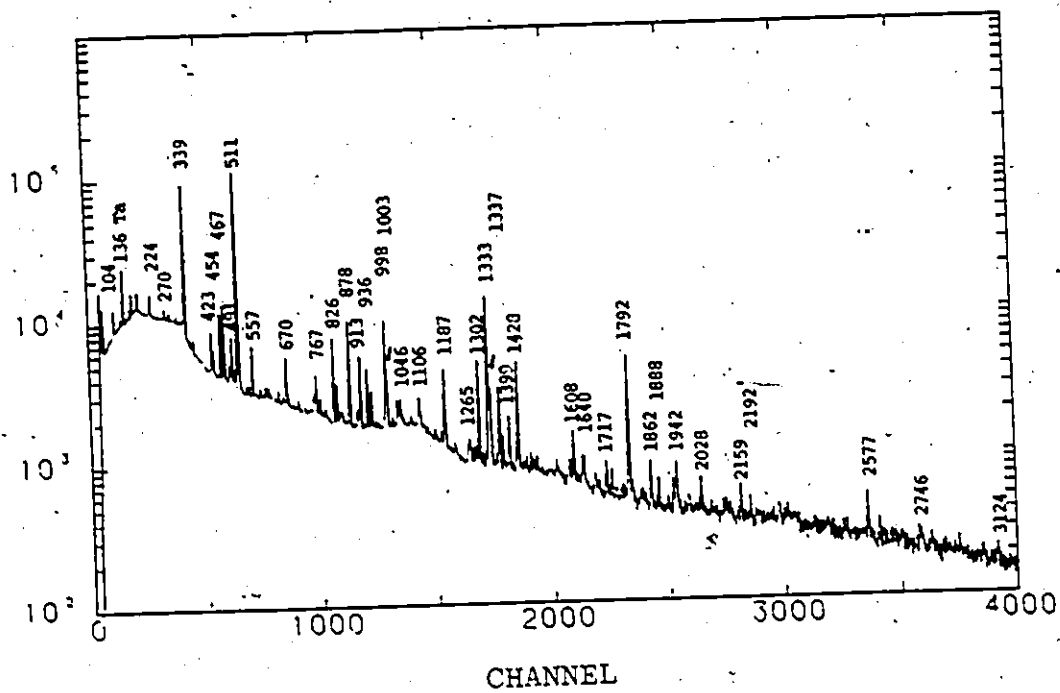


Figure 5.1.  $^{58}\text{Ni}(\tau, n\gamma)^{60}\text{Zn}$   $\gamma$ - $\gamma$  projections  
at  $E_{\tau} = 12$  MeV.

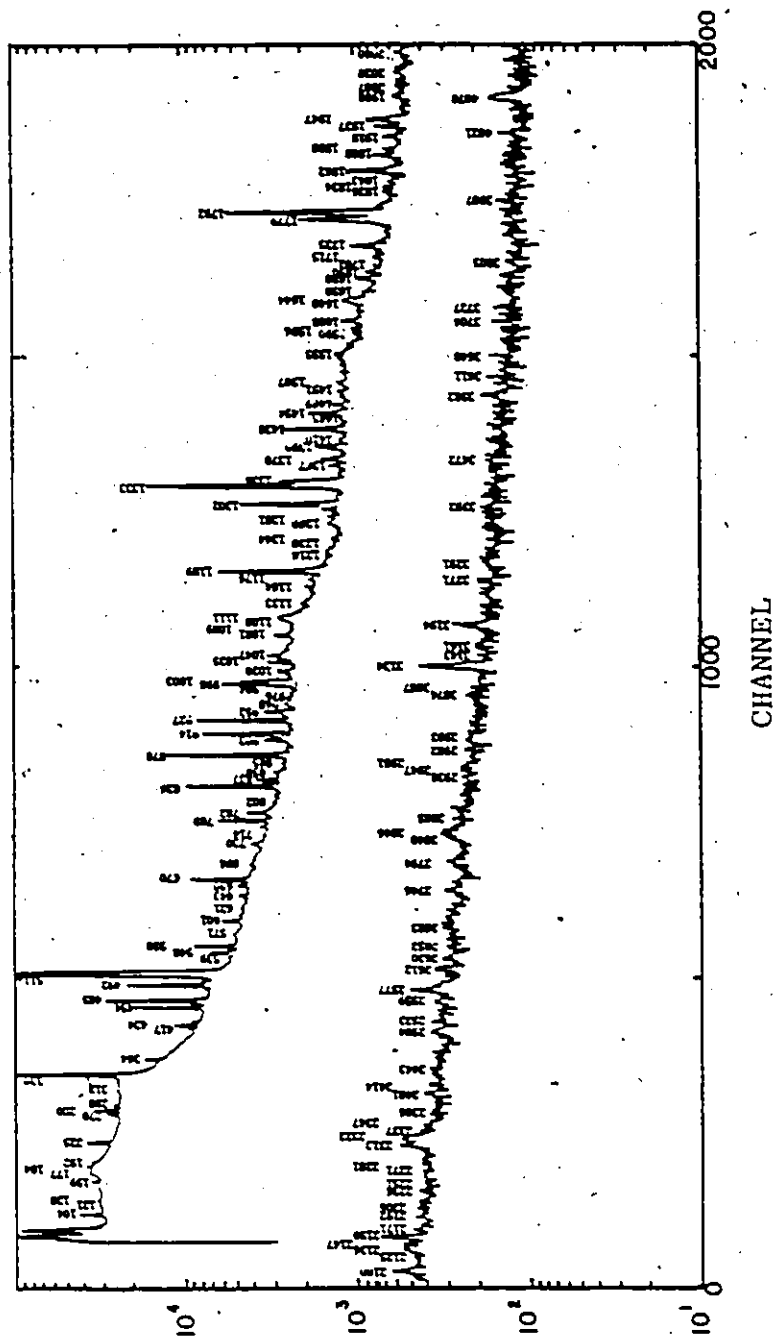


Figure 5.2.  $\gamma$  singles spectrum at  $E_{\gamma} = 12$  MeV.

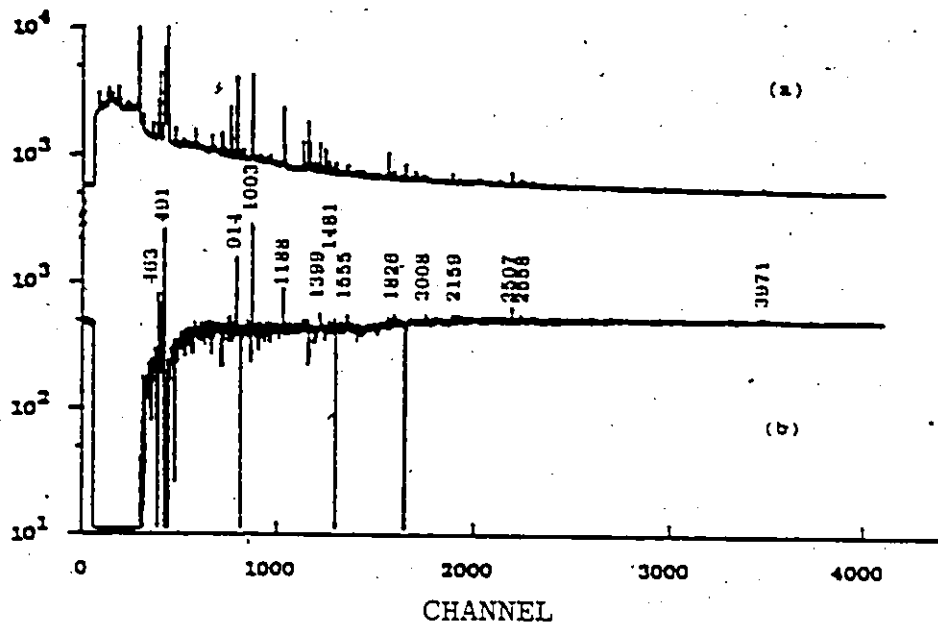


Figure 5.3.  $90^\circ$  n- $\gamma$  coincidence spectrum at  $E_\gamma = 12$  MeV illustrating crude compensation for intruding  $\bar{n}\gamma$  events:

- Initial  $^{60}\text{Zn}$  n $\gamma$  spectrum +500 counts/channel,
- Same but corrected for  $\bar{n}\gamma$  and background n $\gamma$  events using separately collected spectra. The normalization factor for the  $\bar{n}\gamma$  spectrum was determined by averaging the relative intensities of known  $\bar{n}\gamma$  intrusions appearing in the n $\gamma$  spectrum to the  $\bar{n}\gamma$  spectrum. Because there is a non-linear dependence with energy and multiplicity across the nPSA spectrum, some  $\bar{n}\gamma$  peaks appear as over compensated in the net spectrum.

recorded in gated singles mode. The detectors were normalized using the residual  $^{60}\text{Cu}$  beam-off activities, as in Figure 5.4. (Actually, three more detectors were used in the experiment but their data could not be incorporated: two suffered from preamp breakdowns; the third's amplifier malfunctioned partway through the experiment and had to be replaced, but the normalization measurement still gave inconsistent results.)

The  $n\gamma$  spectra themselves suffer from  $p\gamma$  and  $\bar{n}\gamma$  intrusions, even after the latter had been partially corrected for. (One way to attenuate the  $p\gamma$  channel is to increase the neutron detector's energy threshold, but at the expense of rejecting true  $n\gamma$  events.) It was therefore decided to obtain a clean  $n\gamma$  spectrum at 12 MeV (Figure 5.7) by address recording all the pertinent parameters ( $E_\gamma$ ,  $n\text{PSA}$ ,  $n\text{PHA}$ ,  $n\gamma\text{TAC}$ ) and again at 8 MeV (Figure 5.8) in order to suppress the  $p\gamma$  channel. Use of the gold lined target chamber and gold beam dump succeeded in attenuating the  $n\gamma$  events not associated with the target itself. All the  $n\gamma$  spectra were closely scrutinized to determine which  $\gamma$  rays (or sometimes which fractions!) indeed belonged to  $^{60}\text{Zn}$ , with greatest weighting given to the two clean  $n\gamma$  spectra. These  $\gamma$  rays are summarized in Table 5.1, along with those reported by Kamermans et al. Gated spectra for the 1003 and 1188 keV windows are displayed in Figures 5.5 and 5.6. Contents of the  $^{60}\text{Zn}$  gates are summarized in Table 5.2. The



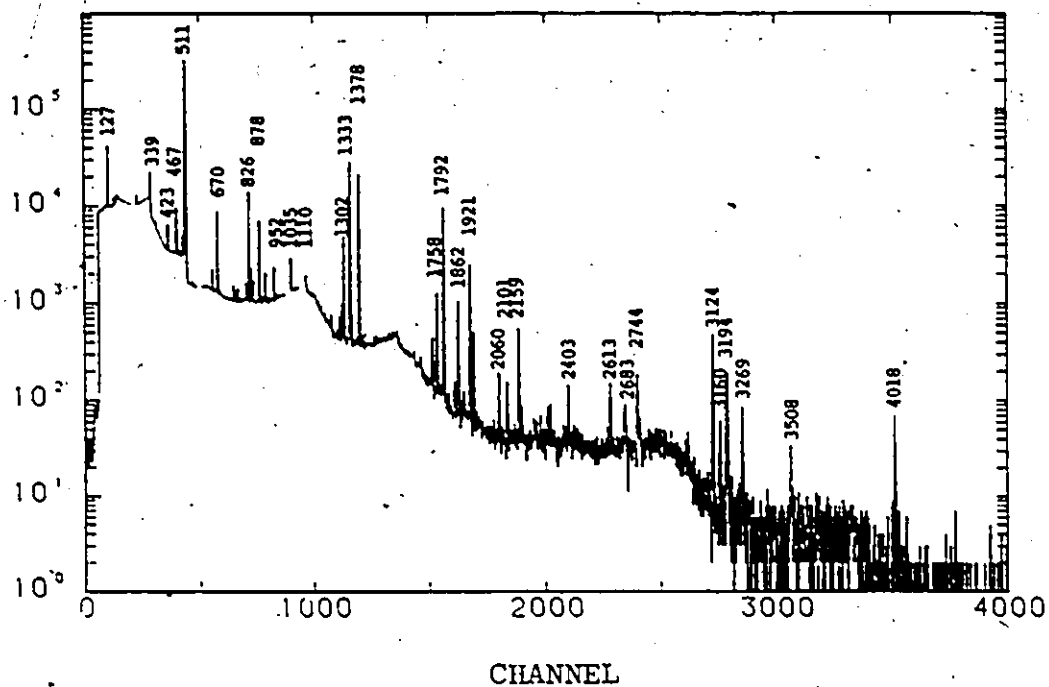


Figure 5.4. Typical beam off  $\gamma$  spectrum following 12 MeV  $\tau$  irradiation of  $^{58}\text{Ni}$ .

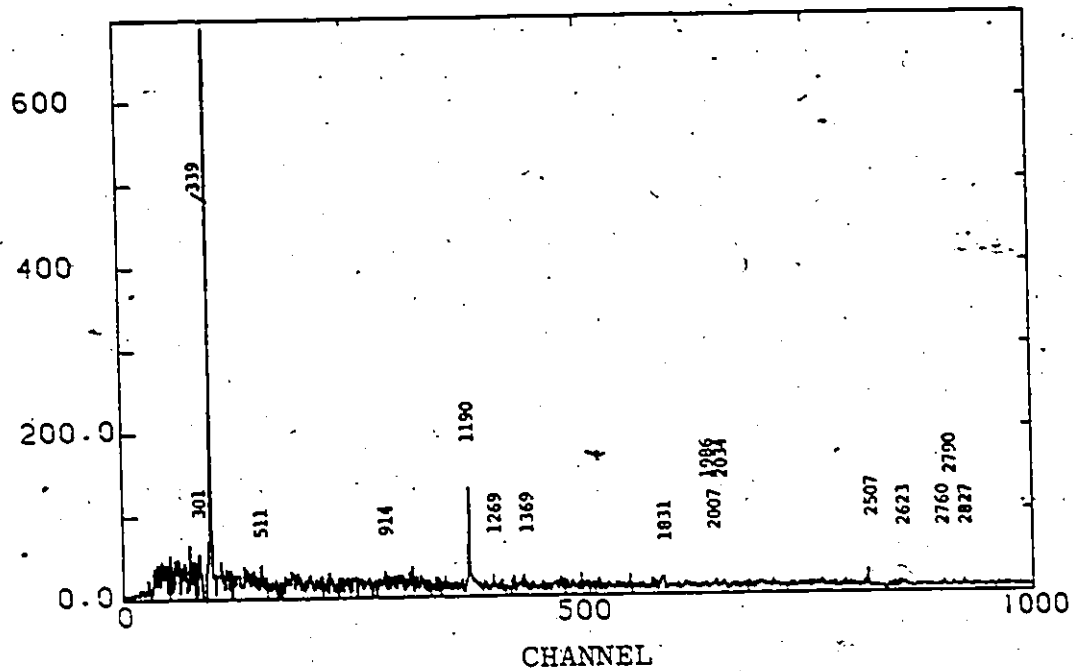


Figure 5.5 1003 keV gate at  $E_c = 12$  MeV.

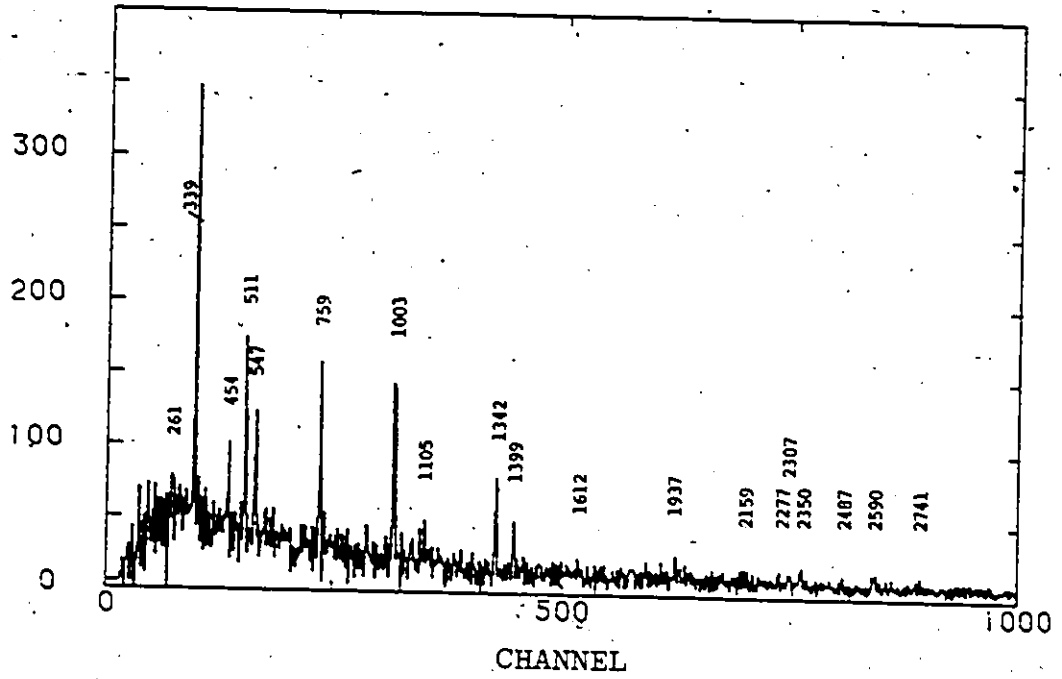


Figure 5.6. 1189 keV at  $E_{\tau} = 12$  MeV.

Table 3.2

Contents of  $^{60}\text{Zn}$  coincidence gates at  $E_{\gamma} = 12 \text{ MeV}$ 

Window	Contents ( $\pm 1 \text{ keV}$ )
463 cont (465)	<u>311</u> , 726, 764, <u>827</u> , (914), (1176), 1214, 1270, 1326, 1333, 1399 (1899), 1943-1952
693 cont	339, 465
1003 +cont	(157) (208), <u>340</u> , 511, 1188, 1269, 1369, 1830, 1976, 2008, 2032, (2158), 2507, 2623, (2760), (2790), (2808), 2826
1188 +cont	261, <u>340</u> , 455, <u>511</u> , <u>546</u> , (579), <u>752</u> , 914, (937), <u>998</u> , <u>1002</u> , 1105, <u>1333</u> , <u>1342</u> , <u>1400</u> , 1612, (1937), (2158), (2277), (2307), (2350), (2486), (2589), (2741)
1403 cont (1399)	<u>340</u> , 454, <u>464</u> , 511, <u>1188</u> , 1333, <u>1644</u> , 2895
2007	(1003), (1189)
2031 cont (2028)	(423), (426), <u>1596</u> ( $^{59}\text{Cu}$ )
2158 cont	<u>511</u> , (1187) (Cu + Zn)
2189 cont	<u>339</u>
2508	(357), (998), 1003 (Cu + Zn)
2557	339, 511, (1368)
2502 cont (2577)	(1289), (1454), (1592), (2653), (2668)
3129 cont (3124)	(452), <u>511</u>

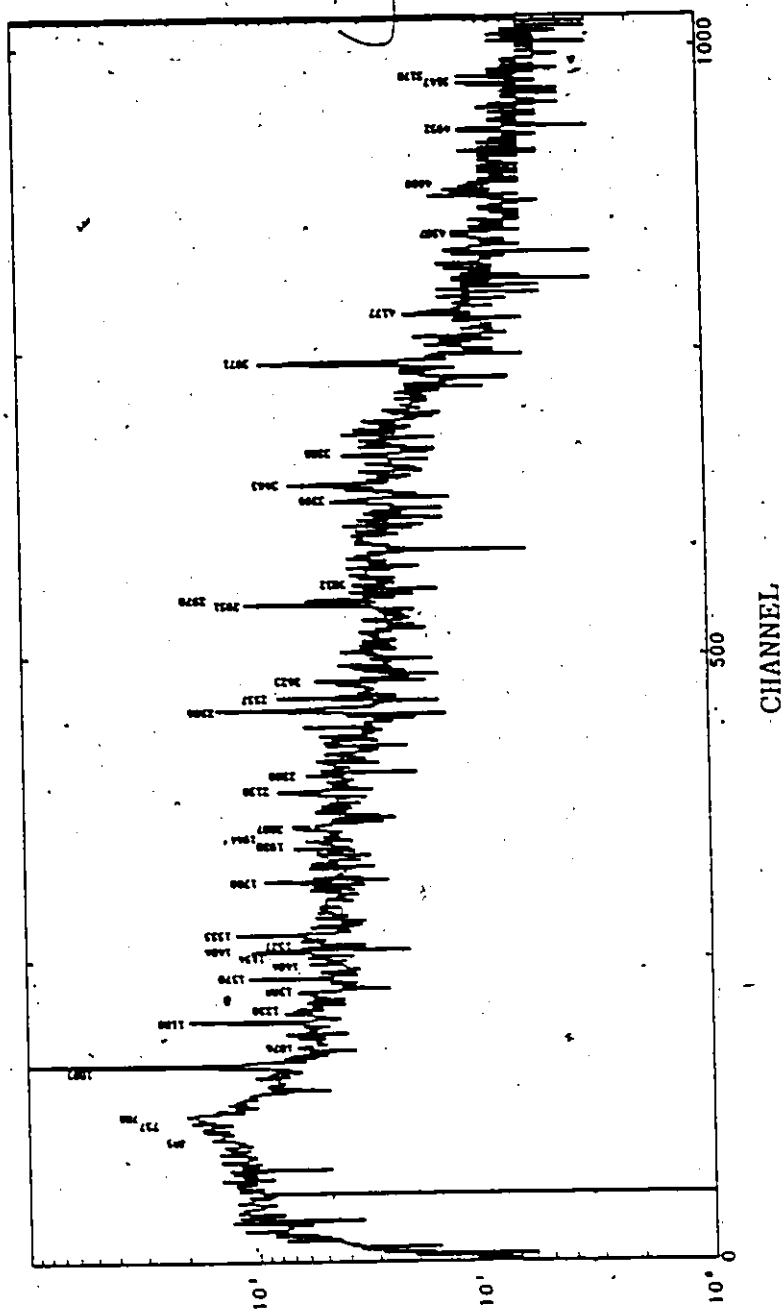


Figure 5.7. Clean  $n\gamma$  coincidence spectrum for  $^{60}\text{Zn}$  using gold beam dump, 11% intrinsic Ge  $\gamma$  detector, 12 MeV, sorted from address recorded  $\{E_\gamma, n\text{PSA}, n\text{PHA}, n\gamma\text{TAC}\}$

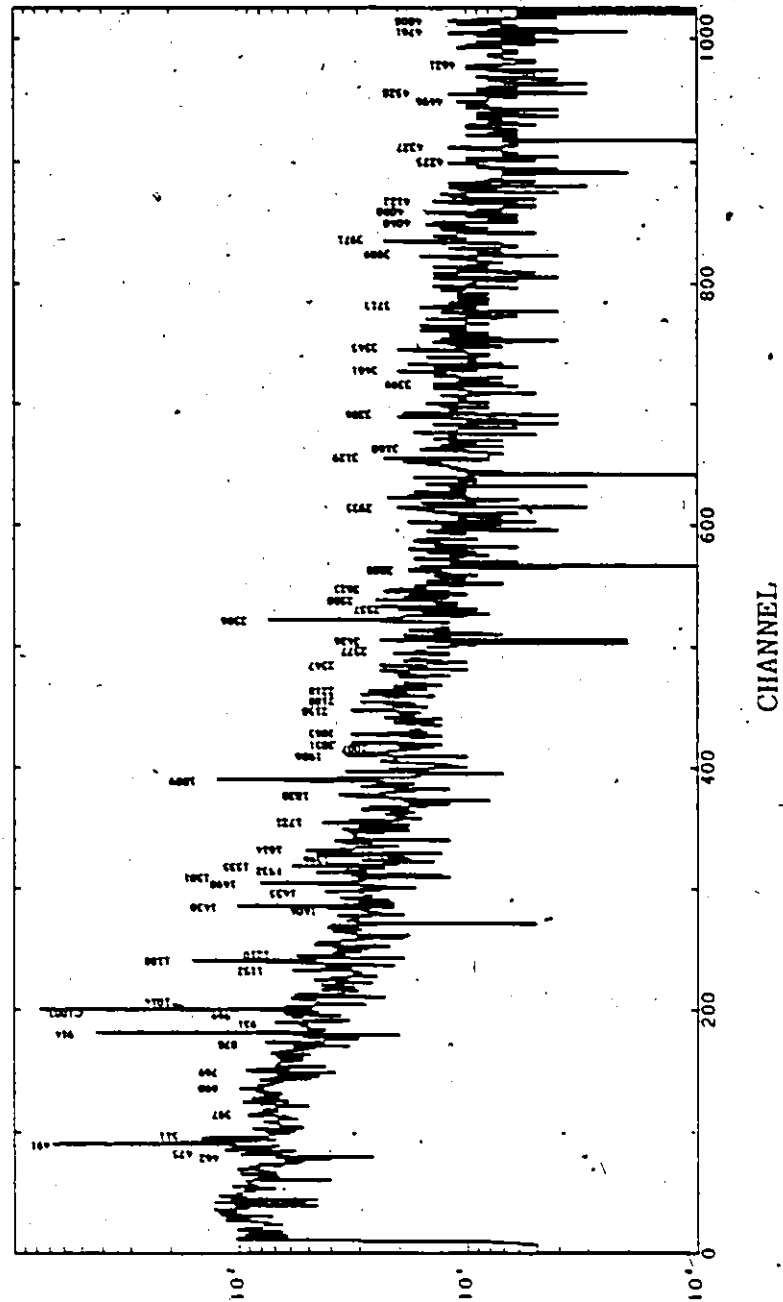


Figure 5.8. Clean  $n\gamma$  coincidence spectrum for  $^{60}\text{Zn}$  at  $E_\gamma = 8$  MeV.

small size of the  $^{60}\text{Zn}$  cross-sections may be appreciated here: candidate lines appear very weakly, if at all.

Singles  $\gamma$  angular distributions at 12 MeV were measured using 1 - 2 mg/cm<sup>2</sup>  $^{58}\text{Ni}$  targets with (to stop recoils) and without thin gold backings, but were generally not very useful. Singles  $\gamma$  yields with bombarding energies between 6 and 12 MeV were also measured but to little avail due to intrusions from other channels in the stronger peaks.

The level scheme of Figure 5.9 was gradually established using  $n\gamma$  coincidence data and at least two affirmatives from the  $\gamma\gamma$  coincidences, energy sums and matching to levels seen in the  $(\tau, n)$  and, to a lesser extent,  $(\text{HI}, \text{HI}')$  particle work as summarized by Auble (1979). For lines where intrusions from  $p\gamma$  or strong  $\bar{n}\gamma$  events could not be ruled out exclusively, the placements were assigned only tentatively. Spins and parities for this work were assigned on the basis of the  $n\gamma$  and  $(n-\bar{n})\gamma$  angular distributions with side feeding populations  $P(m=0) = 0.5$  and  $P(m = \pm 1) = 0.25$ . (The projection of orbital angular momentum for a state is zero when the emitted neutron is detected at  $0^\circ$  or  $180^\circ$  with respect to the beam axis. Since the incoming and outgoing particles each have intrinsic spin  $S=1/2$  with projections  $m_s = \pm 1/2$  and the reaction mechanism is expected to be predominantly compound nuclear at  $E_\tau = 12$  MeV, there are the four equally probable combinations  $(++, ++, ++, ++)$  resulting in the above final  $m$ -state populations. These populations were

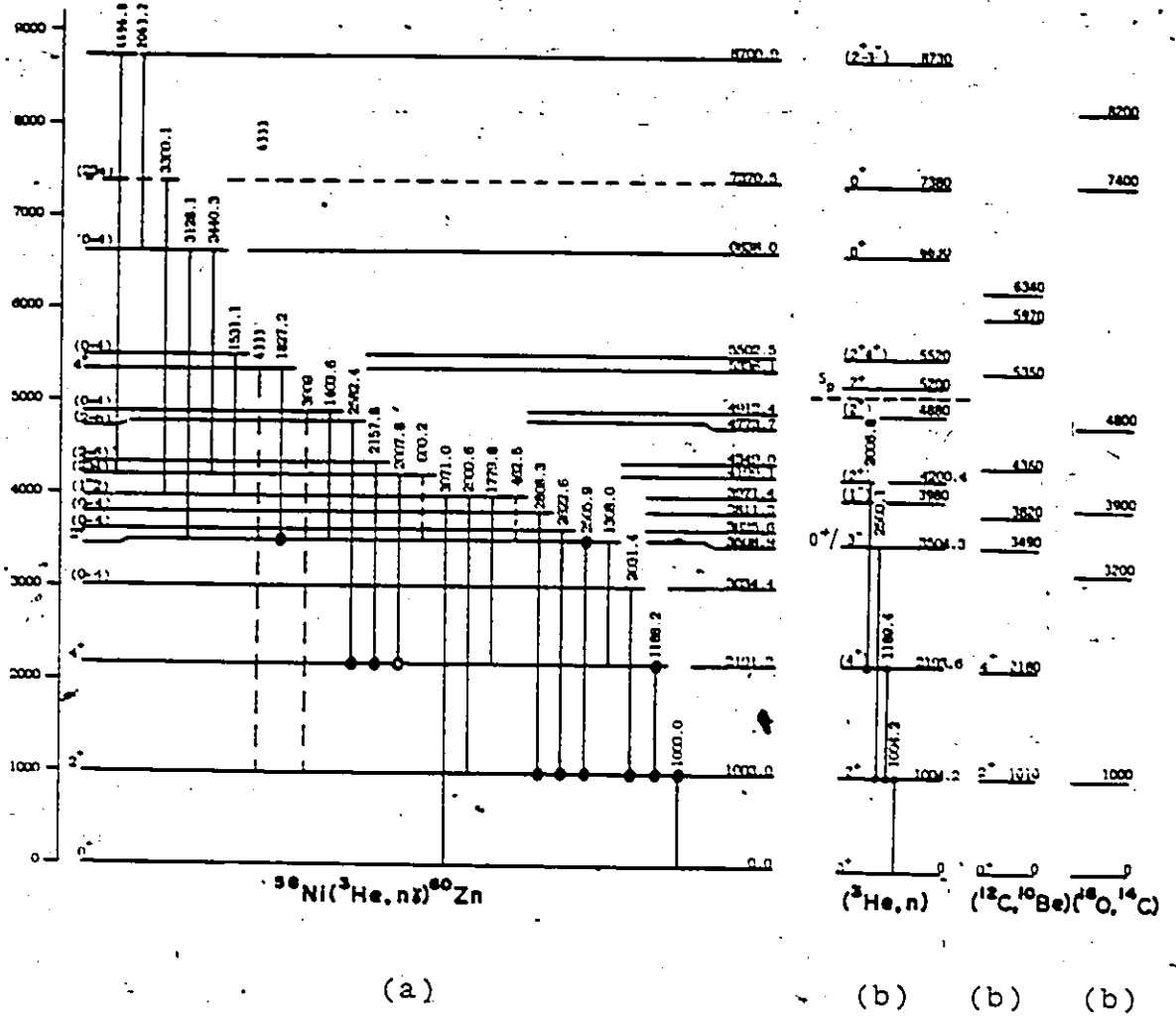


Figure 5.9. Proposed  $^{60}\text{Zn}$  level scheme obtained in (a), this work, and (b), elsewhere (as summarised by Auble, 1979).



also verified, within error, by examining the 1189 keV  $4^+ \rightarrow 2^+$  distribution under different, realistic assumptions.) The results of the  $(\tau, n\gamma)$  angular distributions and  $n\gamma$  yields are summarized in Table 5.3. For comparison, Figures 5.10 and 5.11 illustrate the level scheme in relation to theories (shell model, SDI, weak coupling) and systematics of nearby  $Z=30$  isotopes and  $N=30$  isotones. The  $Z=30$  systematics illustrate that  $^{60}\text{Zn}$  is a good vibrator, like the other even zinc isotopes except that only the  $4^+$  member of the  $0^+ 2^+ 4^+$  vibrational triplet has been identified. The systematics of the negative parity states may have to be "taken with a grain of salt".  $^{60}\text{Zn}$  is a self conjugate ( $Z=N$ ) nucleus with drastically fewer valence particles compared to the other zinc isotopes; it should have a simpler low-lying structure and be more free of intrusions of negative parity, which arise from the promotion of an odd number of valence particles to the higher positive parity shells, or to core excitations.

The heavy ion  $\gamma$  experiments failed to show any appreciable  $^{60}\text{Zn}$  activity. The two strongest possible lines were masked by those from other channels; weaker lines were difficult or impossible to see in the "grass" in the heavy ion singles- $\gamma$  spectra. Coincidence gates set on the 1003 and 1189 keV lines failed to show any signs of  $^{60}\text{Zn}$  lines known to feed the 1003 and 2191 keV levels, although weak decay lines from  $^{60}\text{Zn}$   $\beta^+$  decay could be seen in the beam off

Figure 5.10. Comparison of experimental levels of  $^{60}\text{Zn}$  with theories. Shown are SDI models of van Hienen et al. (1976), a shell model (SM-K) using the Kuo interaction by Wong (1970; similar to those of Singh and Rustgi, 1971), another shell model (SM-A) by Perazzo (1973) using the Argonne potential, and quartet model (QM) of Jaffrin (1972). (The experimental levels shown are those known at the time the above models were first studied.)

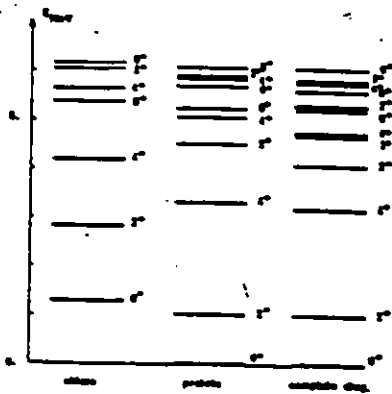
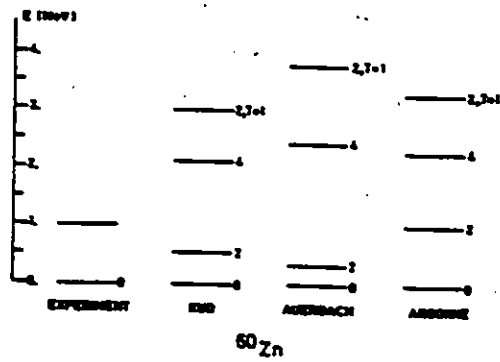
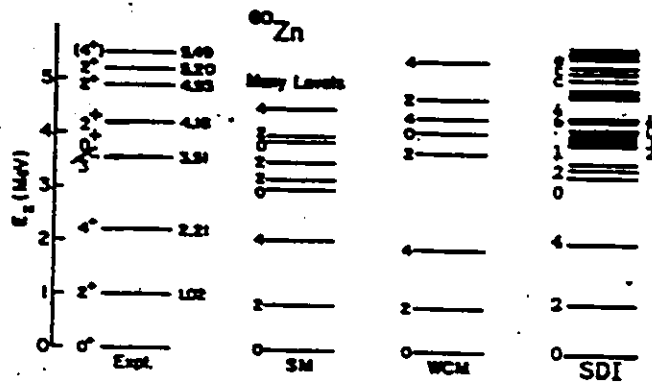


Table 8.3  
Summary of (1.87)<sup>60</sup>Co work

$E_{\alpha}$	$E_{\gamma}$	$J^{\pi}_i - J^{\pi}_f$	MEV	$\theta_2$	$\theta_4$	$\tan^{-1} \theta$	av slope <sup>a</sup>	$J^{\pi}_f$ adopted
1003.02±.14	1003.02±.14	2 <sup>+</sup>	100 <sup>+</sup>	.49±.03	-.06±.38	0	60±.03	3 <sup>+</sup>
2181.34±.20	1188.32±.14	4 <sup>+</sup>	100 <sup>+</sup>	.80±.03	-.26±.03	0	.18±.03	4 <sup>+</sup>
3034.45±.10	3031.42±.10	3 <sup>+</sup> (0-4)	100					(0-4)
3204.07±.89	3199.92±.45	3 <sup>+</sup> (3,3,4)	82±18					(3,3,4)
	1016.86±.80	4 <sup>+</sup>	47±28					(3,3,4)
3304.81±.24	3303.82±.20	3 <sup>+</sup> (3 <sup>+</sup> ) (3 <sup>-</sup> )	84±7 <sup>a</sup>	.31±.04	-.37±.24	-87.0±10 if J=3 -30±10 if J=3	.02±.04	(3 <sup>+</sup> )
	1304.02±.4	10 <sup>+</sup>	19±4					(3 <sup>+</sup> )
3438.42±.8	3432.42±.7	3 <sup>+</sup> (0-4)	100					(0-4)
3811.3±1.3	3808.3±1.3	3 <sup>+</sup> (0-4)	100					(0-4)
3871.41±.38	3871.05±.64	1 <sup>+</sup> (3 <sup>+</sup> ) (3 <sup>-</sup> ) (3 <sup>-</sup> )	70±8	.02±.08	-.37±.17	not unique	-.48±.87 -.18±.00 -.48±.87	(0-4) (3 <sup>+</sup> , 3 <sup>+</sup> )
	3449.8±1.0	2 <sup>+</sup>	10±11					(3 <sup>+</sup> , 3,4)
	1778.81±.83	4 <sup>+</sup>	14±18					(3 <sup>+</sup> , 3,4)
	483	(f)	6±8	not reliable cont.			const	
4199.07±.64	3007.82±.81	4 <sup>+</sup> (3,3,4) (3 <sup>+</sup> )	87±23 <sup>a</sup>	.49±.17	.71±.23	not unique	-.04±.06	(3 <sup>+</sup> , 3,4)
	690	(f)	32±37					
4318.99±.67	3187.78±.85	3 <sup>+</sup> (2-6)	100 <sup>+</sup>	.47±.09	-.38±.12	not unique	-.13±.11	(3-6)
4773.7±1.3	3582.4±1.3	3 <sup>+</sup> (3-6)	100 <sup>+</sup>	.31±.19	.45±.23	not unique		(3-6)
4813.4±2.8	3811±3	3 <sup>+</sup> (0-4) (3 <sup>+</sup> )	69±33 <sup>a</sup>					3 <sup>+</sup>
	1403.68±2.6	3 <sup>+</sup> (2 <sup>+</sup> )	82±18 <sup>a</sup>				.19±.28	
	719	(f)	6±7					
5320.4±2.8	3039.19±2.8	3 <sup>+</sup> (3-6) (3 <sup>+</sup> )	100				-.04±.27	3 <sup>+</sup>
5336.18±.34	4333	3 <sup>+</sup> (3,3,4)	33±24					(3,3,4)
	1837.31±.30	3 <sup>+</sup> (3,3)	82±12	.82±.07	.14±.18			(3,3,4)
5502.48±.72	3331.07±.80	3 <sup>+</sup> (0-4) (3 <sup>+</sup> , 4 <sup>+</sup> )	100				.32±.06	(3,3,4)
6438±1.3	3128.1±1.4	3 <sup>+</sup> (0-4) (10 <sup>+</sup> )	31±18					0 <sup>+</sup>
	3440.3±1.6	3 <sup>+</sup> (3,3,4)	43±18					
	1784	(f)	17±4 <sup>a</sup>					
7370.5±2.3	3389.1±2.1	3 <sup>+</sup> (3,3,4) (10 <sup>+</sup> )	17±4 <sup>a</sup>	(-.13±.18)	(-.00±.18)		-.02±.18	(3,3,4)
8700.9±1.4	6494.6±0.0	3 <sup>+</sup> (1 <sup>+</sup> , 3 <sup>+</sup> )	100 <sup>+</sup>	.83±.06	-.85±.11			(3,3,4)
	3063.31±.23	12 <sup>+</sup> , 3 <sup>+</sup>	30±20					(6-4)
		(01334)	70±23					

<sup>a</sup> based on intensities at 60° (otherwise 90°)  
(f) fitted & visibly seen  
(3) spin from particle work  
<sup>b</sup> av slope ± 0.35 π in (1/av ± 12 MeV)/(av ± 8 MeV)

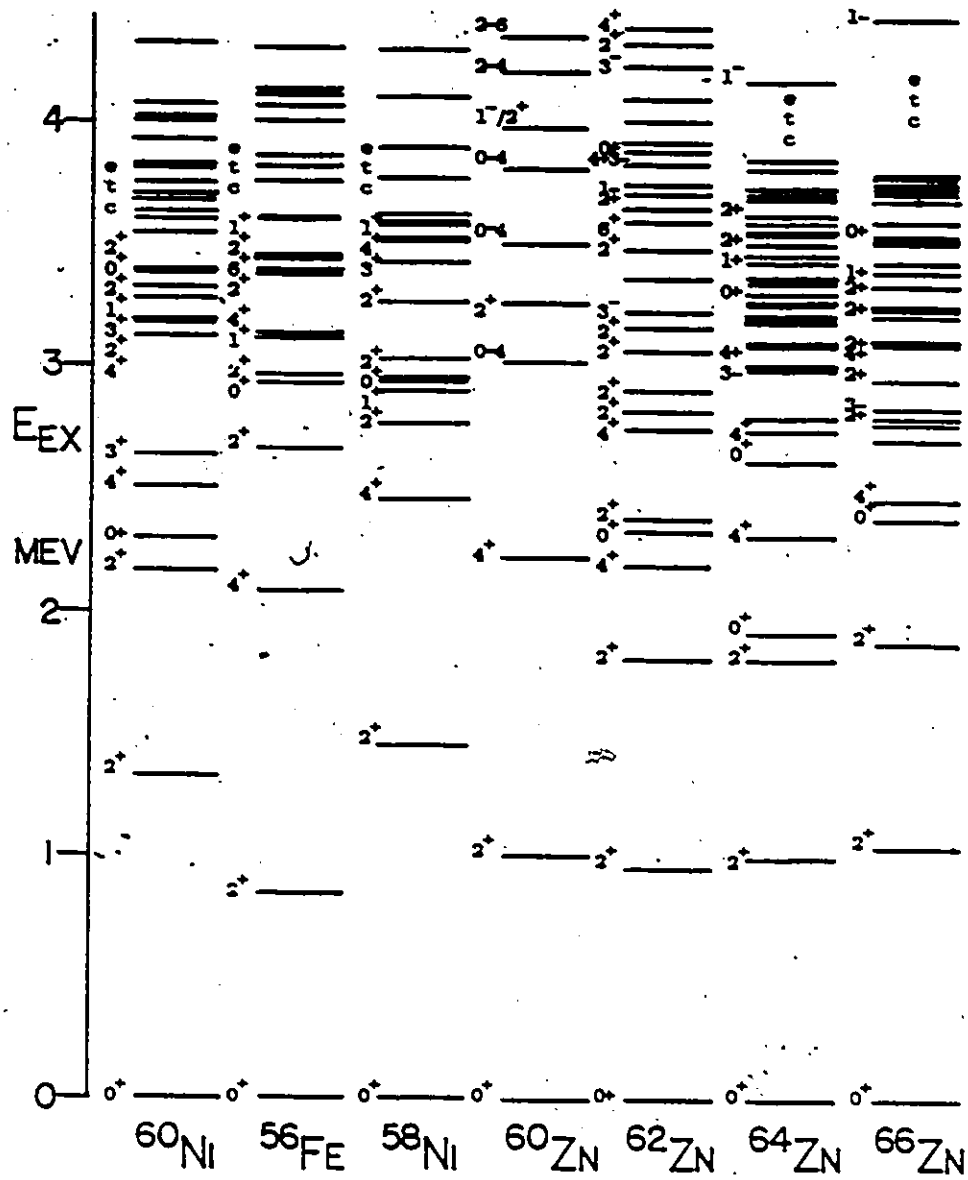


Figure 5.11. Even- $A$  systematics for  $N=30$  isotones and  $Z=30$  isotopes near  $^{60}\text{Zn}$ .

spectra for  ${}^6\text{Li}$  on  ${}^{58}\text{Ni}$ ,  ${}^{23}\text{Na}$  on  $\text{Ca}$ , and of course,  ${}^3\text{He}$  on  ${}^{58}\text{Ni}$ .

For the stronger  $n\gamma$  lines, no doppler shifts, within error were observed, nor were "electronic" lifetimes; this is consistent with the expected lifetimes being of the order of 1 psec (see below). Shifts for the weaker lines could not be reliably measured because of statistics. (The maximum possible shifts are expected to range from 0.2% for the first excited state to 0.4% at much higher excitation when the neutrons are detected at  $0^\circ$ .)

## 5.2 Discussion of levels

### 5.2.1 The 1003 and 2191 keV levels

The 1003 and 2191 keV levels have been well established from previous  $(\tau, n)$  and  $(\tau, n\gamma)$  work, with only the parity of the latter level being uncertain.

The 1003 keV  $2^+ \rightarrow 0^+$   $n\gamma$  distribution, which exhibited signs of a stretched E2 shape, nevertheless suffered from dealignment due to top feeding and possible  $\bar{n}\gamma$  intrusion. An estimate using 1/3 top feeding from the 2191 keV  $4^+$  level and 2/3 side feeding did not appreciably alter the final population statistical tensors from the pure side feeding assumption. In any case, the spin and parity of the 1003 keV level is already well established by particle work as  $2^+$ , which agrees well with systematics and theoretical

(shell model, weak and cluster coupling models, Hartree-Fock-Bogolyubov model) calculations.

The 1188 keV  $n\gamma$  distribution, when examined under  $J_i=0$  to 5 spin assumptions, showed a solution with sharp  $\chi^2$  minimum at zero mixing angle for  $J_i=4$ . The solution was also stable when the populations were allowed to vary over realistic limits. Negative parity was ruled out because the lifetime was measured to be under 5 ns. Therefore the 2191 keV level is assigned a definite value of spin and parity of  $4^+$ .

Systematics and theory place the lifetimes of the two levels at 1 to 2 ps, which is at the edge of the DSAM limits for the  $(\tau, n\gamma)$  experiment. No shifts were found within experimental error.

### 5.2.2 The 3509 keV level

The 3509 keV level decays to the 1004 keV level by the 2506 keV  $\gamma$  transition and to the 2194 keV level by a weak 1308 keV transition. Earlier nTOF distributions assigned a spin and parity of  $3^-$  to this level; more recent work gave it  $0^+$ , supposedly in good agreement with Kamermans et al's  $(\tau, n\gamma)$  studies. Both  $0^+$  and  $3^-$  appear to be contradicted by the results obtained in the present  $(\tau, n\gamma)$  studies: the  $A_4$  coefficient for the 2506 keV  $n\gamma$  distribution is definitely non zero which automatically rules out  $0^+$ ,  $1^+$ , and  $3^-$  as possible spin values for this level. (The last is

based upon the assumption that M2/E1 is improbable.) Only the  $J_1 = 2^+$  hypothesis yielded a  $\chi^2$  minimum below the 0.1% confidence limit of 6.9. The lack of any branch directly to the ground state -- otherwise allowed by spin considerations -- is consistent with the nearby even zinc isotopes and weak coupling theory of Vo Van et al. (1978). The latter predicts the third excited state to be  $2^+$  compared with the shell model's  $0^+$ . If the 3509 keV level is indeed the second  $2^+$  state, then it would seem to radically depart from systematics, which place such a level near 1.9 MeV. (It may be that weak levels not seen by the particle experiments may exist in the energy region; there exist several weak  $\gamma$  rays that could not be placed in the particle scheme. However, all the theories agree against such an energy.) A spin of  $0^+$  or  $3^-$  must also be ruled out because of the 3128 keV branch feeding the 3509 from the  $0^+$  6638 keV level. (Unfortunately, the 3128 keV line is obscured by the 3124 keV line from  $^{60}\text{Cu}$   $\beta$  decay in singles although it is consistently seen in  $n\gamma$  coincidence.) No consistent doppler shift was observed for the 2506 keV line, nor was there any evidence for an electronically measurable lifetime. Singles  $\gamma$  angular distributions appeared to suffer from intrusion of a nearby doppler shifting line and so were not reliable. A spin and parity of  $2^+$  is therefore assigned to the 3509 keV level.



### 5.2.3 The 3971 keV level

The existence of the 3971 keV level was determined by energy sums and matching to the 3.98 MeV level seen in the particle work. Branches to the 0, 1003, 2191 and 3509 keV levels were observed by way of 3971, 2970 and possibly 1780 and 463 keV  $\gamma$  transitions. (The last two suffer from severe  $\bar{n}\gamma$  intrusions.) The  $\chi^2$  values for the 3971  $n\gamma$  angular distribution showed no sharp minima and were generally rather large. The  $A_4$  coefficient ruled out  $J=1$  (but  $\delta A_4/A_4=0.5$ ; of course  $0 \rightarrow 0^+$  won't go by electromagnetic decay!); the  $\chi^2$  plots ruled out  $J_1=3$  or 4, which leaves  $J_1=2$ . In addition, only the  $J_1=2$  assumption yielded any  $\chi^2$  values (just) below the 0.1% confidence limit but only at large ( $64^\circ$ ) mixing angles. Otherwise, based on  $\chi^2$ ,  $1^-$  and  $2^+$  fits are equally mediocre. Also,  $2^- \rightarrow 0^+$  would be very unusual in this region! The  $J=2$  spin is in contradiction with the particle assignment of ( $1^-$ ). (Systematics also put ( $1^-$ ) in the 3.6 MeV region, but they may not be truly valid here.) A spin of ( $1^-, 2^+$ ) is therefore assigned to the 3971 keV level.

### 5.2.4 The 4199 keV level

The 4199 keV level decays to the 2194 keV level via a 2008 keV  $\gamma$  transition. Kamermans et al have assigned a spin of ( $2^+$ ) to this level, but the weakness of the line cannot possibly warrant  $n\gamma$  distribution analysis. Weak branches to the 3504 and 1004 keV levels may exist but the 690 and 3196

keV  $\gamma$  rays involved are strongly contaminated. If these branches do exist, then the value of the spin must lie between 2 and 4, inclusive. Because of the poor statistics, the  $n\gamma$  angular distributions obtained here cannot distinguish among any of the  $J_i=2$  to 4(6) assumptions.

#### 5.2.5 The 3811, 4349, 4774 and 5336 keV levels

The (heavy ion, particle) work places levels at 3.2, 3.82, 3.9, 4.36, 4.8 and 5.35 MeV in  $^{60}\text{Zn}$ . A very weak 2808 keV  $\gamma$  ray is seen in the  $n\gamma$  spectrum and the 1004 keV gate, so it is reasonable that the  $\gamma$  ray be placed as originating from the 3811 keV level. Because the distribution is too poor to be useful, only an upper limit of 4 may be assigned to the spin of the 3811 keV level.

A 2158 keV  $\gamma$  ray -- seen both in the  $n\gamma$  spectrum and the 1188 keV gate -- originates from the 4349 keV level. The  $n\gamma$  angular distribution cannot distinguish among the  $J_i=2$  to 6 possibilities, although  $J_i=5$  does yield the smallest  $\chi^2$  value, but at a large mixing angle of  $-74^\circ$ . Intrusion by the 2158 keV line from  $\beta$  decay of  $^{60}\text{Cu}$  is probably the main culprit, as the  $n\gamma$  distribution is very different after subtraction of the  $\bar{n}\gamma$  events. Arguments based on the lack of observed transitions to the  $0_1^+$  and  $2_1^+$  states cannot be invoked to infer  $5^+$  or  $6^+$  as the most likely spins due to the weakness of the level coupled with

poor efficiency in detecting the  $\gamma$  rays at the expected energies.

The 2582 keV  $\gamma$  ray is also seen in the 1188 keV window and so it must originate from a 4774 keV level. No definite spin is indicated from the angular distributions, which again are very different when corrected for  $\bar{n}\gamma$  events. ( $J_i=5, 3$  are preferred but at large mixing angles of  $-83^\circ, 73^\circ$ ; otherwise the remaining possibilities are generally equivalent.)

The 1827 keV  $\gamma$  ray depopulating a 5336 keV level is seen in both the 2506 and 1003 keV gates. Angular distributions give preference to the  $4^+ \rightarrow 2^+$  assumption. (It is surprising that this level was not seen in the  $(\tau, n)$  work but perhaps this is due to poor resolution and overlap of the nearby 5200 and 5520 MeV levels.) There is also weak evidence for a 4333 keV branch to the 1003 keV level. A spin of  $4^+$  is therefore assigned to the 5336 keV level.

#### 5.2.6 The 4912, 5502, 6638, 7371, and 8701 keV levels

The 1403 keV  $\gamma$  ray depopulating the 4912 (as determined by energy sums) is obscured by the 1398 keV line from  $(\tau, pn\gamma)^{59}\text{Cu}$  at 12 MeV bombarding energy, but not at 8 MeV. Two small "bumps" in the spectra at 713 and 3909 -- corresponding to decays to the 4199 and 1003 keV levels -- are sometimes seen in the various  $n\gamma$  spectra, but not always, nor are they really large enough to be statistically

certain. The spin for the 4912 keV level can be anywhere from 0 to 4 based on the  $\gamma$  branch(es) which is not inconsistent with the  $(\tau, n)$  assignment of  $(2^+)$ .

The 5502 keV level was determined by the energy match between the weak 1531 keV  $n\gamma$  line to the 5.52 keV  $(\tau, n)$  particle level from the 3971 keV level. Spin is limited to 2 to 6 compared with the particle work assignment of  $(2^+, 4^+)$ .

The 6638 keV level is depopulated by 3128 and 2440 keV lines feeding the 3509 and 4199 keV levels. (There may also be a weak 1724 keV line, contaminated by the strong nearby 1730 keV line, which could feed the 4912 keV level.) Since the  $\gamma$  angular distributions are too poor to be of use, the spin can only be limited to between 0 and 4 whereas the particle work assigns a definite value of  $0^+$ .

The tentative 7371 keV level feeds the 3971 keV level via a 3399 keV  $\gamma$  transition as determined by energy matching. The  $a_4$  coefficient of -0.8 automatically rejects 0 or 1 spin assumptions which contradicts the particle assignment of  $0^+$  for the spin of the 7370 keV level (hence the tentative level assignment). Unfortunately, the distributions do not readily distinguish between the  $3 \rightarrow 1^-$  ( $x_2^2$  is still very high;  $2 \rightarrow 1^-$  is much worse,  $4 \rightarrow 1^-$  has an unacceptably large  $E4/M3$  mixing ratio) and  $(2, 4) \rightarrow 2^+$  is similarly bad.

The 8701 keV level has two decay branches as determined by energy sums: 2063 and 4497 keV to the 6638 and 4199 keV level. Because of the uncertainties in the final state spin, the spin for the 8701 keV level can only be restricted to a maximum of 4.

#### 5.2.7 The 3034 and 3626 keV levels

The 2031 and 2623 keV lines are seen very weakly in the 1003 keV gates as well as in  $\gamma\gamma$  coincidence. Their assignments as originating from the 3034 and 3626 keV levels can only be made tentative owing to the lack of matching particle levels and the fact that unseen intermediate  $\gamma$  transitions might exist (the gain was set so that a maximum of only 3 MeV could be recorded in the  $\gamma$  detector in the  $\gamma\gamma$  experiment). Perhaps either the 3034 or 3626 keV level may be the sought-after rotational  $4^+$  level discussed below. Alternatively, the 3626 keV level might explain the  $0^+/3^-$  ambiguity assigned to the 3509 keV level for the neutron time-of-flight work.

## CHAPTER 6

### Summary and Concluding Remarks

The experimental results of this project have certainly extended the knowledge of the nuclear structure of  $^{60}\text{Zn}$  and  $^{61}\text{Zn}$ . Using a  $^3\text{He}$  ion chamber neutron detector, the level scheme and binding energy for  $^{61}\text{Zn}$  were determined much more accurately than any heavy-ion particle work (Woods et al., Weber et al.) or than any possible neutron time-of-flight methods. Independent information from n- $\gamma$  and  $\gamma$ - $\gamma$  coincidence techniques confirmed and extended the level scheme to higher excitation energy. Furthermore, information about spins, parities, mixing ratios, branching ratios and lifetimes for the levels was extracted from the same  $\gamma$  work. Comparison of the present work with the particle work of Woods et al. and Weber et al. and the (simultaneous) n $\gamma$  work of Smith et al. showed excellent agreement, especially with the latter. Some exceptions did arise; namely, identification of several n $\gamma$  doublets and levels missed by Smith et al. In addition, many of the spin and parity assignments made in the present work were made on firmer grounds than by Smith et al., owing to better treatment of populations of the m-substates and use of lifetime information.

Although attempts at heavy-ion particle experiments proved unsuccessful (more as a result of mishaps than anything else), the heavy ion induced  $\gamma$  decay studies provided some limited success in extracting information on  $^{61}\text{Zn}$ ; notably the multi- $\gamma$  coincidence work with the  $^{24}\text{Mg} + \text{Ca}$  reaction confirmed and extended portions of the level scheme somewhat, and the singles- $\gamma$  study of  $^6\text{Li} + ^{58}\text{Ni}$  proved the (not unexpected) existence of the 418 and 755 keV levels previously obscured by carbon contamination in the ( $^6\text{Li}, t$ ) particle work of Woods et al. The superior resolution inherent in the  $\gamma$  work made possible the isolation of, for instance, the 124 keV level from the 88 keV level. On the other hand, the fact that the singles- $\gamma$  work could not discriminate against the overwhelming undesired channels meant that some regions in the  $\gamma$  decay scheme were obscured.

The same n- $\gamma$  and  $\gamma$ - $\gamma$  coincidence techniques as above were employed to ascertain structural information on  $^{60}\text{Zn}$  via the ( $\tau, n\gamma$ ) reaction, but with much more limited success. While it is true that many more lines and levels in  $^{60}\text{Zn}$  were identified in the present work than by Kamermans et al. (partly because of the latter's high neutron energy threshold), it was necessary to place reliance on the neutron time-of-flight work of Alford et al., Brill et al., Evers et al., Greenfield et al., Miller et al., and Winsborrow et al. to assist in the determination of the  $\gamma$  decay scheme. Since the overabundance of  $\gamma$ -rays from competing channels was the

main culprit responsible for this problem, one immediate solution would be to measure  $n-\gamma$  and  $n-\gamma-\gamma$  coincidences using arrays of both neutron and  $\gamma$  detectors to improve overall efficiency and selectivity. Furthermore, the improved pulse shape sensitivity of materials such as PILOT PS fluid over NE213 or NE218 should be used to advantage; also an arrangement for simultaneously measuring samples of singles spectra of in-beam and beam-off  $\gamma$  activity plus standard reference  $\gamma$  sources located nearby should be incorporated to determine efficiency and energy calibrations to maximum accuracy, particularly important if angular distribution and DSAM techniques are to be employed to their limits. Such an arrangement might easily consist of a random coincidence between any  $\gamma$  detector in the array and a pulser to generate a logic gate and routing bit to distinguish the event from a normal  $n\gamma$  or  $n\gamma\gamma$  coincidence; another set of routing bits would distinguish beam-off from beam-on events.

The results have also demonstrated the validity of the Surface Delta Interaction/Shell Model theory of van Hienen et al. in a region often described as vibrational. Agreement between theory and experiment of excitation energies and spins for  $^{61}\text{Zn}$  is very good below 2 MeV in excitation with a few minor discrepancies. For instance, the ordering of the lowest three states is incorrectly predicted by SDI, but it should be born in mind that these



three levels are not that different in energy; more importantly, only the average parameters from nickel and copper isotopes were used, which is justifiable in its own right. By "fine-tuning" the parameters to incorporate zinc, especially  $^{60,61}\text{Zn}$ , it is most probable that the SDI model would do an even better job of describing  $^{60,61}\text{Zn}$ . Approximations made in the SDI model, such as neglecting core excitations and restricting the space to the  $1f_{7/2}$  subshells, have been shown elsewhere (eg. Roodberger et al., 1981) to be more applicable to the zinc isotopes than to copper or nickel. For  $^{60,61}\text{Zn}$  this is even more so, although  $^{60}\text{Zn}$  still exhibits, not unexpectedly, a definite vibrational character, as suggested by the 0, 1004, 2194 keV/ $0^+$ ,  $2^+$ ,  $4^+$  levels, spaced almost equally at 1 MeV apart.

Qualitatively, the lifetime limits, branching ratios and E2/M1 mixing ratios (where available) suggest E2/M1 enhancements as expected by the vibrational model, but not so excessively large that they cannot be accommodated by a large though still plausible effective charge in the shell model. It is a pity that the lifetimes of the excited states could not be measured more accurately as they, along with branching and mixing ratios, represent an even more powerful test of the various theoretical models. Since the only calculations of reduced transition rates appearing in the literature are for  $^{60}\text{Zn}$  (and sparse at that!), perhaps this thesis will inspire others to extend their model calcu-

lations to  $A < 62$  for the zinc region. In any case, the lifetime limits generally appear reasonable when compared to the nickel isotopes (two protons removed) or the other nearby zinc isotopes. Since the lifetimes (limits) were measured to be between 5 ps and 5 ns, some suggestions for improving the precision of the measurements might be to incorporate DSAM with the  $(\tau, n\gamma)^{60}\text{Zn}$  and  $(\alpha, n\gamma)^{61}\text{Zn}$  reactions at higher bombarding energies (limited by cross section roll-off with energy), and to use an annular neutron detector placed at  $180^\circ$ , instead of the previously used  $0^\circ$  configuration, to maximize the initial<sup>-</sup> velocities of the recoiling nuclei. The DSAM with the  $^{40}\text{Ca}(^{24}\text{Mg}, 2pn)^{61}\text{Zn}$  heavy ion reaction at 60 to 85 MeV should have been very fruitful as the recoiling momenta are four times greater than the above  $\alpha$  induced reactions. However, the  $\gamma$  calibrations for the detectors used in the MPF in singles mode were not sufficiently reliable. Again, an obvious solution to this problem in any future experiments would be to place standard  $\gamma$  reference sources near the target that are suitably chosen to map out the energy region without obscuring any  $\gamma$ -rays of interest from the target itself. Comparing thin targets, of order  $0.1 \text{ mg/cm}^2$ , with thick ones, of order 1 to  $10 \text{ mg/cm}^2$ , and with and without lead backings might prove useful as well, as would investigating targets comprised of layers of Ca or  $^{58}\text{Ni}$  (or any other desired

target) alternating with low density material in an effort to reduce the stopping power for the recoils.

It was also disappointing that the heavy ion induced  $\gamma$  experiments yielded so little in terms of results for  $(59), 60, 61\text{Zn}$ . This should not be unexpected as the Coulomb barriers are easily offset by the larger Q-values for proton emission in this region. However, Mother Nature is not always malevolent: new information about the structure of  $59, 60\text{Cu}$  is not unwelcome and is important in its own right (see appendix).

To study the beam-off  $\beta/\gamma$  decay and/or  $\beta$  delayed proton emission of  $59\text{Zn}$  and  $61\text{Ga}$  (or even  $58\text{Zn}$ ,  $60\text{Ga}$ ,  $61, 62\text{Ge}$ ) following the  $\text{Ca} + \text{Mg}$  reaction, it is clear from the present "negative" results of the mechanically chopped beam/insitu  $\gamma$  decay experiments that some kind of separation technique will have to be employed to improve the "signal" over the "noise" from the more prominent but undesirable decays. Suitable techniques commonly used are transport of the recoil particles by either a helium jet or "ticker-tape" to a background reduced counting room, perhaps in conjunction with an off-line (or even on-line magnetic isotope separator. Another simple solution might be to employ a moving ribbon target that is heavily shielded except in the immediate vicinity of the beam in an effort to enhance detections of the short-lived, though rarer, decays. over the much longer ones.

The work presented here does not represent a closed chapter on  $^{60}\text{Zn}$  or  $^{61}\text{Zn}$ . With future refinements of acquisition and analysis techniques, such as the use of neutron-particle- $\gamma$  crystal balls with high efficiency in detecting radiations and classifying channels in heavy ion experiments, neutron-electron coincidence employing high efficiency and high resolution detectors to measure electron conversion coefficients, construction of an end-on geometry Seforad-type neutron detector for low energy ( $\alpha, n$ ) spectroscopy, use of "exotic" reactions such as  $(\pi^+, \pi)$  (when better resolution becomes available), use of radioactive beams or targets, etc., new information might indeed be gleaned.

Additional crucial measurements might include missing model-expected levels and decay branches. A relevant example would be the discovery of another  $3^-$  level 1/2 MeV higher than the first  $1^-$  level in  $^{60}\text{Zn}$  and another  $4^+$  level around 3 to 4 MeV in excitation as predicted by a very simple rotational model: the two protons and two neutrons outside the  $^{56}\text{Ni}$  core should couple to form an alpha cluster rotating around the core with level spacings analogous to those of the HCl molecular spectra, or the rotational levels of  $^{20}\text{Ne}$  ( $^{16}\text{O}$  core +  $\alpha$ ) or  $^{44}\text{Ti}$  ( $^{40}\text{Ca}$  core +  $\alpha$ ), which exhibit a second band of odd integer spin and negative parity. The only other way to explain the lower lying negative parity states in  $^{60}\text{Zn}$  or positive parity in  $^{61}\text{Zn}$  is by  $g_{9/2}$ ,  $d_{5/2}$  and  $g_{7/2}$  intrusions, as mentioned previously.

(Perhaps the repulsive residual interactions between the four particles are sufficient to inhibit their clustering together, though it is surprising that both  $^{62,64}\text{Zn}$  exhibit levels explainable by the above rotational model. It is curious that Jaffrin (1972) made no mention of such negative parity states in his quartet cluster calculations for  $^{60}\text{Zn}$ .)

Successful or not, the above remain the subject for further investigations.

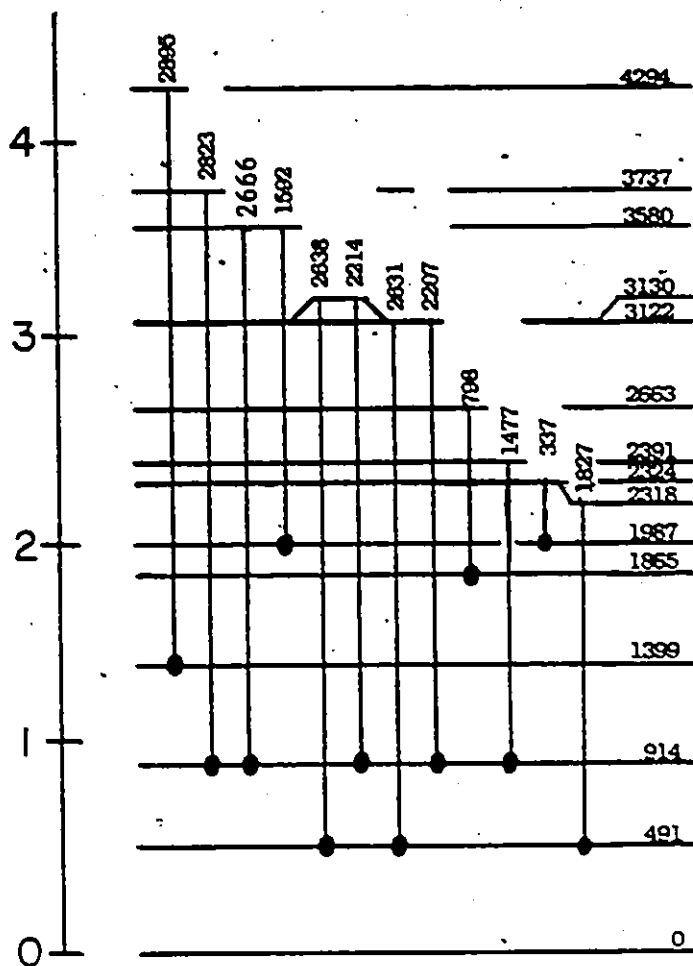
## APPENDIX

### A.1 $^{58}\text{Ni}(\tau, p\gamma)^{59}\text{Cu}$ reaction

New levels and  $\gamma$  rays in the  $^{58}\text{Ni}(\tau, p\gamma)^{59}\text{Cu}$  reaction, have been observed via the  $\gamma\gamma$  coincidence gates, as summarized in Figure A.1.i and Table A.1. For comparison, the  $(\tau, d\gamma)$  and adopted levels compiled by Kim (1976) are shown in Figure A.1.ii. Recently these new levels have been verified in proton capture studies by Din et al. (1984), so further analysis of the  $(\tau, p\gamma)$  data regarding spins, mixing ratios branching ratios, etc. is not warranted.

### A.2 New levels in $^{60}\text{Cu}$ produced by heavy ion reactions

Many  $\gamma$ -rays belonging to  $^{60}\text{Cu}$  have been identified in the  $(\tau, n\gamma)$   $\gamma$ - $\gamma$  coincidence and  $\gamma$ -singles experiments and by energy sums and matching to  $(\tau, p)$  and other charged particle work, summarized by Auble (1979). The more intense  $\gamma$  rays have been observed in the  $(\alpha, p\gamma)$  channel at 20 MeV in the present  $^{61}\text{Zn}$  study. Prior to these investigations only a few  $\gamma$ -rays belonging to  $^{60}\text{Cu}$  were known; since then, Chan et al. (1982) have reported their results of an intensive study of the  $(\alpha, p\gamma)$  reaction. Figure A.2i shows the level scheme obtained by the present  $(\tau, p\gamma)$  work. For comparison, Figure A.2.ii shows the level schemes of the previously known



$^{58}\text{Ni}(\tau, p n \gamma)^{59}\text{Cu}$

Figure A.1. New lines and levels in  $^{59}\text{Cu}$  via  $(\tau, pn\gamma)$  at 12 MeV (i), compared to  $(\tau, d\gamma)$  and adopted levels as compiled by Kim (1976) (ii).

NUCLEAR DATA SHEETS.

DRAWING 22 A - 59

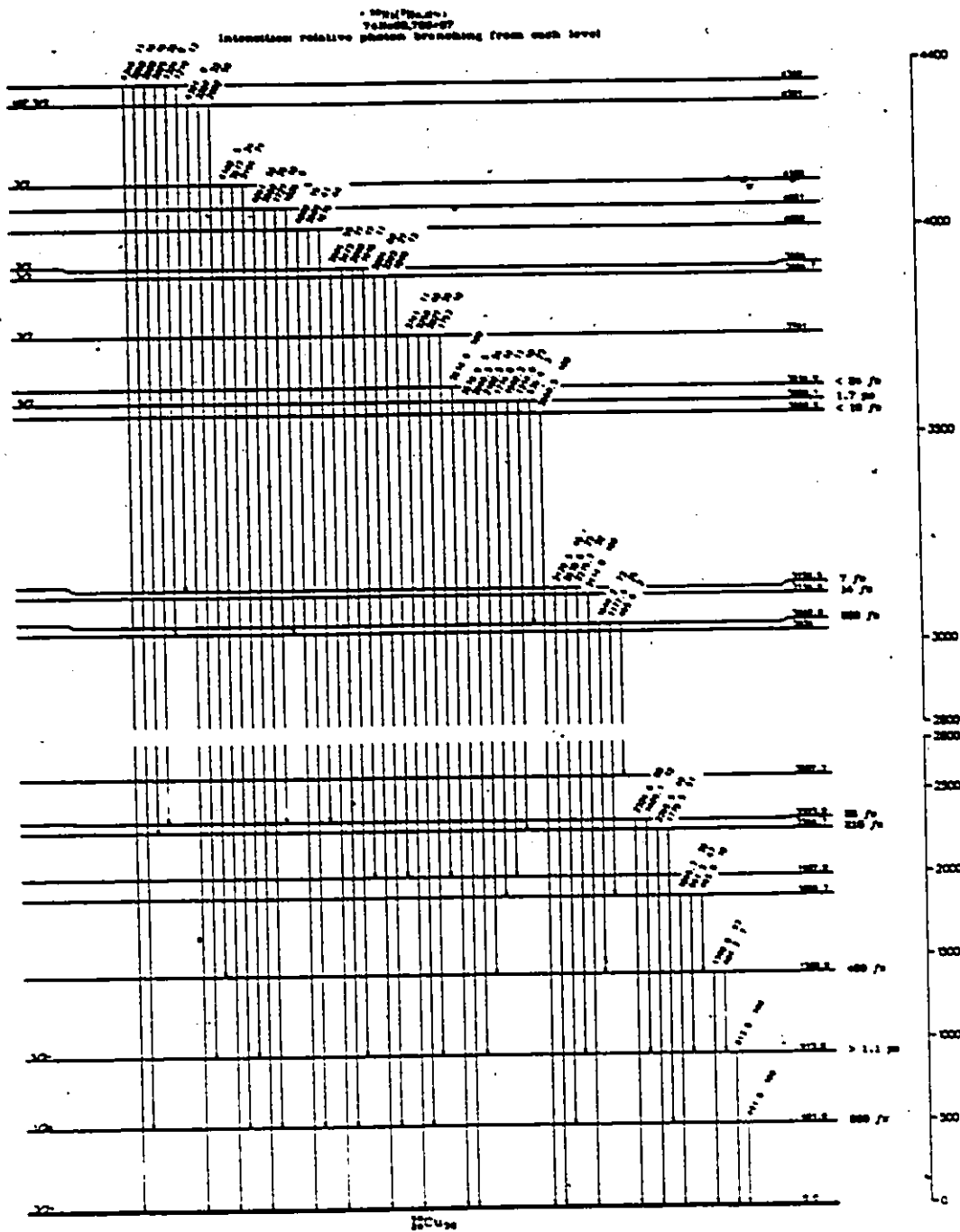


Figure A.1 ii.



Table A.1

New  $\gamma$  lines and levels in (r,pay)<sup>59</sup>Cu

$E_{ex}$ (keV)	$E_{\gamma}$ (keV)
2318	1827
2324	337
2391	1477
2663	798
3122 $\pm$ 1	2630.8 $\pm$ 1.0
	2206.9 $\pm$ 1.4
3130 $\pm$ 1	2637.5 $\pm$ 1.0
	2214.4 $\pm$ 1.6
3380 $\pm$ 0.7	2666.3 $\pm$ 0.7
	1591.9 $\pm$ 1.5
3737 $\pm$ 2	2822.9 $\pm$ 2.0
4294 $\pm$ 2	2894.8 $\pm$ 2.0

Figure A.2.  $^{60}\text{Cu}$  level schemes based on present  $(\tau, p\gamma)$  work, (i), compared with  $(\tau, p)$  particle and other  $\gamma$  experiments as summarised by Auble (1979), (ii), and present  $(\text{HI}, xn\text{p}\gamma)$  work, (iii).

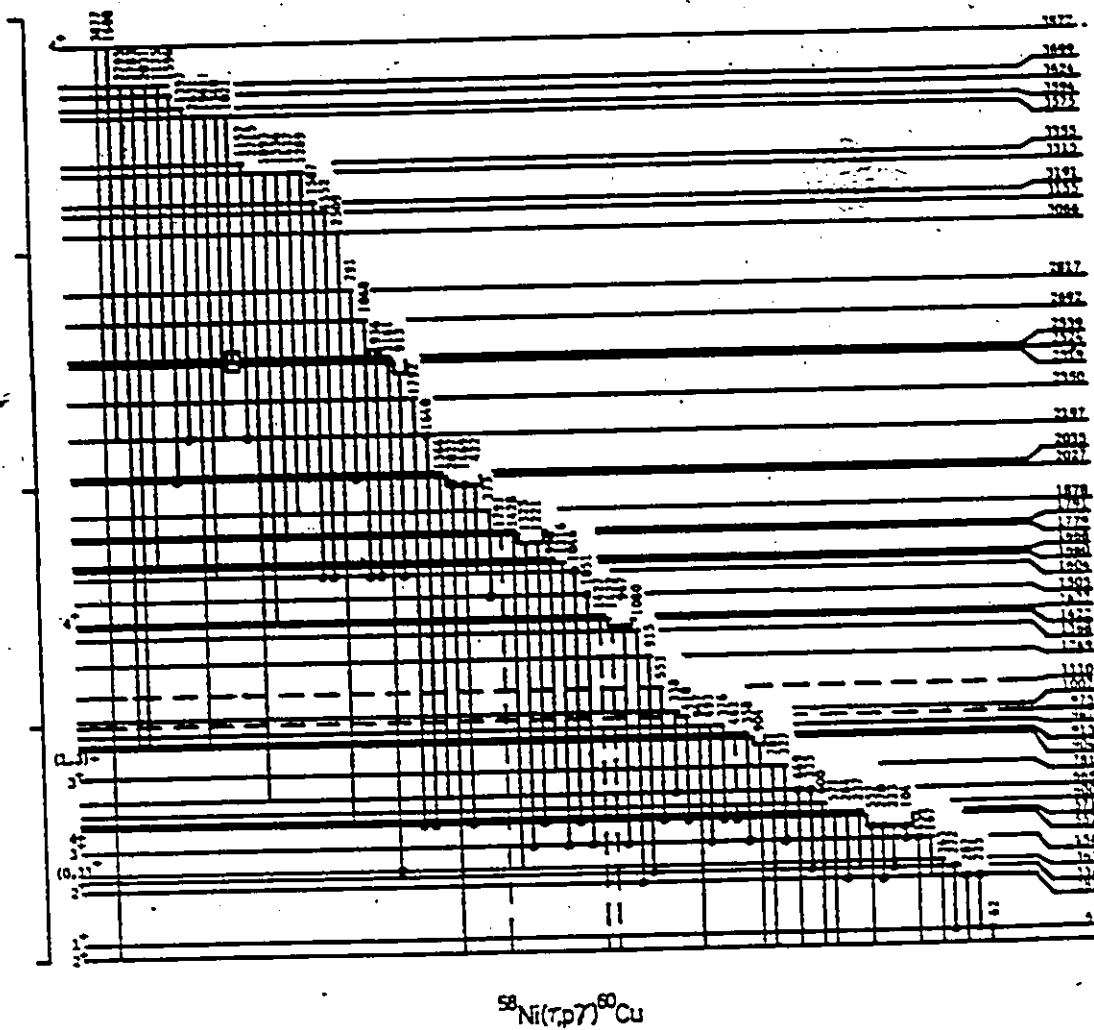


Figure A.2 i.

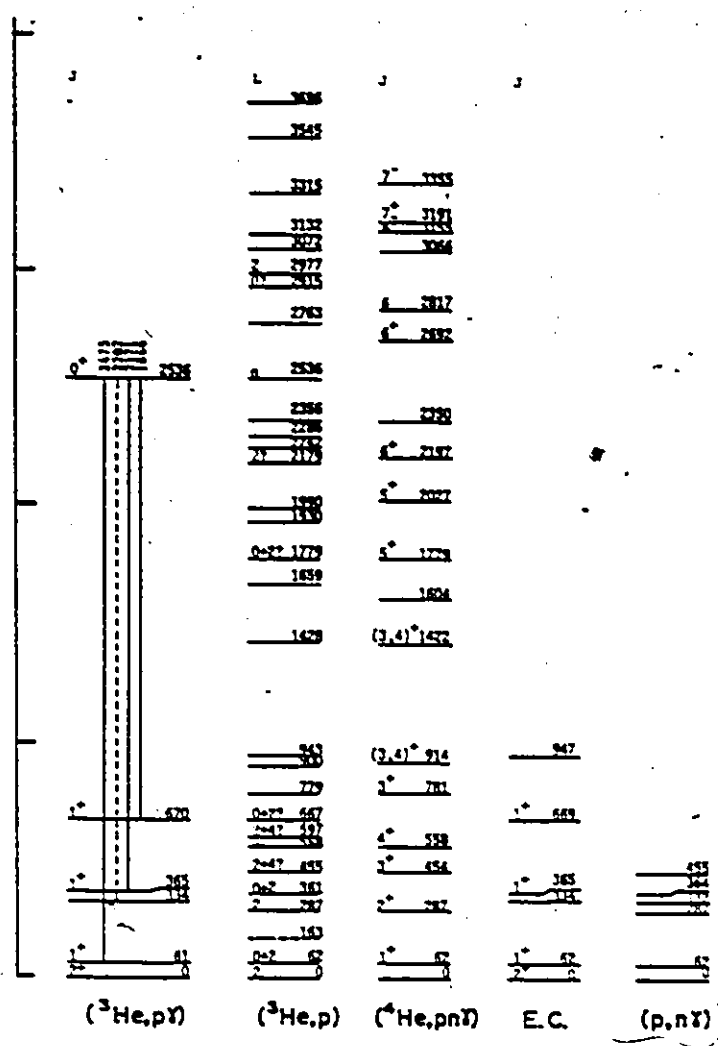


Figure A.2 ii.

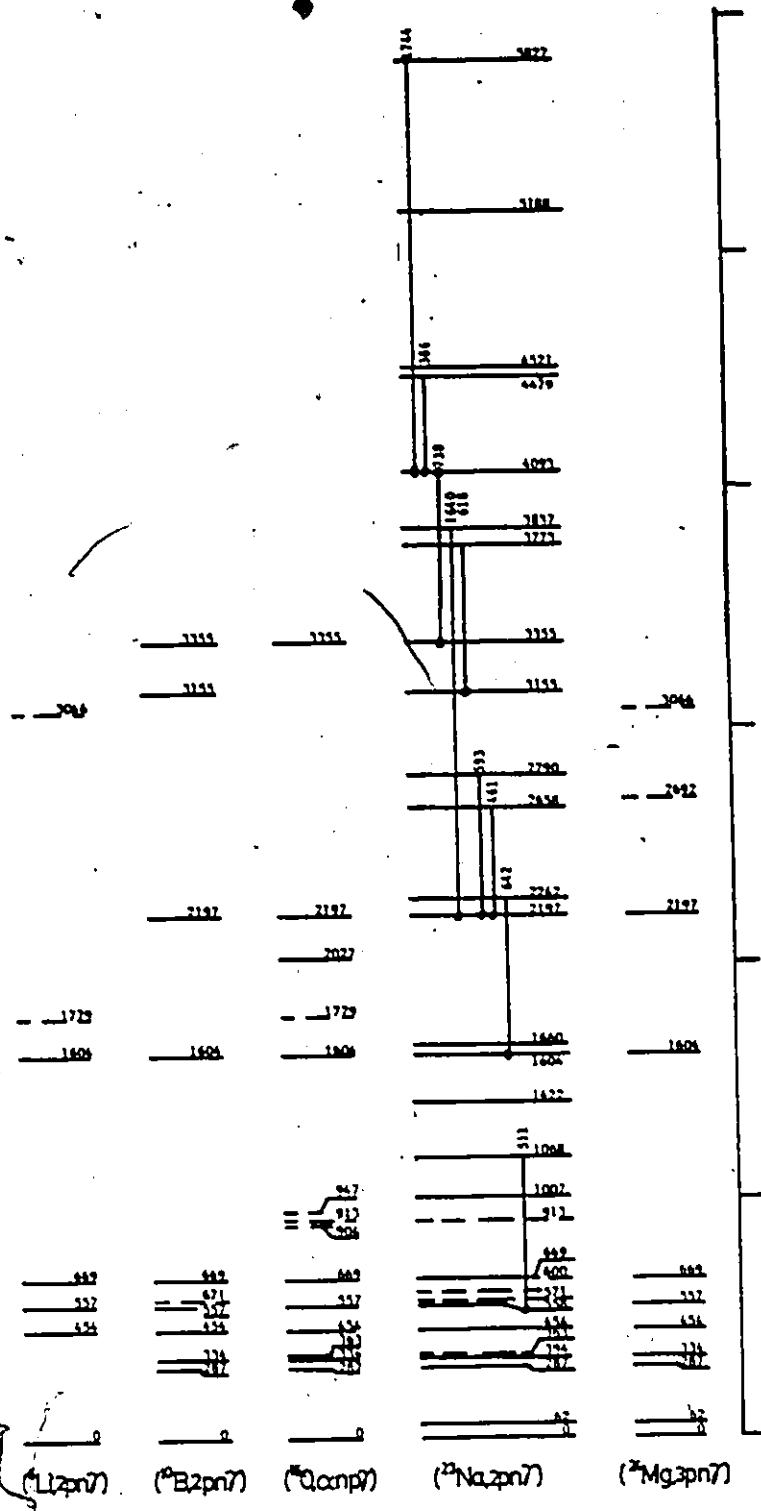


Figure A.2 iii

( $\tau, p\gamma$ ), ( $\tau, p$ ), ( $p, n\gamma$ ) and electron capture/ $\beta^+$  work summarized by Auble and the ( $\alpha, p n\gamma$ ) levels of Chan et al.

Many of the  $^{60}\text{Cu}$   $\gamma$ -rays have been observed in the singles  $\gamma$  spectra of the heavy ion reactions  $^{23}\text{Na}$  on Ca,  $^{24}\text{Mg}$  on Ca,  $^6\text{Li}$  on  $^{58}\text{Ni}$ ,  $^{10}\text{B}$  on  $^{54}\text{Fe}$ , ( $^{16}\text{O}$  on  $^{50}\text{Cr}$ ), as summarized in Table A.2.1. Many new lines and levels were found from the coincidence gates of the  $^{24}\text{Mg}$  and  $^{23}\text{Na}$  on Ca multi-coincidence experiments. Contents of these gates are summarized in Table A.2.2 and A.2.3. The level schemes based on the present heavy ion work are shown in Figure A.2.iii and are summarized in Table A.2.4.

### A.3 Other channels

Many other channels, such as  $^{57-61}\text{Ni}$ ,  $^{59,61}\text{Cu}$ ,  $^{62}\text{Zn}$  etc. were seen in the heavy ion experiments described above. A preliminary scan of the  $^{24}\text{Mg}$  and  $^{23}\text{Na}$  on Ca coincidence gates failed to reveal any new lines. No coincidence measurements were performed for the  $^{10}\text{B}$  on  $^{54}\text{Fe}$ ,  $^{16}\text{O}$  on  $^{50}\text{Cr}$  and  $^6\text{Li}$  on  $^{58}\text{Ni}$ .

Table A.2.1  
Summary of  $^{60}\text{Co}$   $\gamma$  rays observed in the  $\gamma$  experiments

	e	v	Li	P	O	Na	Mg
63	x	x		X rays c	X rays c	X rays c	x
104	x	x		x	x	x	c
167		x	o	c		c	?
167	x	x	o	?		?	
220 <sup>d</sup>	x	xx		x	x	x	x
227		x		?	x	(x)	x
272 <sup>t</sup>	xx	xxx	c)	c	(c)	x	?
284		x	o	c		x(c)	c
287	x	x		c		x(c)	c
327	x	x		c		x	c
334	x	x		o	(c)	o	c
338		no		o	(c)	o	c
348		x		o	(c)	c	
357	x	x		o	(x)	(x)	
364	x	x	o	c	x		
372		x		c	(x)		c
378		x		o	(x)	(x)	
386						x	
418	unplaced x		o	o	(x)	x	c
422		x	o	o	o	o	c
434	x	x		x	x	x	x
462 <sup>d</sup>	x	x		?		xx	
483		x	c	c			7c
511		x	c	o	o	x(coin)	c
553	unplaced x	unplaced x			x	x	
558	x	x	x	x	x	x	x
571		x		(?)			
583 <sup>d</sup>			c	c	(x)	xx	
600		x	c	o		x	c
618	x					x	
643	unplaced x				c	now placed	
669		x	x	x	x	x+c	x+c
728				o	(c)	x	c
781	x				(c)		
780	x	x	(c)	c	(c)	no	
804		x			(x)		
813 <sup>d</sup>	o	cx				c?	
836		cx	c	o	(x)	c?	
847	x	?	o	c	(x)		
868	x	?	c	c	(c)	c	c
886		x coin	c	c		c	c
1021		x		o		x	c
1048	x	x	(x)	c	no	x	?
1061		x	c	c			
1080		x coin		c			c
1088	x				c		(?) <sup>c</sup>
1135		x coin		?			
1157	x	x		tail	x	x+c	
1166	x				c	x	
1178		x	c	o	c	c	c
1216					c	x	
1221	x	?	c	c	c	c	c
1289		x		?		c	
1325	x	x	c		c		
1365	x	x	c	o	?		c

Table A.2.1 (cont'd)  
Summary of  $^{60}\text{Co}$   $\gamma$  rays observed in the  $\gamma$  experiments

	S	T	Li	P	O	Na	Mg
1397		X	c	c	T		
1418	X						
1422		X					
1427		X	c	c	aT		
1437		X					
1469	X	X			X	c	T
1538		X					
1552	X	X	c	X		Tc	
1587	X	T			(a)		
1598		X					
1640 <sup>c</sup>	X	XX		(X)	X c	X	c
1680		X					c
1741		X					T
1744 <sup>d</sup>							
1792	no	oXX		c	c	XX	c
1834	X	T	c		(a)	X	
1842		X coils		(a)			
1898		X		c		X-cT	(a)
1983		X				X-cT	
1941		X					
2028 <sup>d</sup>		X X					
2161		X		(a)			c
2171				(a)			c
2202			(T)				
2475							c
2509	X	X	T				T
2631		X					T
2701		X					
2715		X					T
2778		oote X					
2782		X	T				
2788		X					
2877		X					

Table A.2.2  
 Contents of  $^{60}\text{Co}$  coincidence gates at  $E_{\gamma} = 12 \text{ MeV}$

$E_{\gamma}$ gate (keV)	Contents and comments
62	(82) (117) (218) [ $^{60}\text{Co} + \alpha$ rays but rolled off]
104	(188) (238) (340) (882)
187	(182) 511 (882) 870 (811)
227a	(118) (136) (175) (187) <u>270</u> <u>285</u> 338 511 (557)
270	<u>225</u> 287 332 (814)
272	(174) <u>224</u> 511 (642) (915) (1333)
286a	(200) (270) (511) (670) (712) (1014) (1047)
327	<u>454</u> (464) (511) (875) (1008) (1488)
334	<u>272</u> <u>511</u> 827 882 (908) 1333 (1456) (1799) (1862)
330c	<u>428</u> <u>511</u> 838 (810) (870) <u>282</u> 850 838 <u>908</u> 1107 1182 <u>1328</u> (1354) <u>1347</u> 1398 <u>1428</u> <u>1600</u> 1717 (1780) 2102 (2284) (2581) (2680) (2784) (2954) [ $^{60}\text{Ni} + 1$ ]
348	137 (184) (339) (511) (550) (848) (1078)
357	(153) 484 (468) (485) (511) (642) (828) (979) (1102) (1333)
384	511 (828) (837) 1430 (2162)
422c	511 <u>878</u> (912) (947) (998) [ $^{59}\text{Ni} + 1$ ]
454	<u>104</u> <u>228</u> <u>488</u> 808 1047 1061 (1328) (1410) 1640
557	(511) <u>1047</u> (1087) <u>1640</u> (1791)
582c	(180) (284)
600	(147) (511)
688	187 338 511 909 1367
781	104 (511)
790	(182) <u>228</u> <u>241</u> (511) (518) 557 (857) (1212) (1472)
804c	(28) (285) (322)
814a	274 322 485 <u>482</u> 511 708 951 (1178) (1333) <u>1478</u> 1792 2210 2665 2823 [ $^{60}\text{Cu} + 1$ ]
836c	<u>182</u> (240) 338 (729) 773 (1047) 1183 <u>1426</u> 2114 [ $^{59}\text{Ni}$ ]
847	(243) (511)
886c	<u>338</u> 388 <u>428</u> <u>511</u> <u>1101</u> 1367 1687 <u>1716</u> 1833 [ $^{59}\text{Ni}$ ]
1021	(202) (408) (511) 1082
1046	(202) <u>228</u> 287 (422) (450) 484 557 (511) 815
1051	374 454
1080	252 <u>282</u> (288) (338) (511) (515) 1022
1125	224 (284) (339) (511) (1792) 2578
1157	484 (508) (558) 1642
1222c	(184) (484) 511
1289c	(322) 340 2578 [ $^{59}\text{Ni} + 1$ ]
1325	(339) <u>484</u>
1307c	<u>338</u> 484 464 511 1188 1333 <u>1644</u> 2895 [ $^{59}\text{Cu} + ^{60}\text{Zn} + 1$ ]
1427c	173 338 782 808 (1357) <u>1610</u> (1792) (2335)
1448	(248) 484 483 558 (792)
1532	(1046)
1596	<u>2028</u>
1640a	228 <u>454</u> <u>558</u> (1399)
1680c	(135) (285) 339 (492) 511 (908) (1010) 2323 [ $^{59}\text{Ni}$ ]
1782c	(322) <u>338</u> <u>511</u> 1271 <u>1333</u> 1420 [ $^{60}\text{Ni}$ ]
1814c	<u>227</u> 898 [ $^{59}\text{Ni} + 1$ ]
1842	224 (511) (815)
2028a/c	(422) (428) <u>1508</u>
2181c	511 (1187) [ $^{60}\text{Ni} + ^{60}\text{Zn} + 1$ ]
2508c	(887) 898 1604
2755	(485) (558) 1271



Table A.2.3  
 Contents of  $^{60}\text{Co}$  coincidence gates at  $E_{Na} = 70 \text{ MeV}$

gate (keV)	Contents
104	438 454 511 (602) (738) (868) 1046 1157 1639 (1332)
225d	(62) <u>270</u> 511 738 1046 1639
270	132 224 1046
285	(130) (314) (368) (738) (1046)
287	(134) (270)
334c	(438) 1173 <u>1333</u> (1460) (1374) (1892)
363	462
454	<u>104</u> <u>511</u> <u>738</u> <u>1046</u> <u>1156</u> <u>1216</u> <u>1638</u> <u>1744</u>
461c	56 128 (316) (339) 511 <u>558</u> 1638 1744
553	(62) (104) 221 310 454 557 570 (590) 778 (880) 906 (940)
558	(114) (150) (156) (180) (460) (494) <u>511</u> (539) (590) 642 738 (810) (906) <u>1046</u> (1086) (1128) <u>1157</u> (1140) 1638 (1644) (1832)
593c	(62) (233) (321) (454) (634) (798) (1638)
596c	(62) (86) 322 511 557 (882) (1084) (1508) (1610) (1680) (1862)
618	(104) (270) (294) (346) (511) (608) (1044) (1333) (1418) (1552) 1680
738	104 224 (294) (346) (511) (608) (1044) (1332) (1418) (1552) (1680)
868	(150)
1046	(60) 104 <u>454</u> <u>538</u> (616) (642) (988) (1364) <u>1552</u> 2014
1100	(62) (124) (170) (342) (634) (676) (752)
1158	(62) (68) <u>104</u> (126) <u>224</u> (270) (320) <u>454</u> <u>558</u> (598) (740) (956) (1332) (1416) <u>1638</u> (1646) (1744)
1166c	(62) (104) (128) (196) (224) (252) (320) (384) 454 (558) (598) (738) (870) (954) 1332 1462
1224c	(64) (74) (196) (290) (321) (370) <u>466</u> (492) <u>511</u> (588) (596) (606) <u>833</u> (844) (978) (1104)
1552c	<u>104</u> 146 <u>224</u> <u>270</u> <u>321</u> 334 <u>339</u> <u>454</u> <u>465</u> 476 <u>511</u> <u>558</u> 596 <u>738</u> <u>788</u> <u>834</u> (848) <u>1046</u> (1065) <u>1083</u> <u>1173</u> <u>1224</u> <u>1332</u> 1366 <u>1460</u> (1454) <u>1609</u> <u>1639</u> (1688) 1728 <u>1757</u>
1639	(72) (104) 188 224 (240) (314) <u>453</u> <u>460</u> <u>558</u> (696) (737) (904) <u>1157</u> (1224) (1452) (1482) 1638
1745	(86) (158) (339) (460) (511) (708) (790) (1128) (1158)

Table A.2.4  
Summary of <sup>60</sup>Cu levels based on the γ experiments

$E_{\gamma}$	Y	u	Li	B	O	Na	Mg
0	x	x	x	x	x	x	x
63	x	x				x	x
163	(c)						
287	x	x		x	x	x	x
334	x	x		x	x	x	x
363	x	x	c	c	x	(x)	
454	x	x	(x)	x	x	x	x
567	x	x	x	x	x	x	x
571	x			(x)		(x)	
600	x		(c)	c		(x)	c
689	x		x	x	x	x	x
781	x	x			(?)		
904	x				(x)		
914	x	x			(x)	x	
947	x		c	c	(x)		
975	x						
1007	x		c	c	(c)	x(coin)c	c
1068	?					x	
1110	x						
1249	x						
1367	x			c			c
1422	x	x	c	c	(c)	x(coin)	c
1428	x		c	c	(c)		
1806	x			?			
1804	x	x	(x)	(x)	x	x	(x)
1880						x	
1988	x	c	c	c		x c	c
1779	x	x	?		?		
1791	x						
1878							
1930							
1990							
2027	x	x			x		
2035							
2179							
2197	x	x		(x)	x	x	x
2248						x	
2286							
2350	x	x		7c	7c		7c
2519	x					(c)?	
2524	x			(c)			(c)
2539	x		c	c	c	c	
2658						x	
2682	x	x			c		7c
2763							
2780						x	
2817	x	x			(c)		
2915							
2977							
3088	x	x	?				or <sup>60</sup> Zn
3122							
3155	x	x	c?	x		x(coin)	
3191	x	x			(?)		
3315	x						
3355	x	x		(x)	x	x	

Table A.2.4 (cont'd)  
 Summary of <sup>60</sup>Co levels based on the γ experiments

E <sub>γ</sub>	γ	A	Li	B	O	Na	Mg
3345	X						
3384	X		o	o	Y		
3734	X						
3888	X						
3773		X					X
3837							X
3877	X						
3883							X
4083							X
4478							X
4321		X	(o)	(o)	Y		X
4818							
4838							
5188		X					X
5637							X
5837							X

## REFERENCES

- Alford, W.P., Lindgren, R.A., Elmore, D.E. and Boyd, R.N., 1975. Nucl. Phys. A243, 269.
- Arai, Y., Frijioka, M., Tanaka, E., Shinozuka, T., Miyatake, H., Yoshii, M. and Ishimatsu, T., 1981. Phys. Lett. 104B, 1981.
- Auble, R.L., 1979. Nuclear Data Sheets 28, 103.
- Auble, R.L., 1975. Nuclear Data Sheets, 16, 1.
- Auble, R.L., 1975. Nuclear Data Sheets, 16, 317.
- Bardeen, J., Cooper, L.N. and Schrieffer, J.R., 1957. Phys. Rev. 106, 162.
- Bohr, A., 1952. Mat. Fys. Medd. Dan. Vid. Selsk. 26, no. 14.
- Bohr, A. and Mottelson, B.R., 1953. Mat. Fys. Medd. Dan. Vid. Selsk. 27, no. 16.
- Bohr, A., Mottelson, B.R. and Pines, D., 1958. Phys. Rev. 110, 936.
- Camp, D.C. and van Lehn, A.L., 1969. Nucl. Instr. Meth. 76, 192.
- Castel, B., Johnstone, I.P., Singh, B.P. and Stewart, K.W.C., 1972. Can. J. Phys. 50, 1630.
- Chan, T.U., Agard, M., Bruandet, J.F., Chambon, B., Dauchy, A., Drain, D., Giorni, A., Glasser, F. and Morand, C., 1982. Phys. Rev. C26, 424.
- Chandra, H. and Rustgi, M.L., 1971. Phys. Rev. C4, 874.
- Chandra, H. and Rustgi, M.L., 1972. Phys. Rev. C6, 1281.
- Cumming, J.B., 1959. Phys. Rev. 114, 1600.
- Diamond, R.M., Matthias, E., Newton, J.O. and Stephens, F.S., 1966. Phys. Rev. Lett. 16, 1205.

- Din, G.U., Cameron, J.A., Janzen, V.P. and Schubank, R.B., (1984). The reactions  $^{58}\text{Ni}(p,\gamma)^{59}\text{Cu}$  and  $^{58}\text{Ni}(p,p'\gamma)^{58}\text{Ni}$  from 0.7 to 5.0 MeV, 1985. Phys. Rev. C31, 800.
- Dulfer, G.H., Ketel, T.J., Kalshoven, A.W.B. and Verheul, H., 1972. Zeit. Phys. 251, 416.
- von Egmond, A., Hofstra, P., Boeker, E., Allaart, K. and Paar, V., 1981. Zeit. Phys. A300, 323.
- Ekström, L.P., Al-Naser, A.M., Lornie, P.R.G. and Twin, P.J., 1979. Nucl. Inst. Meth. 158, 243.
- Ekström, L.P. and Lyttkens, J., Ed., 1983. Nuclear Data Sheets 38, 463.
- Endt, P.M., 1979. Atomic Data and Nuclear Data Tables 23, 547.
- Engel, H.A., 1966. Introduction to Nuclear Physics Addison Wesley Publ. Co. Inc., Reading, Massachusetts.
- Evers, D., Assmann, W., Rudolph, K. and Skorcka, S.J., 1974. Nucl. Phys. A230, 109.
- Gedcke, D.A. and McDonald, J.W., 1967. Nucl. Instr. Meth. 55, 377.
- Gedcke, D.A. and McDonald, J.W., 1968. Nucl. Instr. Meth. 58, 253.
- Glaudemans, P.W.M., 1970. Applications of the nuclear shell model lecture notes. Nuclear Physics Seminar, Groningen.
- Greenfield, M.B. and Bingham, C.R., 1972. Phys. Rev. C6, 1756.
- Haxel, O., Jensen, J.H. and Suess, H.E., 1949. Phys. Rev. 75, 1766.
- van Hienen, J.F.A., Chung, W. and Wildenthal, B.H., (1976). Nucl. Phys. A269, 159.
- (also Rept. MSUCL-207, March 1976)
- Hoffman, E.J. and Sarantites, D.G., 1970. Nucl. Phys. A157, 584.

- Hoffman, E.J. and Sarantites, D.G., 1969. Phys. Rev. 177, 1647.
- Hoffman, E.J., van Patter, D.M., Sarantites, D.G. and Barker, J.H., 1973. Nucl. Instr. Meth. 109, 3.
- Honkanen, J., Kortelahti, M., Eskala, K. and Vierinen, K., 1981. Nucl. Phys. A366, 109.
- Ionescu, V.A., Kern, J., Nordmann, C., Olrich, S. and Reichart, W., 1981. Nucl. Instr. Meth. 190, 19.
- Jaffrin, A., 1972. Nucl. Phys. A196, 577.
- James, A.N., Twin, P.J. and Butler, P.A., 1974. Nucl. Instr. Meth. 115, 105.
- Kamermans, R., Jongsma, H.W., van der Spek, J. and Verheul, H., 1974. Phys. Rev. C10, 620.
- Kim, H.J., 1976. Nuclear Data Sheets 17, 485.
- Koops, J.E. and Glaudemans, P.W.M., 1977. Zeit. Phys. A180, 181.
- Kisslinger, L.S. and Kumar, K., 1967. Phys. Rev. Lett. 19, 1239.
- Lawson, R.D. and Utretsky, J.L., 1957. Phys. Rev. 108, 1300.
- Lederer, C.M. and Shirley, V.S., 1978. Ed. Table of Isotopes, J. Wiley and Sons, Inc., New York.
- Lightbody, J.W., Jr., 1972. Phys. Lett. 38B, 475.
- Litherland, A.E. and Ferguson, A.J., 1961. Can. J. Phys. 39, 788.
- Mayer, M.G., 1949. Phys. Rev. 75, 1969.
- McFee, J.E., 1977. McMaster University, Ph.D. thesis.
- Morand, C. and Chan, T.U., Chan, 1981. Comp. Phys. Comm. 23, 393.
- Newton, J.O., 1969. Prog. in Nucl. Phys. Vol. 2, Ed. by Brink, D.M. and Mulvey, J.H., Pergamon Press, Oxford.
- Nilsson, S.G., 1955. Mat. Fys. Medd. Dan. Vid. Selsk. 29, no. 16.

- Parikh, J.K., 1972. Phys. Rev. C6, 2177.
- Perazzo, R.P.J., 1972. Nucl. Phys. A186, 379.
- Pougheon, F., Roussel, P., Colomboni, P., Doubre, H. and Roynette, J.C., 1972. Nucl. Phys. A193, 305.
- Preston, M.A. and Bhaduri, R.K., 1975. Structure of the Nucleus, Addison-Wesley Publ. Co. Inc., Massachusetts.
- Roodbergen, S., Visser, H., Molendijk, W., Bedet, H.S. and Verheul, H., 1975. Zeit. Phys. A275, 45.
- Rose, H.J. and Brink, D.M., 1967. Rev. Mod. Phys. 39, 306.
- Rowe, D.J., 1970. Nuclear Collective Motion, Methuen and Co., Ltd., London.
- Sandhu, T.S. and Rustgi, M.L., 1975. Phys. Rev. C12, 666.
- Sarantites, D.G., Barker, J.H., Lu, N.H., Hoffman, E.J. and van Patter, D.M., 1973. Phys. Rev. C8, 629.
- Sawa, Z.P., 1973. Ph.D. Thesis, Research Inst. Phys. Stockholm.
- de Shalit, A., 1961. Phys. Rev. 122, 1530.
- Sheldon, E. and van Patter, D.M., 1966. Rev. Mod. Phys. 38, 143.
- Sheldon, E. and Strang, 1969. Comp. Phys. Comm. 1, 35.
- Shikata, V., Sakakura, M. and Sebe, T., 1981. Zeit. Phys. A300, 217.
- Singh, R.P. and Rustgi, M.L., 1971. Phys. Rev. C3, 1172
- Smith, P.J., Ekström, L.P., Kearns, F., Twin, P.J. and Ward, N.J., 1982. J. Phys. G8, 281.
- Throop, M.J., Cheng, Y.T. and McDaniels, D.K., 1975. Nucl. Phys. A239, 333.
- Vo-Van, T. and Wong, S.S.M., 1977. Can. J. Phys. 55, 909.
- Waddington, J.C.W., 1980. McMaster Accelerator Lab Annual Report, p. 36.

Weber, D.J., Crawley, G.M., Benenson, W., Kashy, E. and Nam, H., 1979. Nucl. Phys. A313, 385.

Weidinger, A., Finckh, E., Johnke, U. and Schreiber, B., 1970. Nucl. Phys. A149, 241.

Weisskopf, V.F., 1952, in Theoretical Nuclear Physics, by Blatt and Weisskopf, John Wiley and Sons, Inc., New York.

von Weizsäcker, C.F., 1935. Zeit. Phys. 96, 431.

Winsborrow, R.P.J. and Macefield, B.E.F., 1972. Nucl. Phys. A182, 481.

Wong, S.S.M., 1970. Nucl. Phys. A159, 235.

Woods, C.W., Stein, N. and Sunier, J.W., 1978. Phys. Rev. C17, 66.

Yamazaki, T., 1967. Nucl. Data, Sect. A, 3, 1.